Wind tunnel tests of Risø-B1-18 and Risø-B1-24

Fuglsang, Peter; Bak, Christian; Gaunaa, Mac; Antoniou, Ioannis

Publication date:
2003

Document Version
Publisher's PDF, also known as Version of record

Risø-R-1375(EN)

Wind Tunnel Tests of Risø-B1-18 and Risø-B1-24

Peter Fuglsang, Christian Bak, Mac Gaunaa, Ioannis Antoniou

Risø National Laboratory, Roskilde, Denmark
January 2003

Abstract
This report contains 2D measurements of the Risø-B1-18 and Risø-B1-24 airfoils. The aerodynamic properties were derived from pressure measurements on the airfoil surface and in the wake. The measurements were conducted in the *VELUX* open jet wind tunnel, which has a background turbulence intensity of 1%, and an inlet flow velocity of 42 m/s. The airfoil sections had a chord of 0.600 m giving a Reynolds number of 1.6×10^6. The span was 1.9 m and end plates were used to minimize 3D flow effects. The measurements comprised both static and dynamic inflow. Static inflow covered angles of attack from -5^o to 30^o. Dynamic inflow was obtained by pitching the airfoil in a harmonic motion around various mean angles of attack. The test matrix involved smooth flow, various kinds of leading edge roughness, stall strips, vortex generators and Gurney flaps in different combinations.

The quality of the measurements was good and the agreement between measurements and numerical CFD predictions with EllipSys2D was good. For both airfoils predictions with turbulent flow captured very well the shapes of lift and drag curves as well as the magnitude of maximum lift. Measurements of Risø-B1-18 showed that the maximum lift coefficient was 1.64 at an angle of attack of approximately 13^o. The airfoil was not very sensitive to leading edge roughness despite its high maximum lift. Measurements with stall strips showed that stall strips could control the level of maximum lift. The Risø-B1-24 measurements showed that the maximum lift coefficient was 1.62 at an angle of attack of approximately 14^o. The airfoil was only little sensitive to leading edge roughness despite its high relative thickness and high maximum lift. Measurements with delta wing shaped vortex generators increased the maximum lift coefficient to 2.02 and measurements with Gurney flaps increased the maximum lift coefficient to 1.85. Measurements with combination of vortex generators and Gurney flaps showed a maximum increase in the maximum lift coefficient to 2.17.

At the design Reynolds number of 6×10^6 numerical predictions showed that there was a clear increase in the maximum lift coefficient of 0.22 for Risø-B1-18 and 0.21 for Risø-B1-24.

The project was co-financed by Risø National Laboratory and SSP Technology A/S.

ISBN: 87-550-3139-0
ISBN: 87-550-3140-4(Internet)

ISSN: 0106-2840

Print: Pitney Bowes Management Services Danmark A/S, 2003

Contents

1 Summary of results 6

1.1 Risø-B1-18 6
1.2 Risø-B1-24 7
1.3 Conclusions in summary 10

2 Introduction 12

3 Experimental set-up 13

3.1 Testing facility 13
3.2 Wind tunnel boundary corrections 15
3.3 Wind tunnel flow conditions 16
3.4 Calculation methods 16

4 Airfoil sections and aerodynamic devices 18

4.1 Airfoil sections 18
4.2 Leading edge roughness 18
4.2.1 90° zigzag tape 19
4.2.2 60° zigzag tape 19
4.2.3 Car customising tape 19
4.3 Stall strips 20
4.3.1 Curved stall strip 20
4.3.2 Triangular stall strip 20
4.4 Vortex generators 21
4.5 Gurney flaps 22

5 Results 24

5.1 Testing conditions 24
5.2 Numerical calculations 24
5.3 Presentation of results 24

6 Results for Risø-B1-18 27

6.1 Risø-B1-18, smooth flow (run024) 27
6.2 Risø-B1-18, leading edge roughness (run 025, 026, 030, 031, 032, 033) 29
6.3 Risø-B1-18, stall strips (run 034, 035, 036, 038) 33
6.4 Risø-B1-18, dynamic stall (run 029) 35

7 Results for Risø-B1-24 39

7.1 Risø-B1-24, smooth flow (run002) 39
7.2 Risø-B1-24, leading edge roughness (run 006, 007, 008) 41
7.3 Risø-B1-24, vortex generators (run 012, 016, 017) 43
7.4 Risø-B1-24, vortex generators at x/c = 0.20, leading edge roughness (run 009, 012) 45
7.5 Gurney flaps (run 013, 018, 019, 020, 021) 47
7.6 Vortex generators, Gurney flaps (run 011, 014, 015) 51
7.7 Risø-B1-24, vortex generators, Gurney flaps, leading edge roughness (run 010, 011) 53
7.8 Risø-B1-24, dynamic stall (run 005) 55

8 Sensitivity of airfoil characteristics 59

8.1 Theoretical and measured airfoil shape 59
8.2 Variation in Reynolds number 61

9 Discussion 63

9.1 Risø-B1-18 63
9.2 Risø-B1-24 65
9.3 Airfoil comparison 67
9.4 Sensitivity of airfoil characteristics 68
9.5 Variation with Reynolds number 68

10 Conclusions 70

A Measurement overview 73

A.1 List of symbols 73
A.2 Measurement types 74
A.3 Data file naming convention 76
A.4 Data file formats 76
A.5 Performed measurements 79

Nomenclature

c	[m]	Airfoil chord
h	[m]	Jet height
k		Reduced frequency
Δp	[Pa/m]	Pressure loss
p	[Pa]	Static pressure
p_o	[Pa]	Total pressure head
q	[Pa]	Dynamic pressure
s		Airfoil surface co-ordinate
t	[s]	Pitch motion time
x		Co-ordinate in chord direction
y		Wake rake vertical co-ordinate, airfoil vertical co-ordinate
A	[°]	Pitch motion amplitude
c_d		Drag coefficient
c_l		Lift coefficient
c_m		Moment coefficient
c_n		Normal force coefficient
c_P		Airfoil pressure coefficient
c_t		Tangential force coefficient
Re		Reynolds number
T	[°C]	Air temperature
V	[m/s]	Velocity
α	[rad] [°]	Angle of attack
ε		Speed-up factor
ρ	[kg/m^3]	Air density
ω	[rad/s]	Pitch motion angular velocity

Subscripts

1-3	Pitot tube measurement
a	Airfoil section measurement
atm	Atmospheric value
j	Jet outlet measurement
m	Mean value
min	Minimum value
max	Maximum value
p	Pressure measurement
t	Measured value (uncorrected)
w	Wake rake measurement
∞	Free stream reference for normalisation of airfoil forces

1 Summary of results

Two-dimensional wind tunnel testing was carried out for the Risø-B1-18 and Risø-B1-24 airfoils in the *VELUX* wind tunnel at Re = $1.6 \cdot 10^6$. The measurements comprised both static and dynamic inflow. Static inflow covered inflow angles from -5^o to 30^o. Dynamic inflow was obtained by pitching the airfoil in a harmonic motion around various mean angles of attack. The test matrix involved smooth flow, various kinds of leading edge roughness, stall strips, vortex generators and Gurney flaps. For Risø-B1-18 emphasis was put on leading edge roughness and stall strips whereas emphasis was put on vortex generators and Gurney flaps for Risø-B1-24.

The quality of the measurements was in general very good. Pressure measurements on the airfoil surface measured through pressure holes by a pressure measurement system provided the force coefficient normal to the surface and the pressure response of a wake rake yielded the drag coefficients at low angles of attack. Airfoil lift, drag and moment coefficients versus angle of attack were derived from the measurements.

Numerical calculations predicted the theoretical target characteristics for both airfoils. The CFD code EllipSys2D was used for the computations of fully turbulent flow as well as for transitional flow.

1.1 Risø-B1-18

Figure 1-1 shows results for smooth surface conditions. The maximum lift coefficient was 1.64 and the minimum drag coefficient was 0.0090. Separation occurred from the trailing edge at around 12^o. The measurements agreed very well with the numerical predictions. Especially the turbulent predictions captured the shape of the lift curve very well. The magnitude of the measured drag at attached flow fell between the predictions for transitional and turbulent flow because of the presence of background turbulence and the non-hydraulically smooth surface.

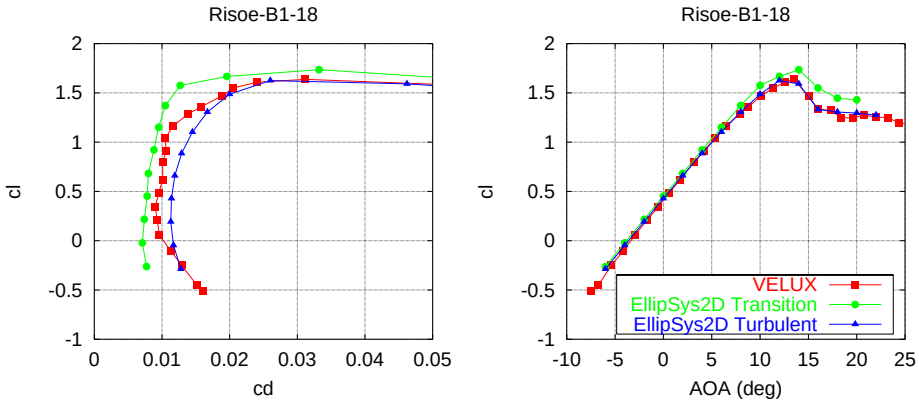

Figure 1-1 Risø-B1-18 VELUX smooth flow measurement and EllipSys2D free transition and turbulent flow predictions.

Figure 1-2 shows results from measurements with the most severe cases of leading edge roughness. The measurements showed that the airfoil is not very sensitive to

leading edge roughness. Maximum lift was not sensitive to standard zigzag tape at 5% chord on the suction side and 10% chord on the pressure side (ZZ90 5%/10%). Drops in maximum lift of 0.25 and 0.44 were measured for the more severe cases of leading edge roughness with zigzag tape on the very leading edge part of the suction side (ZZ90 and ZZ60).

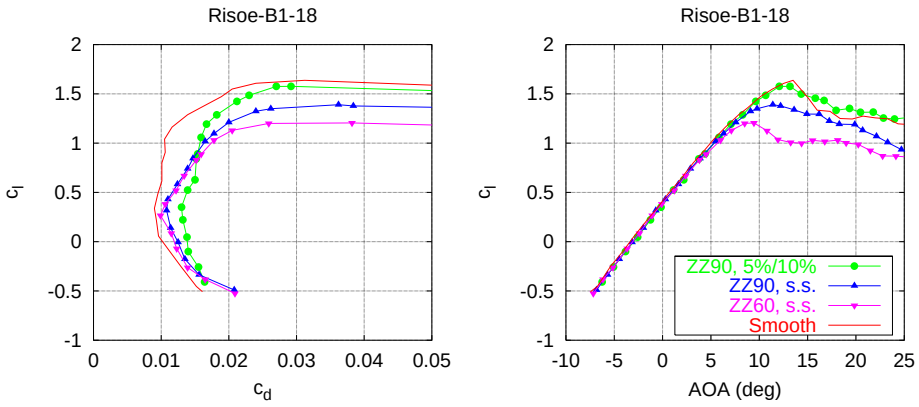

Figure 1-2 Risø-B1-18 VELUX measurements with leading edge roughness.

Figure 1-3 shows results from measurements with stall strips from 0% to 3% chord on the pressure side. The maximum lift was not sensitive to stall strips further downstream than 3% chord, whereas stall strips at the very leading edge resulted in a drop in maximum lift coefficient of 0.4. Minimum drag increased when stall strips were moved towards the leading edge and the increase in drag due to suction side separation moved to lower angles of attack. Even though the airfoil was not intended for use with stall strips, the measurements showed that stall strips were feasible.

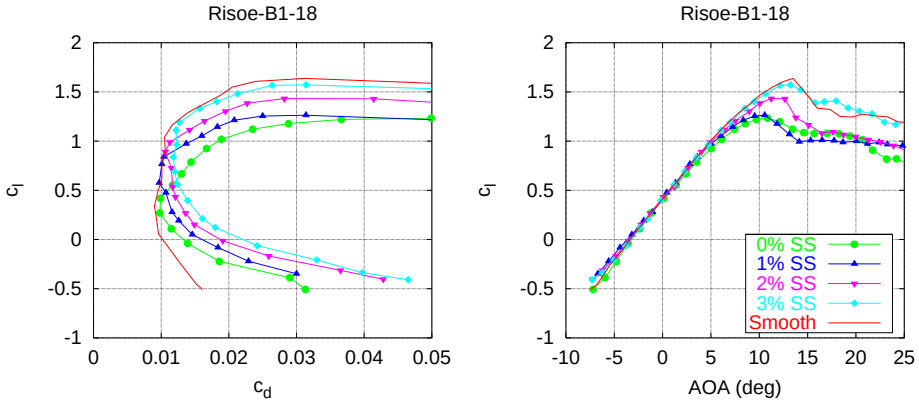

Figure 1-3 Risø-B1-18 VELUX measurements with stall strips.

1.2 Risø-B1-24

Figure 1-4 shows results for smooth surface conditions. The maximum lift coefficient was 1.62 and the minimum drag coefficient was 0.012. Separation occurred from the trailing edge at around 12°. A numerical prediction with turbulent flow captured very well the shapes of both the lift and drag curves. The magnitude of drag at low angles of attack was predicted too high because of the too high skin friction of the anticipated turbulent boundary layer. At very low angles of attack, the prediction showed separation on the pressure side, which was not present in the measurements.

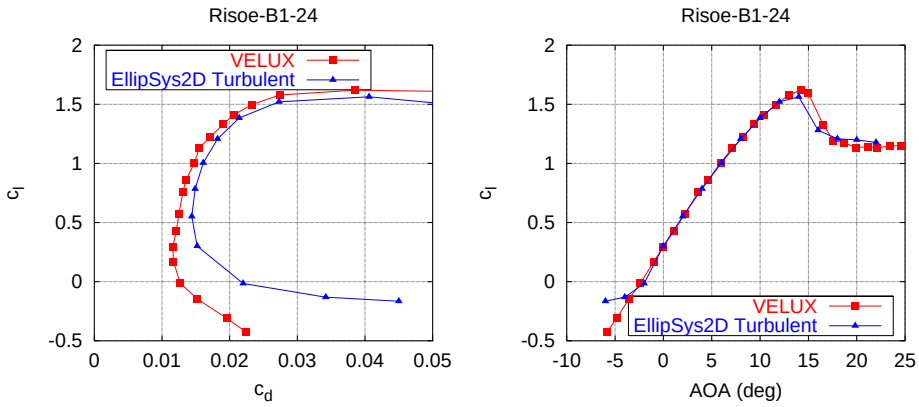

Figure 1-4 Risø-B1-24 VELUX smooth flow measurement and EllipSys2D turbulent flow predictions.

Figure 1-5 shows results from measurements with leading edge roughness. The measurements showed that the airfoil is only slightly sensitive to leading edge roughness despite its high relative thickness and high maximum lift coefficient. Maximum lift was only marginally sensitive to standard zigzag tape at 5% chord on the suction side and 10% chord on the pressure side (ZZ90 5%/10%). The drop in maximum lift coefficient was 0.45 for the most severe configuration, ZZ60 and 0.29 for the ZZ90 configuration.

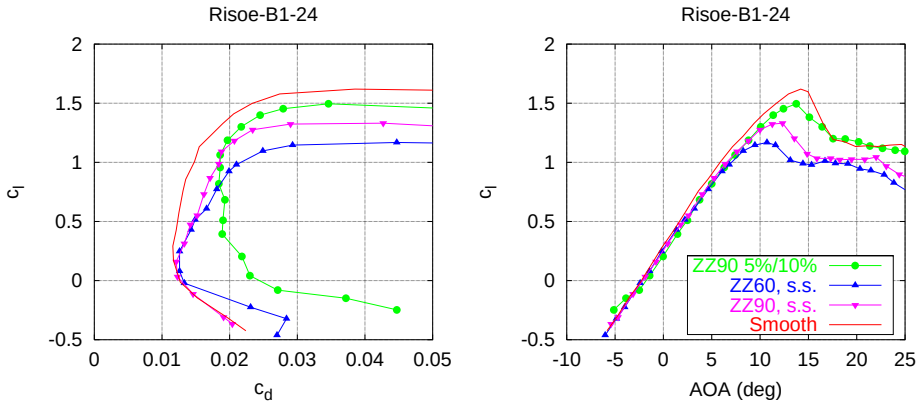

Figure 1-5 Risø-B1-24 VELUX measurements with leading edge roughness at different locations.

Figure 1-6 shows measurements with delta wing shaped vortex generators with a maximum height of 1% chord. All measurements with vortex generators showed an increase in the maximum lift coefficient and at the same time an increase in the minimum drag coefficient. The optimum configuration was found at the 20% chord where the maximum lift coefficient was increased by 0.40 to 2.02 compared to smooth flow. At the same time the increase in drag was limited.

Measurements with vortex generators at 20% chord and ZZ90 leading edge roughness showed a drop in maximum lift coefficient of 0.27 to 1.75. The corresponding drop in maximum lift coefficient with similar roughness without vortex generators was 0.29.

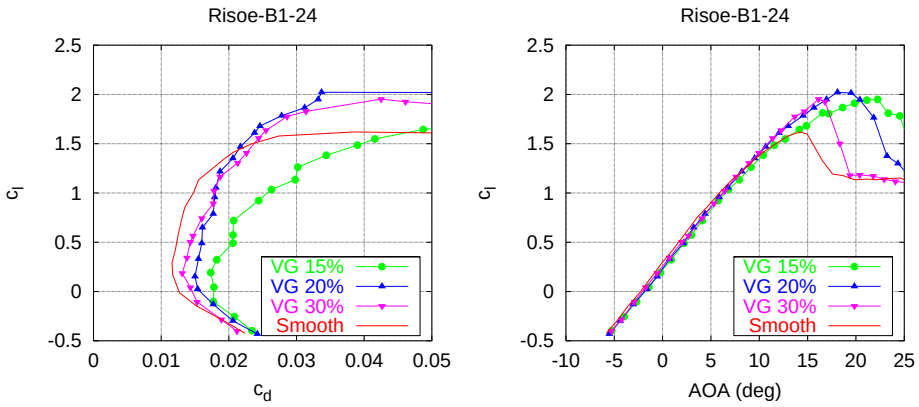

Figure 1-6 Risø-B1-24 VELUX measurements with vortex generators.

Figure 1-7 shows measurements with Gurney flaps. Measurements with triangular Gurney flaps of different height showed an increase in maximum lift coefficient and a decrease in zero lift angle of attack with increasing Gurney flap height. The optimum configuration had a height of 1% of the chord resulting in an increase in the maximum lift coefficient of 0.23 to 1.85 and a limited increase in drag.

Measurements with Gurney flaps of the same height but with different shapes showed that the difference in the maximum lift coefficient was insignificant and the difference in drag was only marginal.

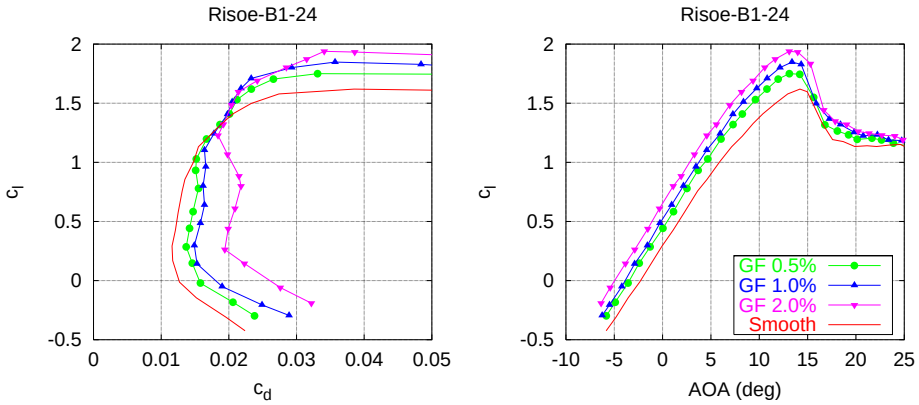

Figure 1-7 Risø-B1-24 VELUX measurements with Gurney flaps of different height.

Figure 1-8 shows measurements of vortex generators and Gurney flaps in combination. The optimum configuration with a triangular Gurney flap of height 1% and vortex generators at 20% chord resulted in an increase in maximum lift coefficient of 0.55 to 2.17. The reduction in the maximum lift to drag ratio was minimal. Hence, the combination of vortex generators and Gurney flaps may provide a significant increase in maximum lift.

Measurements with vortex generators, Gurney flaps and leading edge roughness showed a drop in maximum lift coefficient of 0.23 from leading edge roughness, which is less than the drop of 0.29 from similar roughness compared with the smooth flow configuration.

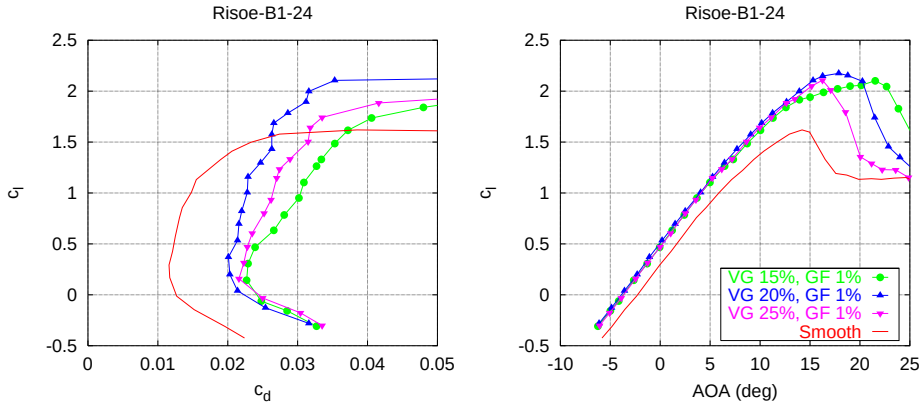

Figure 1-8 Risø-B1-24 VELUX measurements with vortex generators and Gurney flaps

1.3 Conclusions in summary

The following conclusions could be drawn for the Risø-B1-18 airfoil:

- The maximum lift coefficient was 1.64 at an angle of attack of approximately 13°.
- Measurements with leading edge roughness showed that the airfoil was not very sensitive to leading edge roughness despite its high maximum lift.
- Standard zigzag tape of 90° at 5% chord on the suction side and 10% chord on the pressure side reduced the maximum lift coefficient by 0.06.
- Zigzag tape of 90° at the very leading edge of the suction side caused a drop in maximum lift coefficient of 0.25.
- Measurements with stall strips showed that stall strips could control the level of maximum lift.
- Stall strips at the very leading edge of the pressure side reduced the maximum lift coefficient by 0.4
- Dynamic inflow measurements from pitch motion showed expected results for hysteresis curves of lift, drag and moment coefficients. The slopes of the loops in general followed the slopes of the mean curves.

The following conclusions could be drawn for the Risø-B1-24 airfoil:

- The maximum lift coefficient was 1.62 at an angle of attack of approximately 14°.
- Measurements with leading edge roughness showed that the airfoil was only marginally sensitive to leading edge roughness despite its high relative thickness and high maximum lift.
- Standard zigzag tape of 90° at 5% chord on the suction side and 10% chord on the pressure side reduced the maximum lift coefficient by 0.12 to 1.50.
- Zigzag tape of 90° at the very leading edge of the suction side caused a drop in maximum lift coefficient of 0.29.
- Measurements with Delta wing shaped vortex generators of height 1% chord located at 20% chord increased the maximum lift coefficient by 0.40 to 2.12.
- Measurements with triangular shaped Gurney flaps of height 1% increased the maximum lift coefficient by 0.23 to 1.85.
- Measurements with Gurney flaps of the same height with different shapes showed insignificant differences in maximum lift and minimum drag.
- Measurements with a combination of vortex generators and Gurney flaps showed a maximum increase in the maximum lift coefficient of 0.55 to 2.17.

- Dynamic inflow measurements from pitch motion showed expected results for hysteresis curves of lift, drag and moment coefficients. The slopes of the loops in general followed the slopes of the mean curves.

The maximum Reynolds number for the VELUX wind tunnel is 1.6×10^6, which unfortunately is somewhat lower than the design Reynolds number of 6×10^6. For both Risø-B1-18 and Risø-B1-24 numerical predictions showed that there was a clear increase in the maximum lift coefficient of 0.22 for Risø-B1-18 and 0.21 for Risø-B1-24 when the Reynolds number was increased from 1.6×10^6 to 6×10^6. At the same time there was a decrease in minimum drag of 0.0024 for Risø-B1-18 and 0.0033 for Risø-B1-24.

2 Introduction

This report contains 2D wind tunnel measurements for the Risø-B1-18 and Risø-B1-24 airfoils. The operational design Reynolds number for the airfoils is $Re = 6.0 \cdot 10^6$. The measurements were carried out in the *VELUX* wind tunnel, which has an inlet test section with a background turbulence level of 1% and a maximum flow velocity of 42 m/s. All tests were carried out at the highest possible Reynolds number of $1.6 \cdot 10^6$.

The angle of attack range was between -5° and 30°. The static pressure distribution around the airfoil was measured through holes in the airfoil surface. A wake rake measured total and static pressure distributions in the airfoil wake. The measurements were used to derive airfoil forces versus angle of attack. Fuglsang *et al.* describe the testing facility in detail in [3].

The test matrix included:

- Steady and quasi-steady inflow measurements where mean values were obtained for the airfoil aerodynamic coefficients. During quasi-steady measurements the angle of attack was changed continuously at an average rate around 0.1°/s to 0.5°/s. During steady inflow conditions the angle of attack was changed in steps of 2° and a 20 s duration time series was obtained for each angle of attack. Furthermore, measurements with fixed angle of attack were performed for either 1 minute or 3 minutes typically at high angles of attack.
- Dynamic inflow measurements with the airfoil in pitching motion at amplitudes of approximately ±2° around various mean pitch angles and reduced frequencies around 0.1.

The airfoils were tested under the following surface configurations:

- Smooth surface referred to as ‘smooth flow’.
- Leading edge roughness to simulate the change of the aerodynamic coefficients from dirt and dust accumulation at the leading edge referred to as ‘LER’.
- Stall strips at the leading edge, referred to as ‘SS’.
- Vortex generators on the suction side referred to as ‘VG’.
- Gurney flaps on the pressure side at the very trailing edge referred to as ‘GF’.
- Various combinations of leading edge roughness, vortex generators and Gurney flaps.

For Risø-B1-18 emphasis was put on the sensitivity of the airfoil characteristics with leading edge roughness. For Risø-B1-24 emphasis was put on the airfoil characteristics with vortex generators and Gurney flaps.

3 Experimental set-up

The experimental set-up is briefly described in this chapter. A more complete description can be found in Fuglsang *et al.* [3].

3.1 Testing facility

The *VELUX* wind tunnel is of the closed return type with an open test section which has a cross section of 7.5×7.5 m and a length of 10.5 m, Figure 3-1. The cross section of the quadratic jet blowing into the test section is 3.4×3.4 m. The maximum flow velocity is 42 m/s.

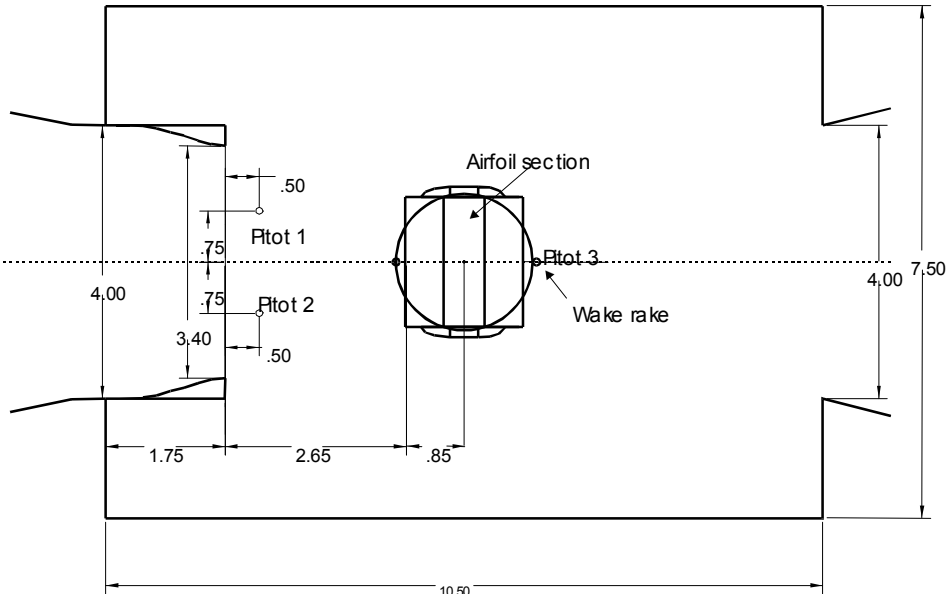

Figure 3-1 The wind tunnel test section with the test stand seen in a top view. The flow is coming from the left.

A test stand was built for 2D airfoil testing, Figure 3-2. The test stand was inserted in the tunnel test section. The airfoil section itself had a span of 1.9 m and a chord of 0.6 m and it was mounted 1.7 m from the tunnel floor and 3.2 m from the nozzle outlet. End plates were fixed to the stand at the ends of the airfoil section to limit 3D flow effects.

Three Pitot tubes measured static and total pressure at different locations in the test section, Figure 3-1. These Pitot tubes were used to measure the wind tunnel reference pressures and to estimate the turbulence level and the stability of the wind tunnel flow.

Quasi-steady measurements at continuously varying angles of attack as well as dynamic inflow measurements were possible. Dynamic inflow was obtained by pitching the airfoil section at a reduced frequency of k = 0.10 and an amplitude of A=±2° with the pitch axis located at x/c = 0.40, see section 3.4.

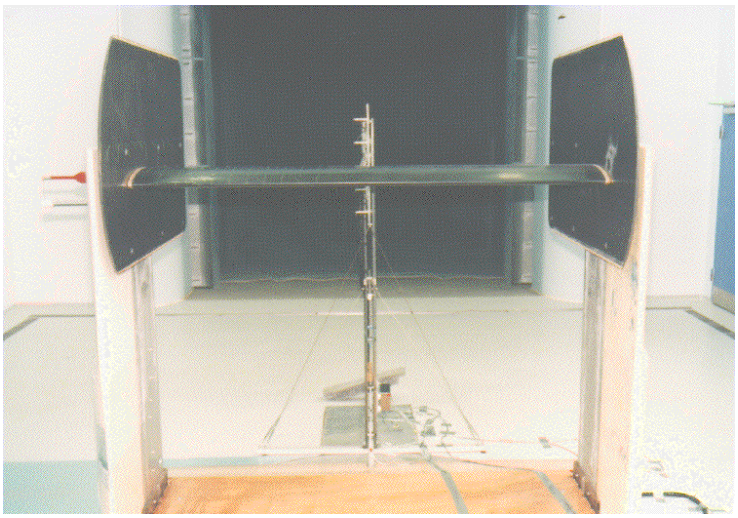

Figure 3-2 The test section with the test stand and the wake rake downstream of the airfoil section.

The wake rake contained 53 total pressure tubes and five static pressure tubes. The vertical span was 0.456 m, Figure 3-3. The distance between the airfoil trailing edge and the wake rake was 0.7 airfoil chords (0.42 m) and the centre of the wake rake was placed approximately at the height of the trailing edge at 0° incidence and behind the centre line of the airfoil section. The rake was not traversed in the horizontal or the vertical directions during the measurements.

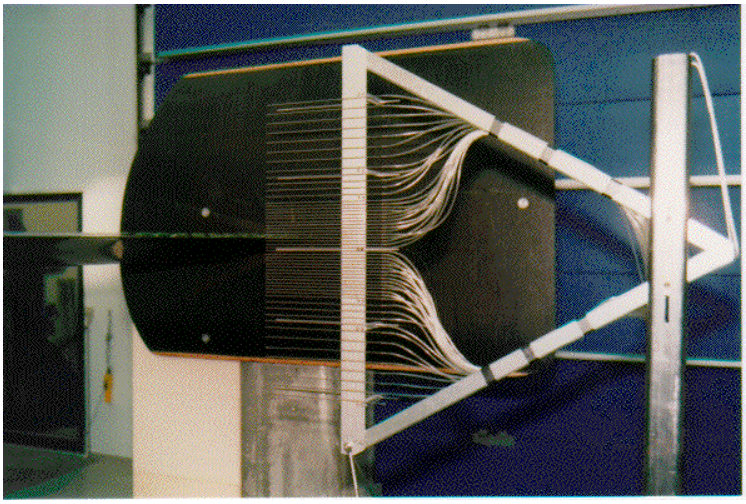

Figure 3-3 The wake rake seen from the side in front of an endplate.

The HyScan 2000 data acquisition system from Scanivalve Corp. was used. Two ZOC33 pressure-scanning modules recorded the pressure signals. For the airfoil surface pressures, 40 1psi and 24 2.5psi range sensors were used. For the wake rake and the Pitot tubes, a total of 64 10´´ H_20 sensors were used. The ZOC module for the airfoil pressures was mounted on the test stand side just outside of the airfoil section. Equal length tubes were lead from the airfoil section through a hollow axis to the pressure module. The pressure module used for the wake and the Pitot tubes was placed on the floor next to the wake rake. A ZOCEIM16 module was used for the acquisition of additional electrical signals.

A total of 131 signals were measured by the data acquisition system during the measurement campaigns:

- 64 airfoil surface static pressures, $p_a(s)$
- 5 wake rake static pressures, $p_w(y)$
- 53 wake rake total pressures, $p_{ow}(y)$
- 3 Pitot tube static pressures, $p_{1\text{-}3}$
- 3 Pitot tube total pressures, $p_{o1\text{-}3}$
- Angle of attack, α
- Air temperature, T
- Atmospheric pressure, p_{atm} (Out of order)

3.2 Wind tunnel boundary corrections

Wind tunnel corrections should be applied for streamline curvature and downwash. Horizontal buoyancy, solid and wake blockage could on the other hand be neglected because the test section configuration corresponds to an open jet, which is free to expand, Ray and Pope [4]. The application of wind tunnel boundary corrections for the VELUX wind tunnel was described in Fuglsang *et al.* [3].

Streamline curvature is introduced to the flow, especially in the case of open test sections. Solid walls do not bound the flow, which is then free to diverge downstream of the airfoil section. The curvature of the flow influences the effective angle of attack over the airfoil and induces drag. In the case of the VELUX tunnel, the presence of the floor close to the jet bottom boundary will influence the streamline curvature and will introduce uncertainty on the wind tunnel corrections. This influence was assumed to be negligible and the applied corrections for streamline curvature do not account for it.

Downwash is introduced to the flow when the jet dimensions exceed the airfoil section span. The airfoil section corresponds to a finite wing and trailing vortices appear at the ends of the span although reduced by the end plates. The trailing vorticity induces a downwash velocity in the case of positive lift coefficient. Due to the downwash the angle of attack is reduced and additional drag is induced.

Both downwash and streamline curvature result in a change in the angle of attack due to the induction of a velocity normal to the flow direction and the airfoil section. It was in [3] showed that for the VELUX test stand downwash is insignificant compared with streamline curvature because of the presence of end plates. However this was not the case in the measurements presented in this report. The span of the airfoil models was 0.03 m too short. It was therefore necessary to introduce a gap between one of the end plates and the test stand. This gap reduced the effective size of one of the endplates causing additional downwash

For the correction of streamline curvature, the method of Brooks and Marcolini [5] was used and an additional term was added to account for the downwash through the gap.

The corrected angle of attack, α, was found from:

$$\alpha = \alpha_t - \frac{\sqrt{3\sigma}}{\pi} c_l - \frac{2\sigma}{\pi} c_l - \frac{\sigma}{\pi}\left(4c_{mt}\right) \; - D\,c_l \quad [rad] \tag{3-1}$$

where

$$\sigma = \frac{\pi^2}{48} \cdot \left(\frac{c}{h}\right)^2 \tag{3-2}$$

The drag coefficient, c_d, is calculated from:

$$c_d = c_{dt} + \left[-\frac{\sqrt{3\sigma}}{\pi} c_l - \frac{2\sigma}{\pi} c_l - \frac{\sigma}{\pi}\left(4c_{Mt}\right) - D\,c_l \right] c_l \tag{3-3}$$

The moment coefficient, c_m, is obtained:

$$c_m = c_{mt} - \frac{\sigma}{2} c_l \tag{3-4}$$

In both (3-1) and (3-3) the term $D\,c_l$ accounted for downwash whereas the other terms accounted for streamline curvature. For details see Fuglsang *et al.* [3].

3.3 Wind tunnel flow conditions

In Fuglsang *et al.* [3] the wind tunnel flow conditions are investigated and it was found that:

- The turbulence intensity at the test section inlet is 1%.
- Between the inlet and the airfoil section, there is a speed-up and a static pressure drop.

During the measurements, the wind tunnel references for static, p_∞ and total pressures, $p_{o\infty}$ were derived from the Pitot 1 measurements located upstream of the test section, Figure 3-1. Comparing the wake rake measurements and the Pitot 1 measurements derived the relation between Pitot 1 and the airfoil section. The flow acceleration between Pitot 1 and the airfoil section was determined to, $\varepsilon_{1\text{-}\infty}$ = 2.1% and the static pressure drop between Pitot 1 and the airfoil section was determined to, $\Delta p_{1\text{-}\infty}$ = 15 Pa/m. They were both taken into account at the calculation of p_∞ and $p_{o\infty}$.

3.4 Calculation methods

The airfoil pressure coefficient, $C_p(s)$, around the airfoil surface, s, is calculated from:

$$C_p(s) = \frac{p_a(s) - p_\infty}{q_\infty} \tag{3-5}$$

Where

$$q_\infty = p_{o\infty} - p_\infty \tag{3-6}$$

The normal force coefficient, c_n, and the tangential force coefficient, c_t, are found from integration of the $C_P(s)$ distribution along the x- and y-axis as seen in Figure 3-4. The airfoil lift coefficient, c_l, and drag coefficient, c_d, are found by resolving c_n and c_t perpendicular to and parallel with the oncoming flow:

$$c_l = \cos(\alpha) c_n + \sin(\alpha) c_t \tag{3-7}$$

$$c_d = -\cos(\alpha) c_t + \sin(\alpha) c_n$$

The moment coefficient, c_m, is found from integration of $C_P(s)$ at $x/c = 0.25$.

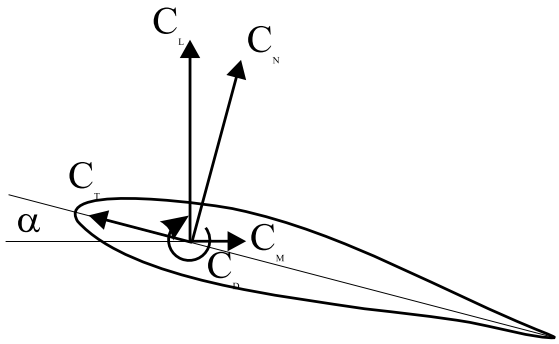

Figure 3-4 Sign convention for aerodynamic coefficients.

The total airfoil drag is the sum of skin friction and pressure drag. By assuming a control surface, which surrounds the airfoil section, the total drag can be calculated from the balance of the momentum flux entering and exiting the control surface. The momentum profile entering is assumed uniform and is calculated from the wind tunnel free stream reference pressures. The momentum profile exiting is calculated from the pressures measured by the wake rake.

Assuming that the flow is 2D, the total wake drag coefficient, c_{dw}, is calculated from Rae and Pope [4]:

$$c_{dw} = \frac{2}{c} \int_{y_{\min}}^{y_{\max}} \sqrt{\frac{p_o(y) - p(y)}{q_\infty}} \cdot \left(1 - \sqrt{\frac{p_o(y) - p(y)}{q_\infty}} \right) dy \tag{3-8}$$

In the analysis of dynamic loads, while the airfoil is in pitching motion, the pitching motion is described by the equation:

$$\alpha = A \sin(\omega t) + \alpha_m \tag{3-9}$$

The pitching motion is related to the reduced frequency:

$$k = \frac{\omega c}{2V_\infty} \tag{3-10}$$

4 Airfoil sections and aerodynamic devices

4.1 Airfoil sections

The tested airfoils were the Risø-B1-18 and Risø-B1-24. For both airfoil sections, the span was 1.9 m. The chord was 0.600m for both airfoils. SSP Technology A/S, Denmark, manufactured both airfoils and carried out the instrumentation of pressure tabs. Risø manufactured the end pieces. Each model was manufactured in two pieces as an upper and a lower shell to facilitate instrumentation. The models were made of fibre glass in moulds. The pressure taps were Ø0.5 mm holes drilled directly in the model surface with the exception of the leading and trailing edges where tubes were installed through the model surface, flush with the surface. Inside the model metal tubes were mounted parallel to the drilled holes and flexible plastic tubes were connected to the metal tubes. When the instrumentation was completed the two shells were assembled. The pressure tubes were taken outside of the model through a hollow axis at one side of the airfoil.

The airfoil sections were equipped with 62 pressure taps in the centre line region. The taps were placed along the chord at the centre line of the model in a staggered alignment to minimise disturbances from upstream taps. Additional taps were drilled close to the centre line as a back up to taps at the leading and trailing edges, and in order to allow measurements away from the centre line.

The position of the pressure taps on the model was decided by looking on the theoretical pressure distributions derived from numerical calculations. The distribution of the pressure taps reflected the expected pressure gradients and the tap spacing was dense at the leading edge. There was more taps on the upper surface compared to the lower surface. After the model was permanently assembled the model dimensions and the tap positions were checked for compliance with the theoretical ones.

There was very good agreement between the theoretical and the measured coordinates. For both airfoil models, it was concluded that this could not result in significant errors in the pressure distribution and in the derivation of aerodynamic loads.

4.2 Leading edge roughness

In some measurements trip tape was mounted on the airfoil model surface to simulate the effects from leading edge roughness (LER). LER appears when dirt, bugs or soil accumulate on the wind turbine blades in dirty environments.

Three different kinds of LER were used:

- 90° zigzag tape of height 0.35 mm
- 60° zigzag tape of height 0.85 mm
- Car customising tape of height 0.12 mm

4.2.1 90° zigzag tape

The used trip tape was originally intended for use on gliders and was manufactured as fibre enforced plastic tape that was glued to the airfoil model surface.

Figure 4-1 shows the 90° zigzag trip tape with a 90° angle, a width of 3 mm and a thickness of 0.35 mm.

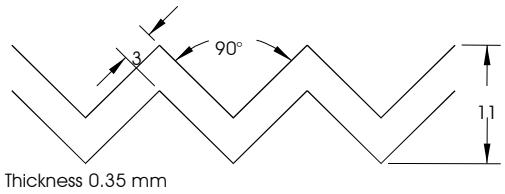

Figure 4-1 Trip tape with 90° zigzag of 3 mm width and 0.35 mm thickness.

The 90° zigzag tape was mounted at different positions:

- At x/c=0.05 on the suction side and at the same time at x/c=0.10 on the pressure side
- From x/c=0, i.e. the leading edge, towards the pressure side
- From x/c=0, i.e. the leading edge, towards the suction side

4.2.2 60° zigzag tape

As for the 90° zigzag tape this trip tape was originally intended for use on gliders and was as well manufactured as fibre enforced plastic tape that was glued to the airfoil model surface.

Figure 4-2 shows the 60° zigzag trip tape with a 60° angle, a width of 3 mm and a thickness of 0.85 mm.

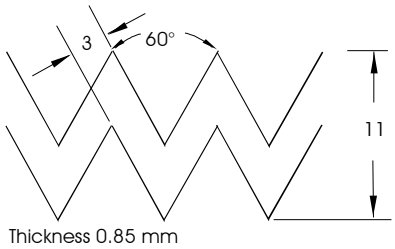

Figure 4-2 Trip tape with 60° zigzag of 3 mm width and 0.85 mm thickness.

The 60° zigzag tape was mounted from x/c=0, i.e. the leading edge, towards the suction side.

4.2.3 Car customising tape

This trip tape was originally intended for use on cars for decoration and was manufactured as plastic tape that was glued to the airfoil model surface.

Figure 4-3 shows the trip tape with a width of 3 mm and a thickness of 0.12 mm.

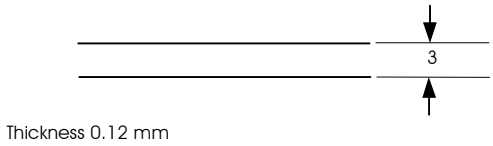

Figure 4-3 Trip tape of 3 mm width and 0.12 mm thickness.

The car customising tape was mounted from *x/c*=0, i.e. the leading edge, towards the suction side.

4.3 Stall strips

In some Risø-B1-18 measurements stall strips (SS) were mounted to the airfoil model surface at the leading edge to modify the stall characteristics. SS are sometimes used on the outer part of wind turbine blades to control power, loads and dynamics at high wind speeds. The stall strips were manufactured in nylon with a span of 1.9m corresponding to the span of the airfoil.

Two different kinds of SS were used:

- Curved SS
- Triangular SS

4.3.1 Curved stall strip

The 'curved SS' were curved on one side to fit the curvature of the leading edge, Figure 4-4.

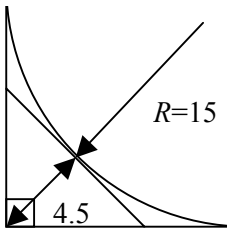

Figure 4-4 Profile view of a curved stall strip used for application on the leading edge.

The curved SS were mounted at three leading edge positions on the Risø-B1-18 airfoil, Table 4-1 and Figure 4-6.

Table 4-1 Positions from the leading edge of the curved SS on the Risø-B1-18 airfoil

Position along surface [mm]	Chord position [%]
0	0
6	0.25
12	0.83

4.3.2 Triangular stall strip

The 'triangular SS' has a triangular profile as shown in Figure 4-5. This is the original shape, which is used on wind turbine blades. In the measurements it was used on locations where the curvature was small. To obtain best possible accordance with full-scale wind turbines the SS were sized to having sides of approximately 1% chord.

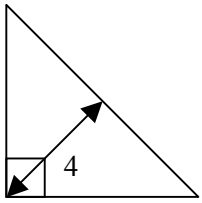

Figure 4-5 Profile view of triangular stall strip.

The triangular SS was mounted at one position on the Risø-B1-18 airfoil, Table 4-2 and Figure 4-6.

Table 4-2 Position of the triangular SS on the Risø-B1-18 airfoil.

Position along surface [mm]	Chord position [%]
18	1.58

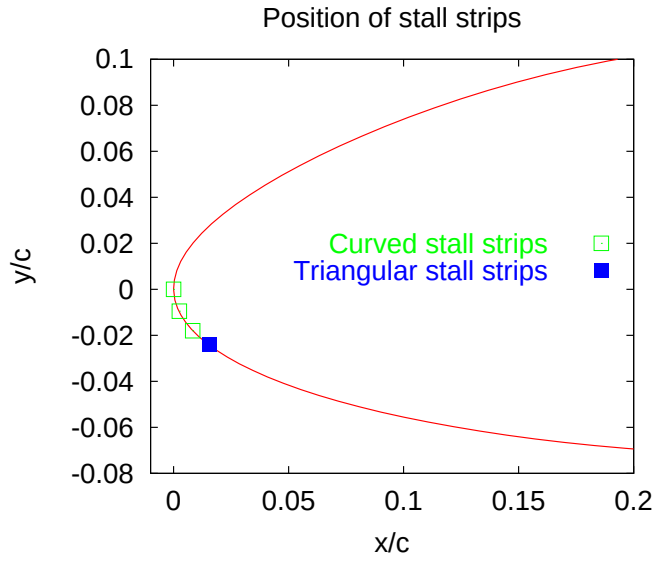

Figure 4-6 Position of curved and triangular SS on the Risø-B1-18 airfoil.

4.4 Vortex generators

In some of the Risø-B1-24 measurements vortex generators (VG's) were used. They are often put on the inner part of wind turbine blades on the blade suction side between 15% and 30% of the chord counted from the leading edge. They increase the maximum lift coefficient by delaying separation on the airfoil suction side to higher incidences. At the same time, they increase the drag coefficient.

The design of the VG's followed the guide lines from Hoerner and Borst [6] and was similar to those used for numerous airfoil tests by Timmer [7], at Delft University, The Netherlands.

Figure *4-7* shows the shapes and dimensions of the used VG's. They have a height of 6 mm and a length of 18 mm. The angles relative to the chord direction are ±19.5°.

The leading edge spacing between two VG's is 10 mm and the distance between two consecutive pairs is 25 mm. They are of the Delta wing type with a shape of orthogonal triangles and they are placed with their right-angle perpendicular to the airfoil surface and their height increases towards the trailing edge. The presence of the VG's results in the formation of counter-rotating vortices, which transfer higher momentum fluid down to the airfoil surface and thus delay separation. To achieve this VG's are arranged in pairs at equal and opposite angles relative to the chord of the blade.

The VG's were constructed from 0.2 mm thick stainless steel. Each VG was cut out and bent perpendicular to the surface. The VG's were glued on the airfoil model surface separately. The thickness of the gluing surface will slightly disturb the measurements since the flow has to enforce the edge of the gluing surface. In particular the drag coefficient at low angles of attack will be increased.

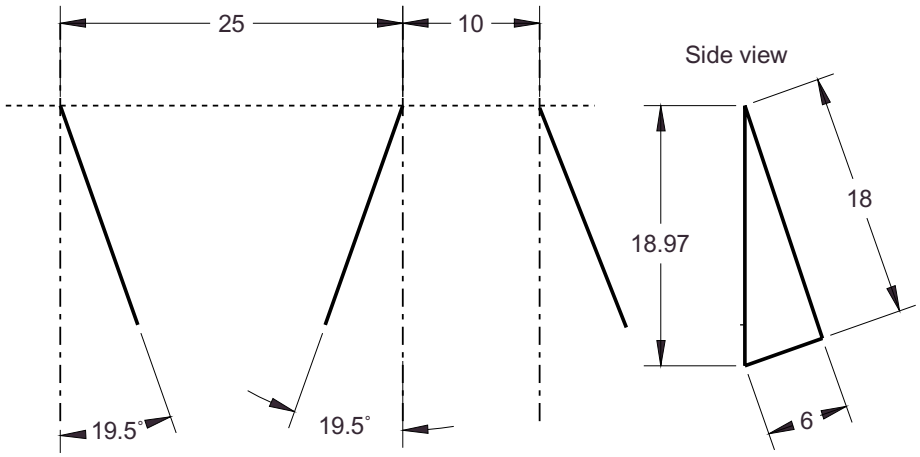

Figure 4-7 Vortex generators of height 6 mm, length 18 mm.

4.5 Gurney flaps

In some measurements of Risø-B1-24 Gurney flaps (GF's) were used. They are sometimes used on the inner part of wind turbine blades at the blade pressure side trailing edge. They increase the maximum lift coefficient by increasing the effective camber of the aft part of the airfoil and hence pressure difference between the lower and the upper sides at the trailing edge. At the same time, they increase the drag coefficient.

Figure 4-8 to Figure 4-10 show the shapes and dimensions of the five used GF's. They had a height of between 3 and 12mm and varied from triangular shapes made by nylon to bent sheets of 0.5mm thick aluminium. The Gurney flaps had a length of 1.9m corresponding to the span of the airfoil. The five tested GF's were:

- Nylon triangles:
  - Height of 0.5% chord length corresponding to 3mm
  - Height of 1.0% chord length corresponding to 6mm
  - Height of 2.0% chord length corresponding to 12mm
- Bent aluminium sheets:
  - Height of 1.0% chord length corresponding to 6mm and bent 90°
  - Height of 1.0% chord length corresponding to 6mm and bent 120°

With these GF shapes both the performance at different heights and at different shapes could be measured.

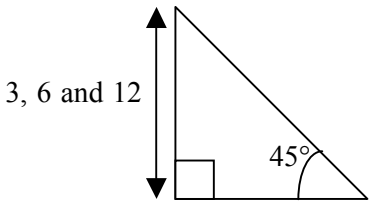

Figure 4-8 Gurney flap of three different heights 3mm, 6mm and 12mm. It was manufactured from nylon.

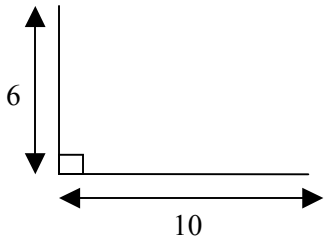

Figure 4-9 Gurney flap of 6mm height and bent 90°. It was manufactured from a 0.5mm thick aluminium sheet.

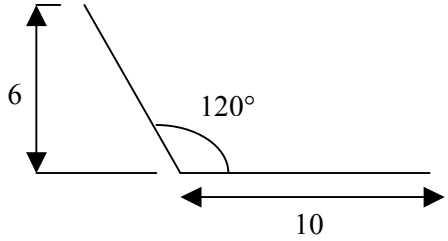

Figure 4-10 Gurney flap of 6mm height and bent 120°. It was manufactured from a 0.5mm thick aluminium sheet.

5 Results

The measurements for Risø-B1-18 and Risø-B1-24 airfoil are reported in Chapter 6 and 7. All shown results were corrected for wind tunnel boundary conditions and the aerodynamic forces were referenced to the wind tunnel free stream flow obtained from Pitot 1 taking into account speed-up and pressure loss as explained in Chapter 3, Fuglsang *et al.* [3].

The different types of conducted measurements are described in Appendix A.

5.1 Testing conditions

The testing conditions are shown in Table 5-1.

Table 5-1 Testing conditions

Airfoil chord	$c = 0.600$ m
Flow velocity	$v = 42$ m/s
Reynolds number	$Re = 1.6 \times 10^6$
Dynamic inflow	
Angular velocity	$\omega = 13.8$ *rad/s*
Reduced frequency	$k = 0.09$
Amplitude	$1.7^o < A < 2.7^o$

5.2 Numerical calculations

The smooth flow measurements were compared with numerical calculations. The Ellipsys2D Navier-Stokes code, Sørensen [8], with the k-ω SST turbulence model, Menter [9], was used for turbulent flow calculations. Free transition was modelled using the Michel transition criteria, Michel [10]. On both the suction and the pressure sides, the flow was laminar upstream of the predicted location of the transition point and fully turbulent downstream of the transition point.

5.3 Presentation of results

Chapter 6 presents the results from the Risø-B1-18 airfoil and Chapter 7 the results from the Risø-B1-24 airfoil. Chapter 6 and 7 contains measurements as shown in Table 5-2.

Results were presented for the airfoil pressure distribution $C_P(x)$ around the airfoil and force coefficients versus angle of attack:

- Lift force, c_l
- Drag force, c_d
- Moment, c_m
- Normal force orthogonal to the chord, c_n
- Driving force in the chord direction, c_t.

For the different measurements the acronyms shown in Table 5-3 were used to identify aerodynamic devices and the surface conditions.

Table 5-2 Measurements for each airfoil.

Smooth flow	**No aerodynamic devices and a clean airfoil surface.**
Leading edge roughness	Various kinds of roughness tape at different positions at the leading edge.
Stall strips	Stall strips at different positions at the leading edge (Only for Risø-B1-18).
Vortex generators	Vortex generators at different positions at the suction side (Only for Risø-B1-24).
Gurney flaps	Gurney flaps of different sizes and shapes at the very trailing edge on the pressure side (Only for Risø-B1-24).
Combined vortex generators and Gurney flaps	Vortex generators and Gurney flaps in combination (only for Risø-B1-24).
Dynamic stall	Measurements with an oscillating airfoil with no aerodynamic devices.

Table 5-3 Description of acronyms to describe the devices and their positions on the airfoil.

Smooth flow	
Smooth	Clean airfoil surface with no devices
Leading edge roughness	
ZZ60	60^o Zigzag tape
ZZ90	90^o Zigzag tape
TT 1	One layer of car customizing tape
TT 2	Two layers of car customizing tape
Positions of leading edge roughness	
s.s.	From the very leading edge towards the suction side
p.s.	From the very leading edge towards the pressure side
5%/10%	LER placed on x/c=5% on suction side and 10% on pressure side
Stall strips	
X% SS	Stall Strips placed X% chord length from the leading edge at the pressure side measured along the surface
Vortex generators	
VG X%	Vortex Generators placed X% chord length from the leading edge at the suction side measured along the chord line, Figure 4-7
Gurney flaps	
GF X%	Gurney Flaps with a height of X% chord length placed at the very trailing edge at the pressure side.
Gurney flap shapes	
Triangle	Nylon triangle as shown in Figure 4-8
90° angle	Aluminum sheet bent 90^o as shown in Figure 4-9
120° angle	Aluminum sheet bent 120^o as shown in Figure 4-10

6 Results for Risø-B1-18

6.1 Risø-B1-18, smooth flow (run024)

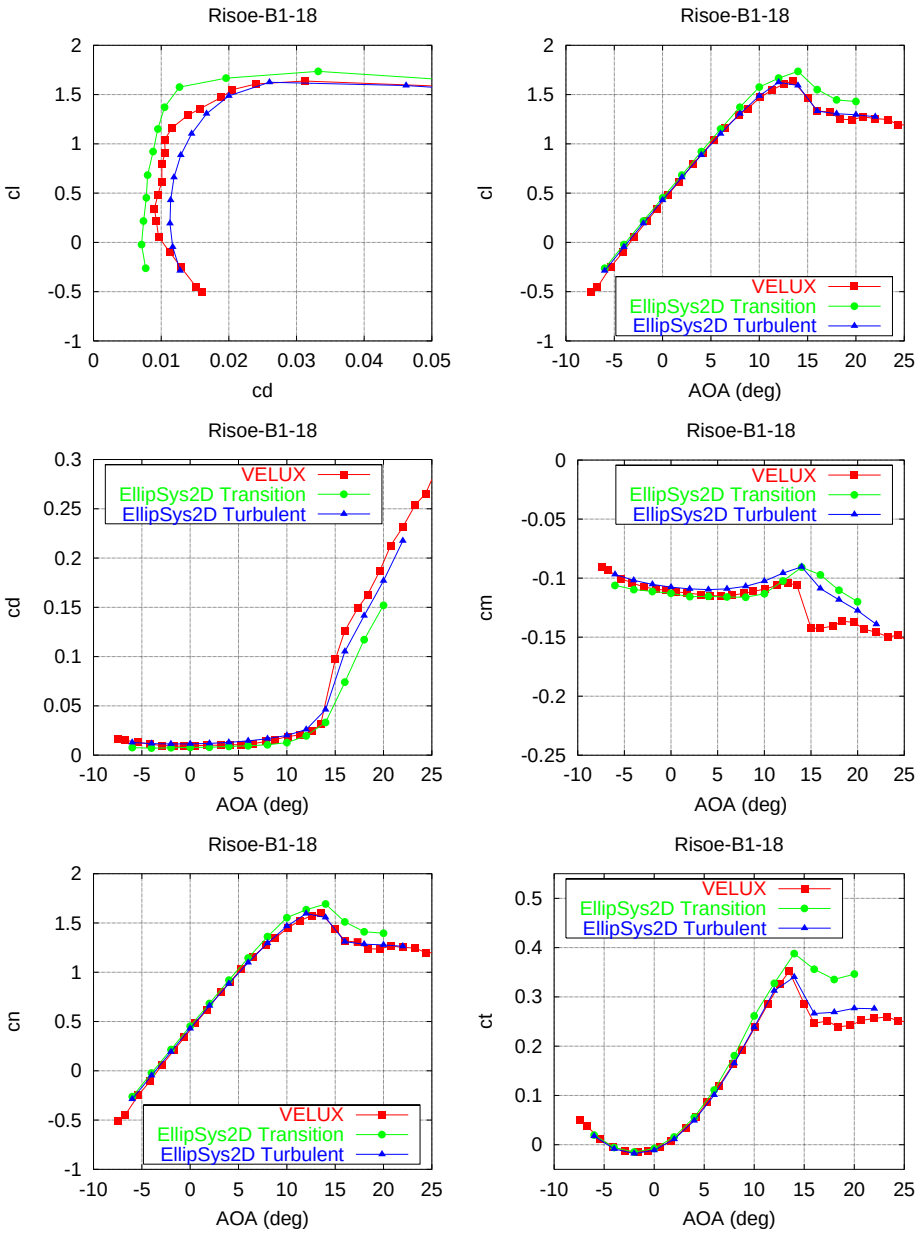

Figure 6-1 Comparison of Risø-B1-18 smooth flow VELUX measurement and EllipSys2D transition and turbulent flow predictions (run024).

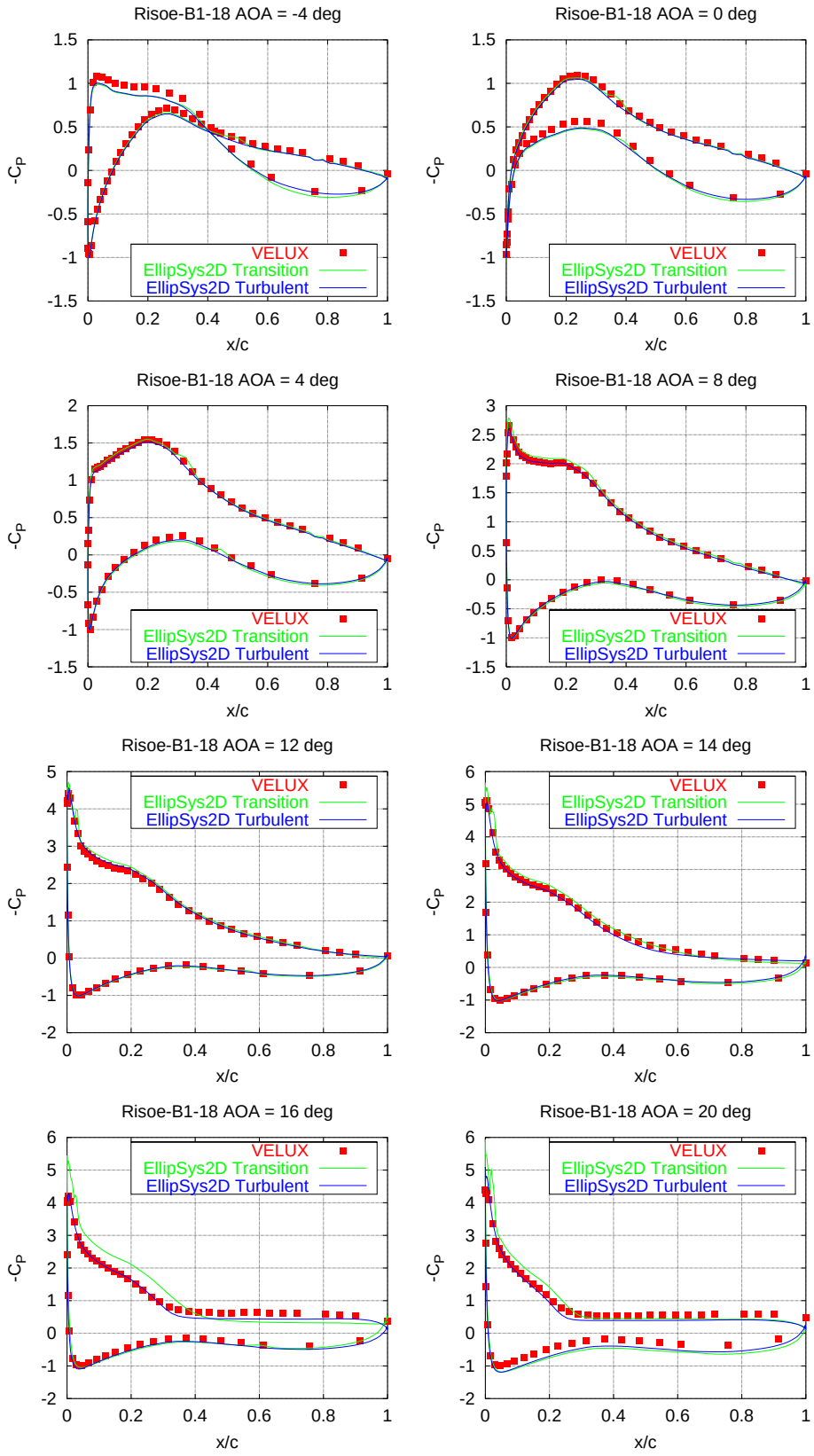

Figure 6-2 C_P at different angles of attack for Risø-B1-18 smooth flow VELUX measurement and EllipSys2D transition and turbulent flow predictions (run024).

6.2 Risø-B1-18, leading edge roughness (run 025, 026, 030, 031, 032, 033)

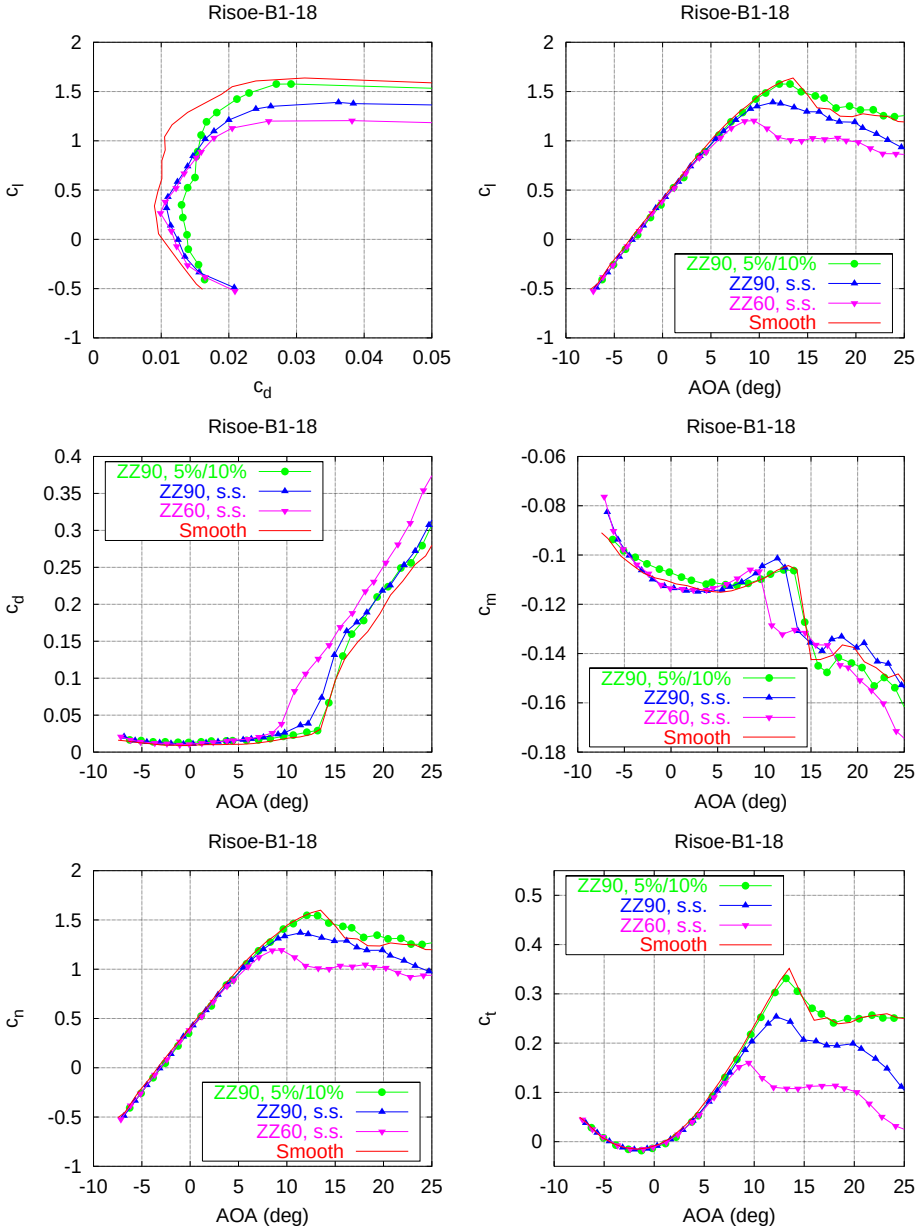

Figure 6-3 Comparison of Risø-B1-18 with leading edge roughness (run 030, 031, 033) and smooth flow (run024).

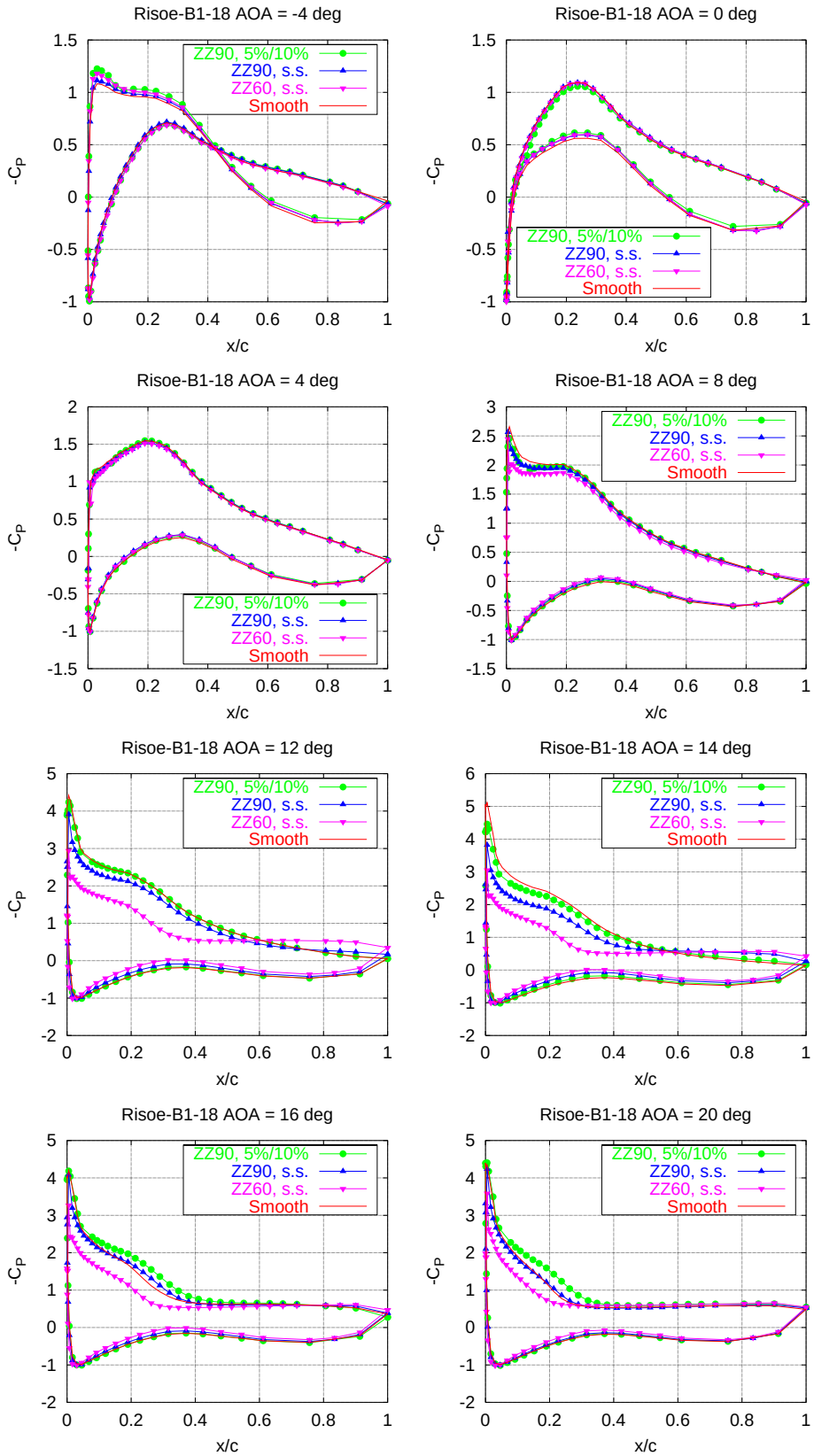

Figure 6-4 C_P at different angles of attack for Risø-B1-18 with leading edge roughness (run 030, 031, 033) and smooth flow (run024).

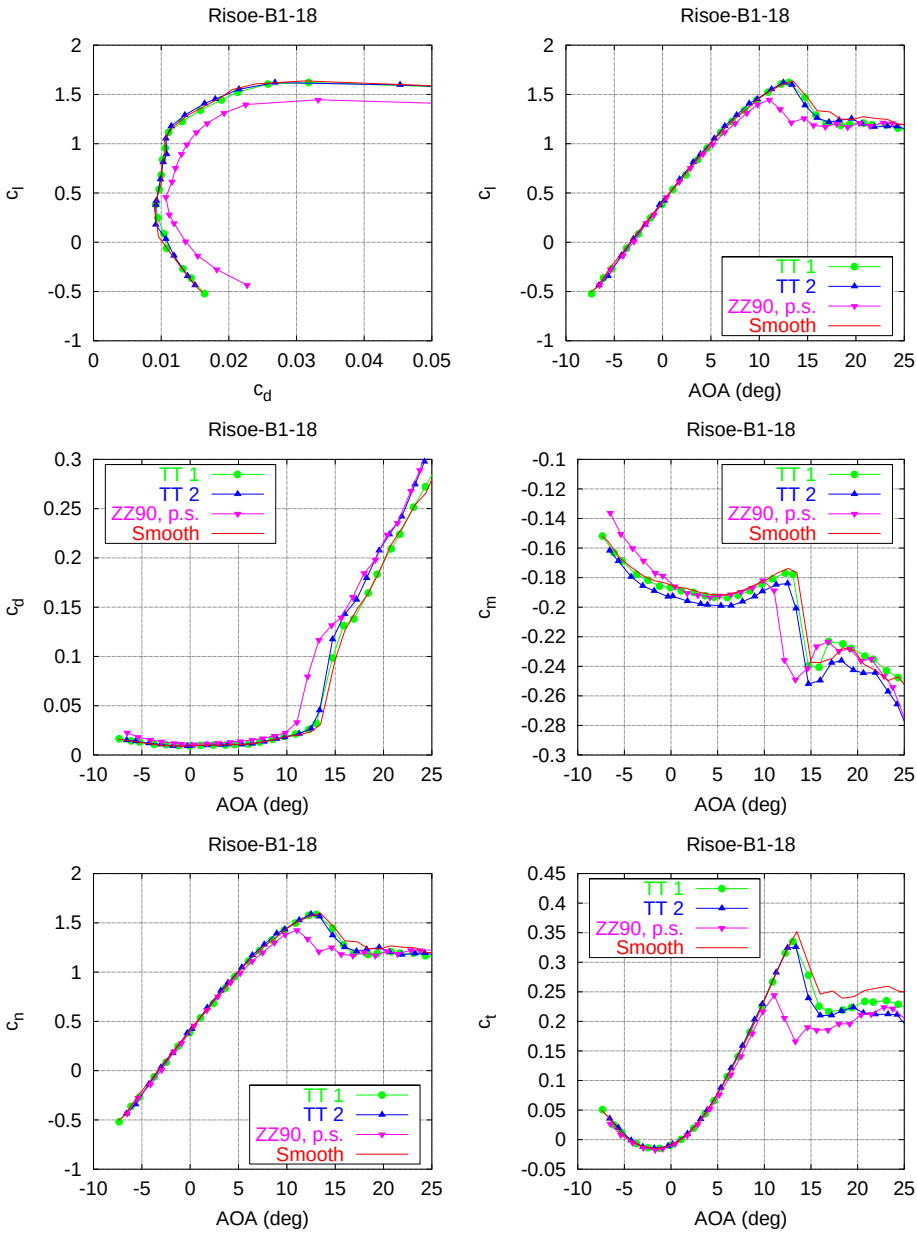

Figure 6-5 Comparison of Risø-B1-18 with leading edge roughness (run 025, 026, 032) and smooth flow (run024).

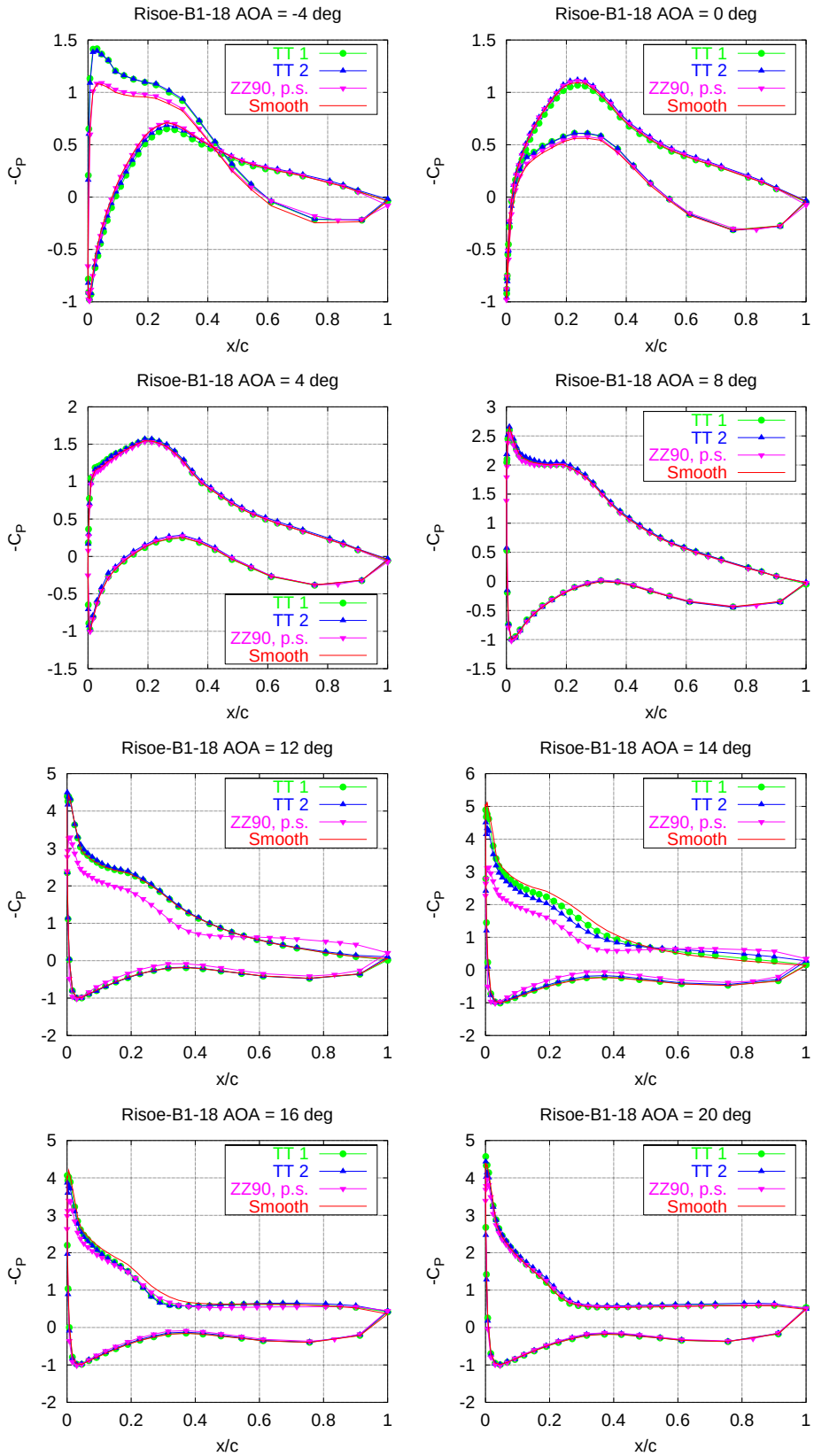

Figure 6-6 C_P at different angles of attack for Risø-B1-18 with leading edge roughness (run 025, 026, 032) and smooth flow (run024).

6.3 Risø-B1-18, stall strips (run 034, 035, 036, 038)

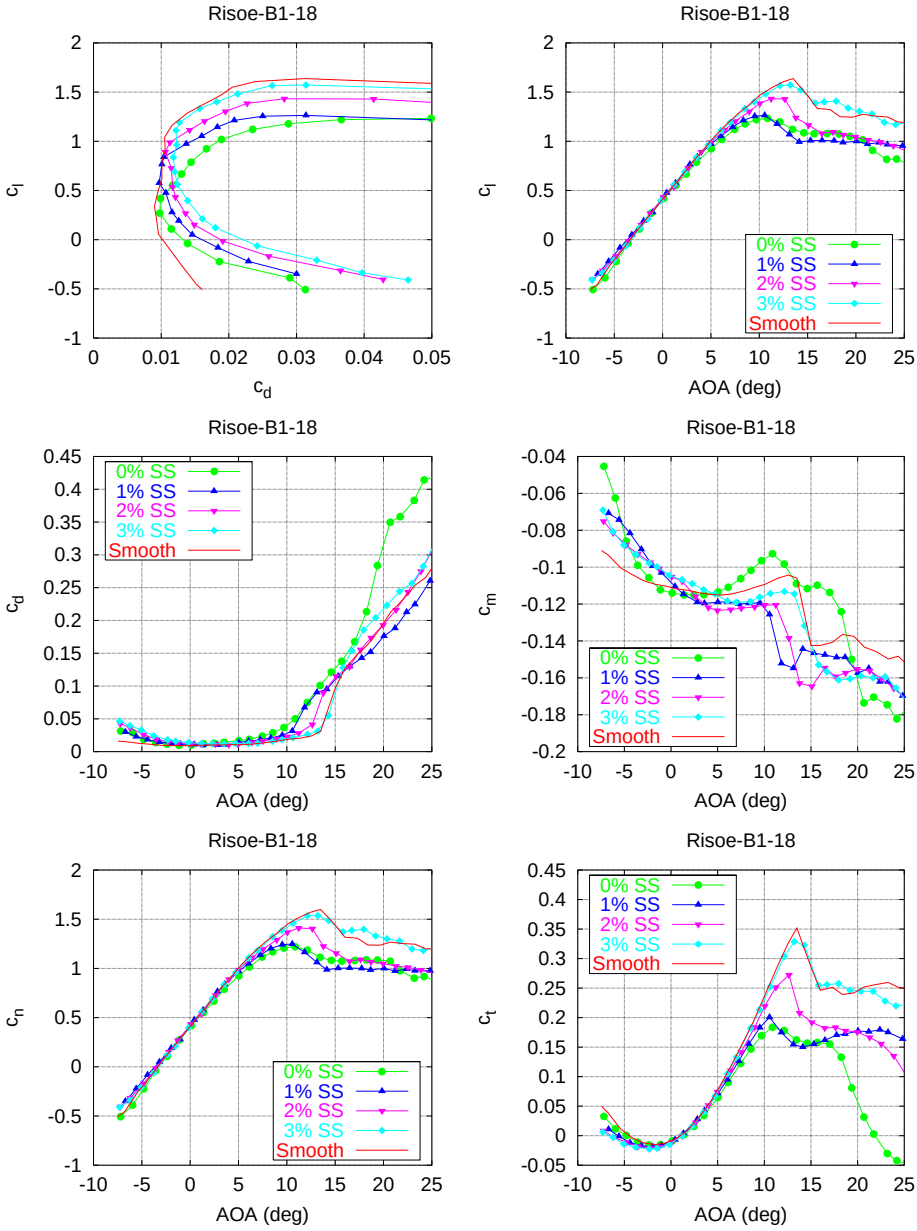

Figure 6-7 Comparison of Risø-B1-18 with stall strips (run 030, 031, 033) and smooth flow (run024).

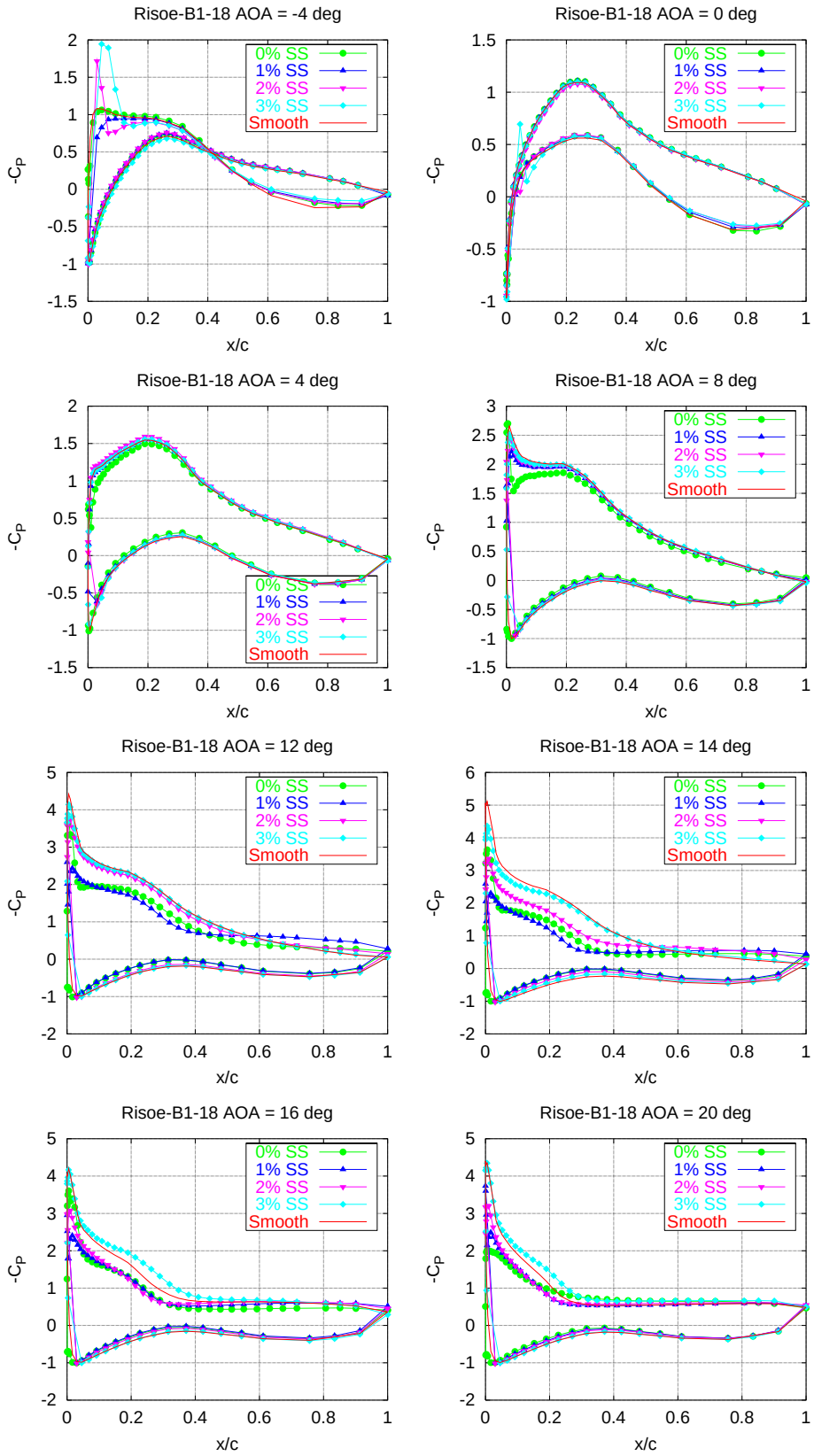

Figure 6-8 C_P at different angles of attack for Risø-B1-18 with stall strips (run 030, 031, 033) and smooth flow (run024).

6.4 Risø-B1-18, dynamic stall (run 029)

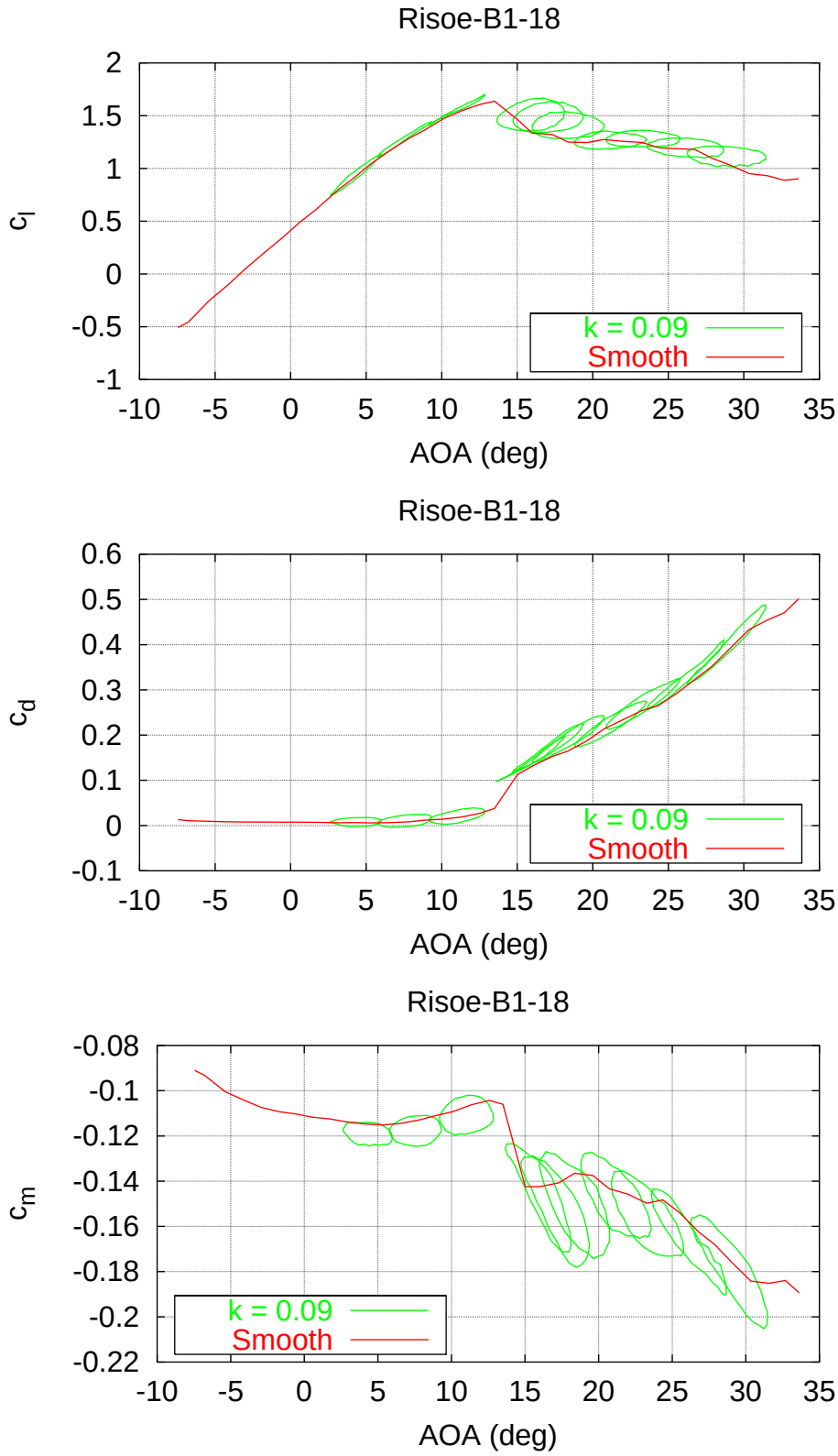

Figure 6-9 Risø-B1-18 c_l, c_d and c_m hysteresis loops for smooth flow, k = 0.092, A between 1.7° and 2.6° (run 029).

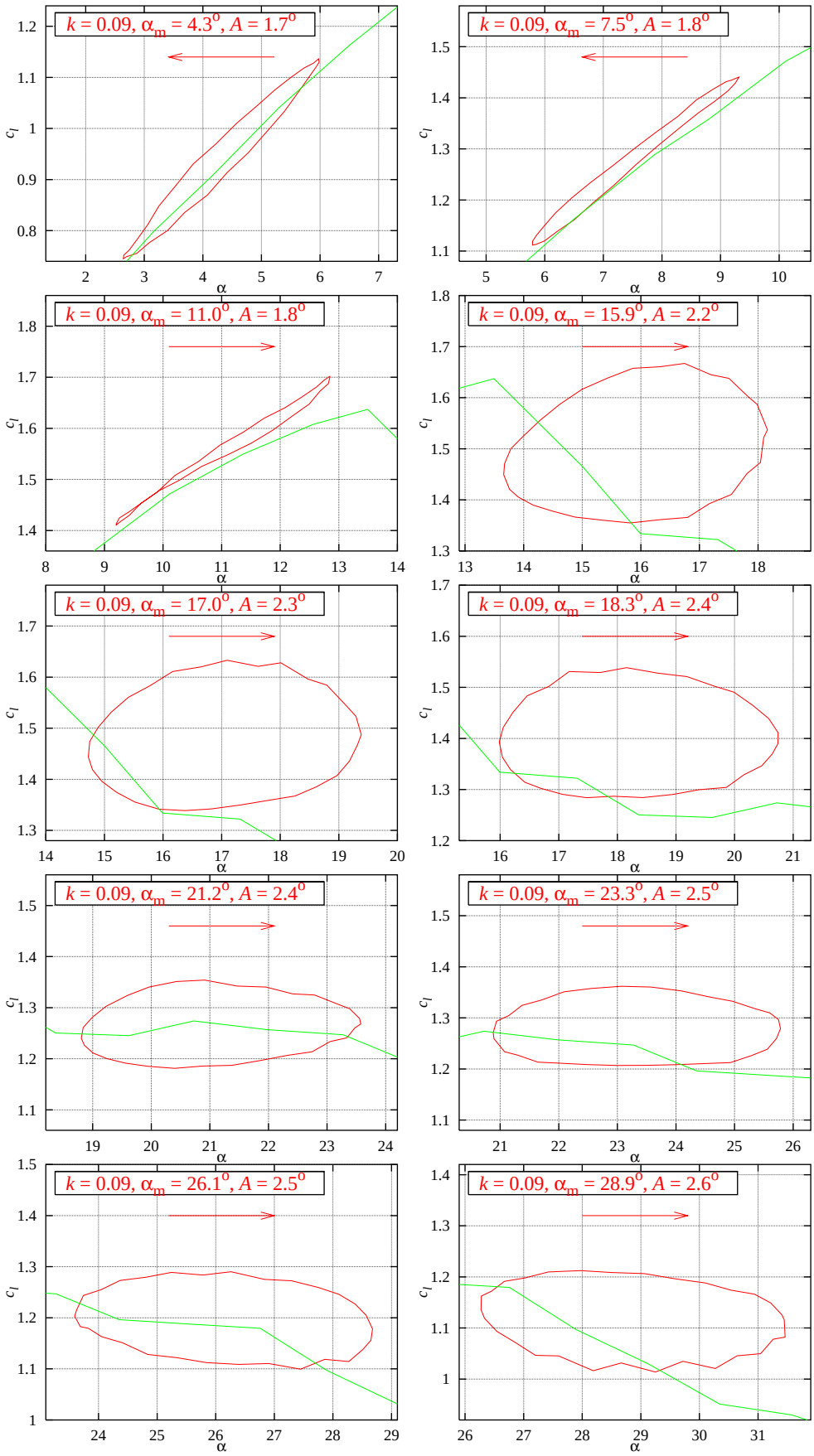

Figure 6-10 Risø-B1-18 c_l hysteresis loops for smooth flow at k = 0.09, A between 1.7° and 2.6° (run 029).

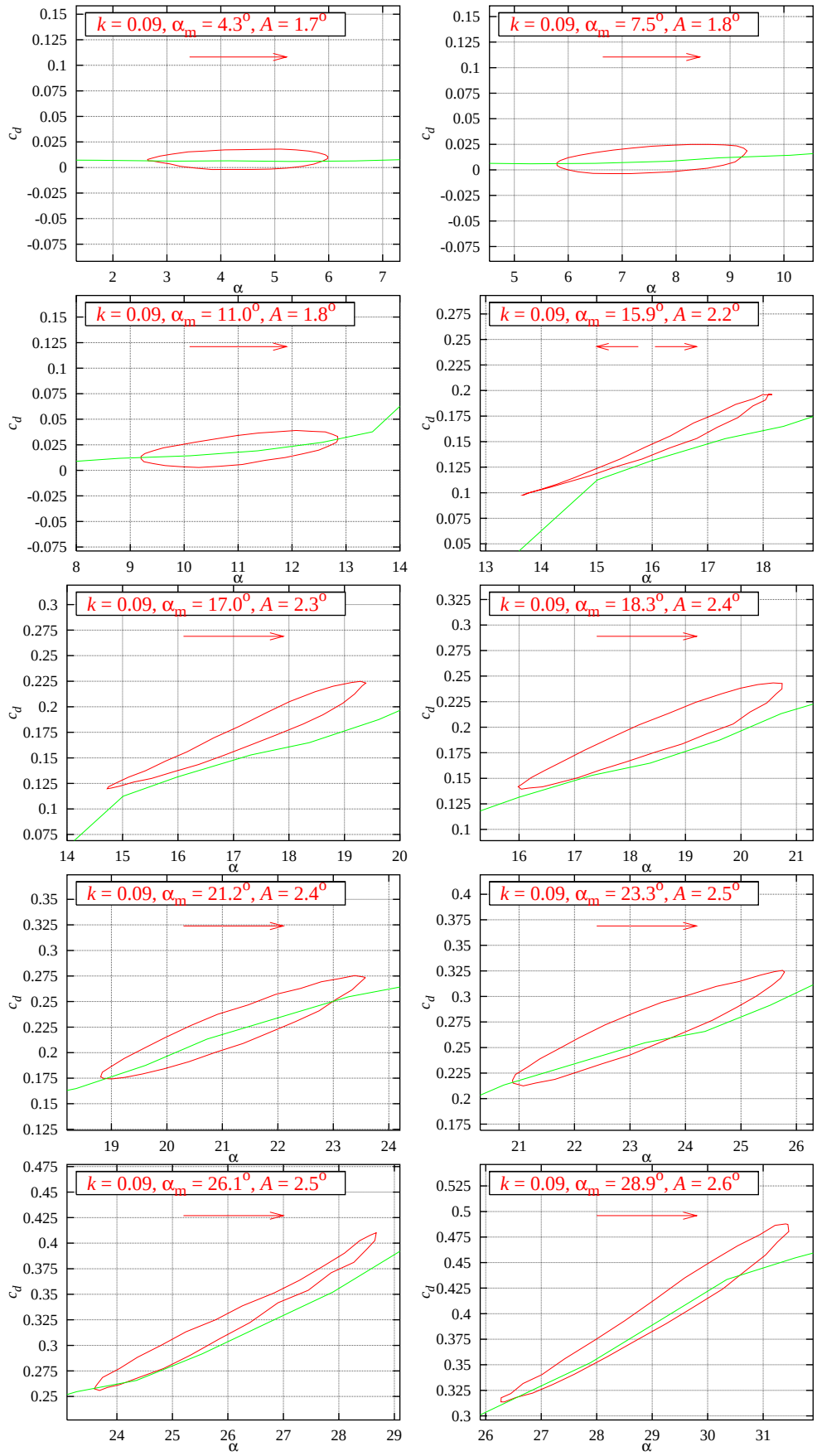

Figure 6-11 Risø-B1-18 c_d hysteresis loops for smooth flow at k = 0.09, A between 1.7° and 2.6° (run 029).

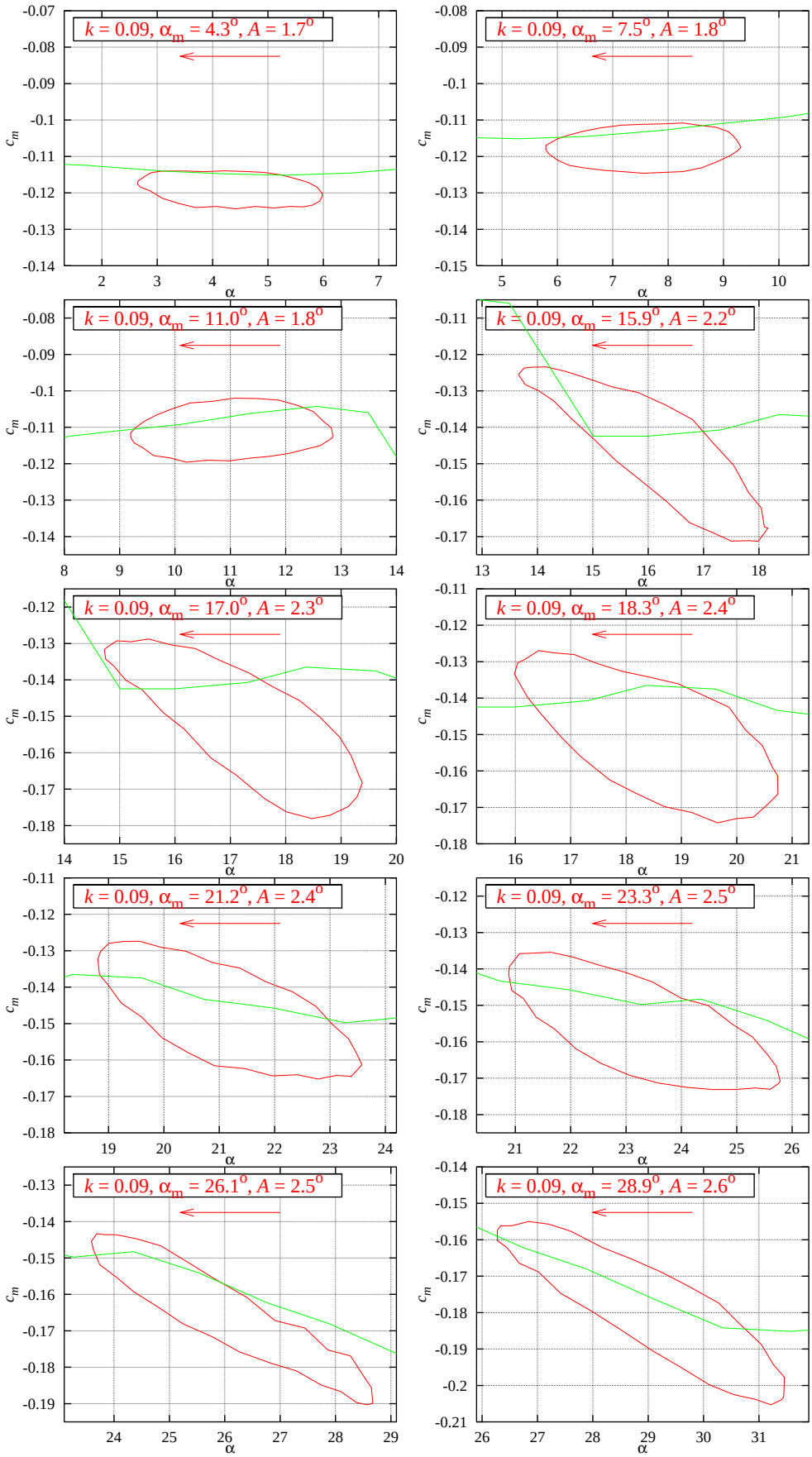

Figure 6-12 Risø-B1-18 c_m hysteresis loops for smooth flow at $k = 0.09$, A between 1.7° and 2.6° (run 029).

7 Results for Risø-B1-24

7.1 Risø-B1-24, smooth flow (run002)

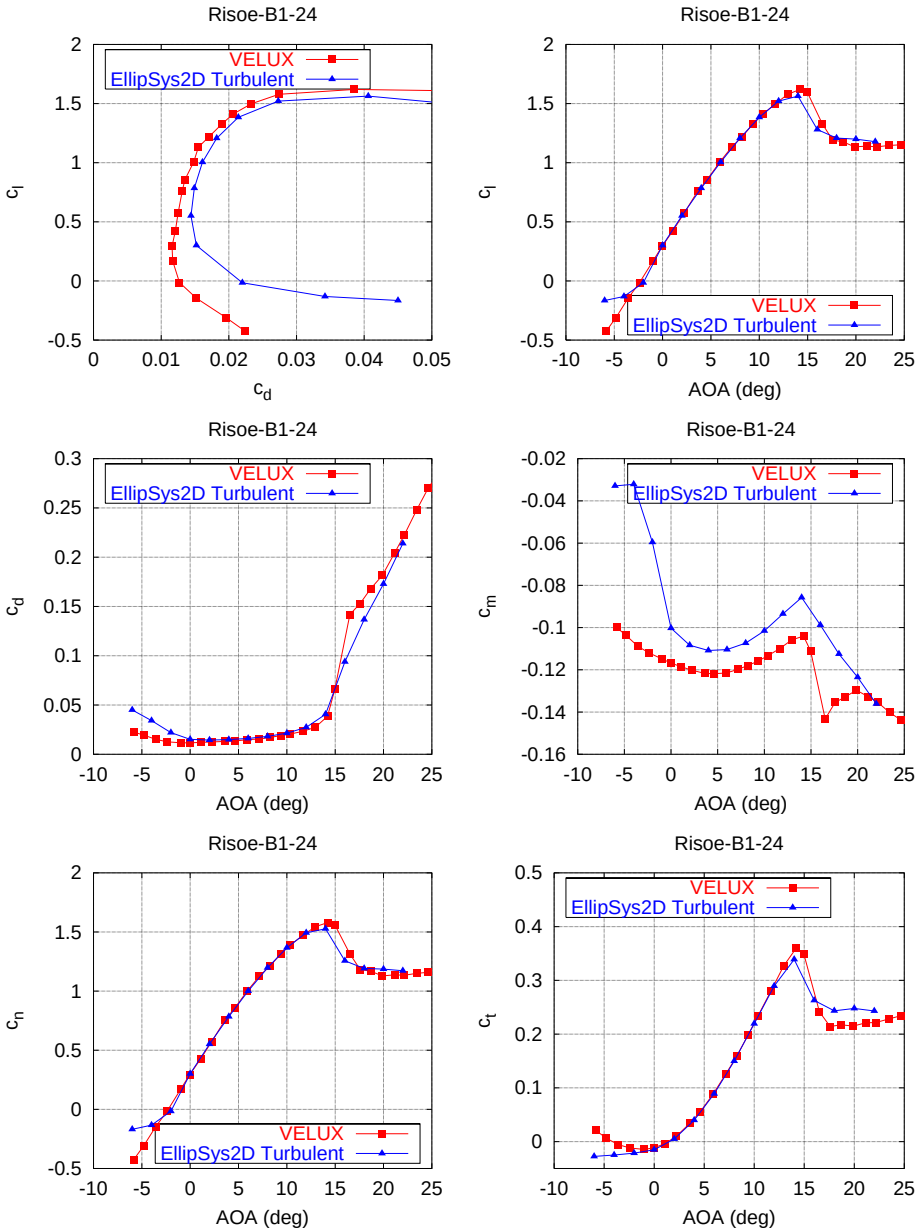

Figure 7-1 Comparison of Risø-B1-24 smooth flow VELUX measurement and EllipSys2D turbulent flow prediction (run 002).

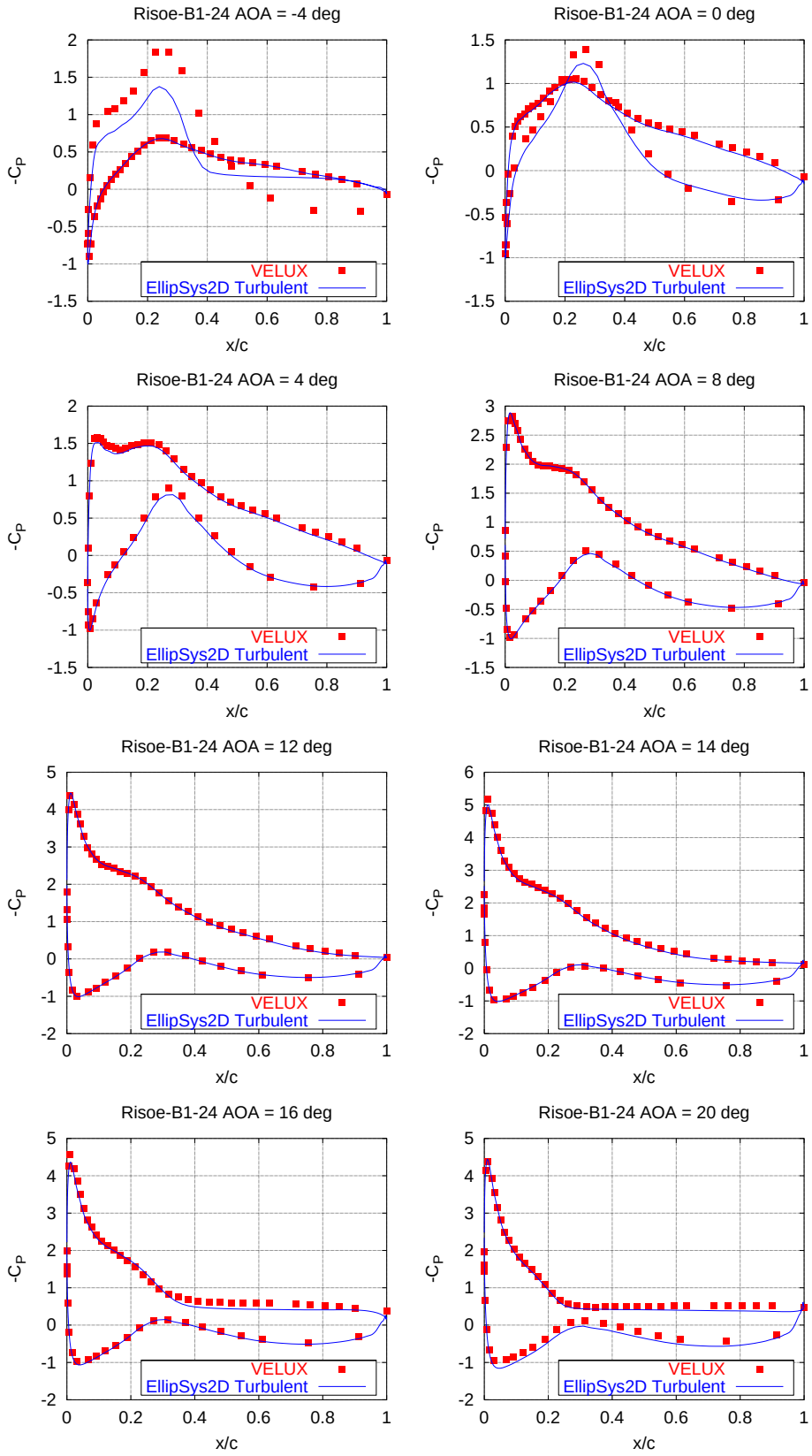

Figure 7-2 C_P at different angles of attack for Risø-B1-24 smooth flow VELUX measurement and EllipSys2D turbulent flow prediction (run 002).

7.2 Risø-B1-24, leading edge roughness (run 006, 007, 008)

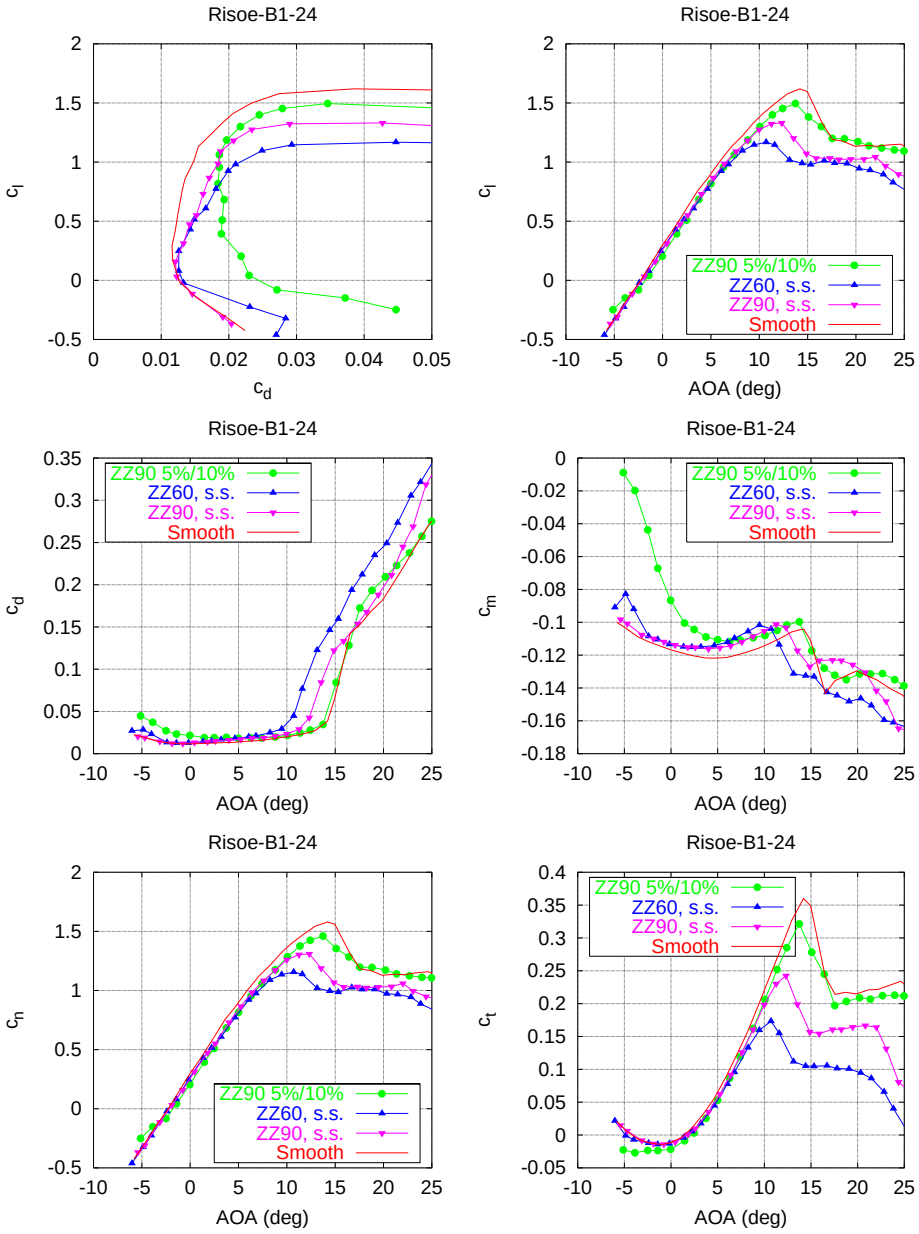

Figure 7-3 Comparison of Risø-B1-24 with leading edge roughness (run 006, 007, 008) and smooth flow (run002).

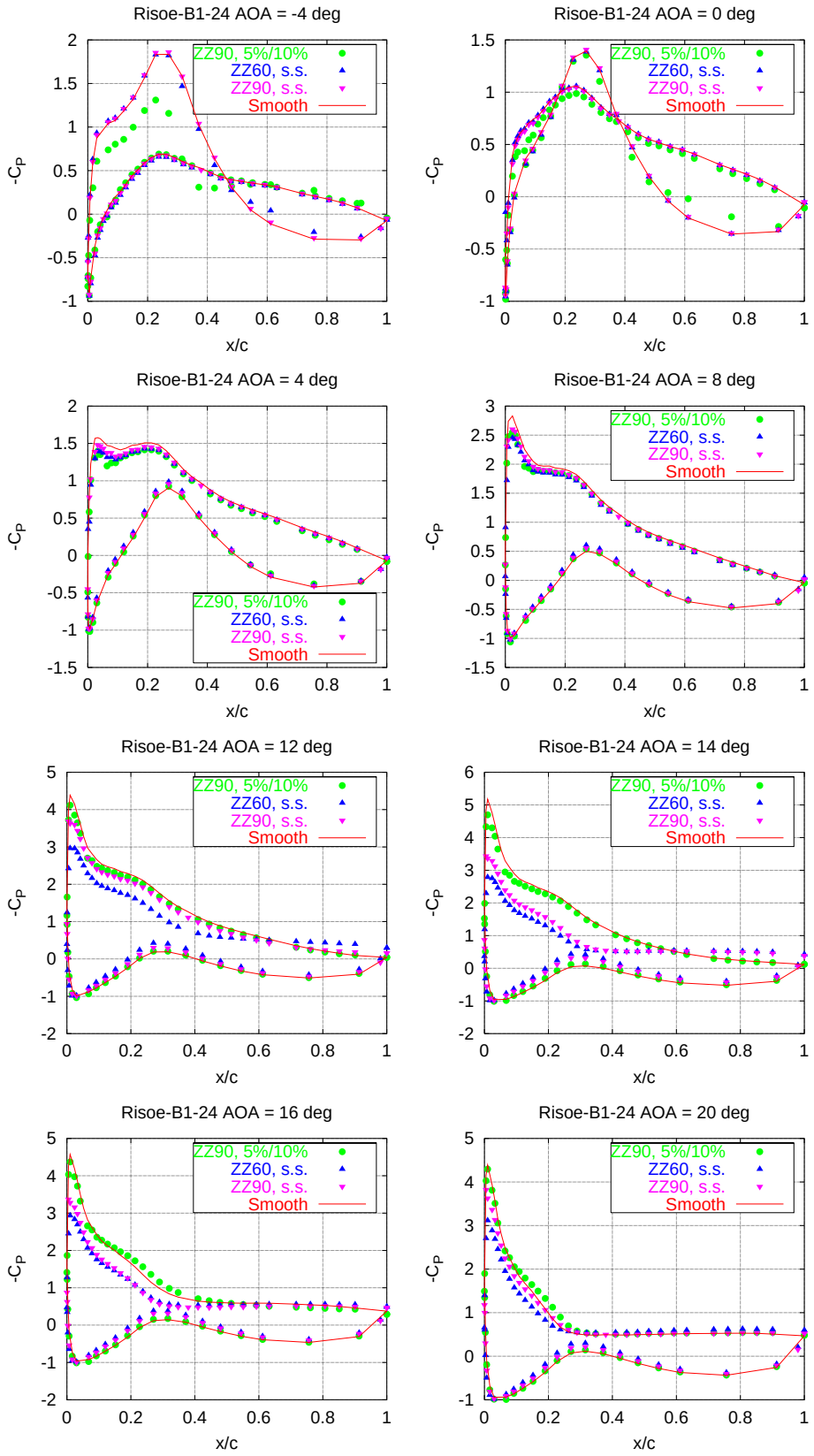

Figure 7-4 C_P at different angles of attack for Risø-B1-24 with leading edge roughness (run 006, 007, 008) and smooth flow (run002).

7.3 Risø-B1-24, vortex generators (run 012, 016, 017)

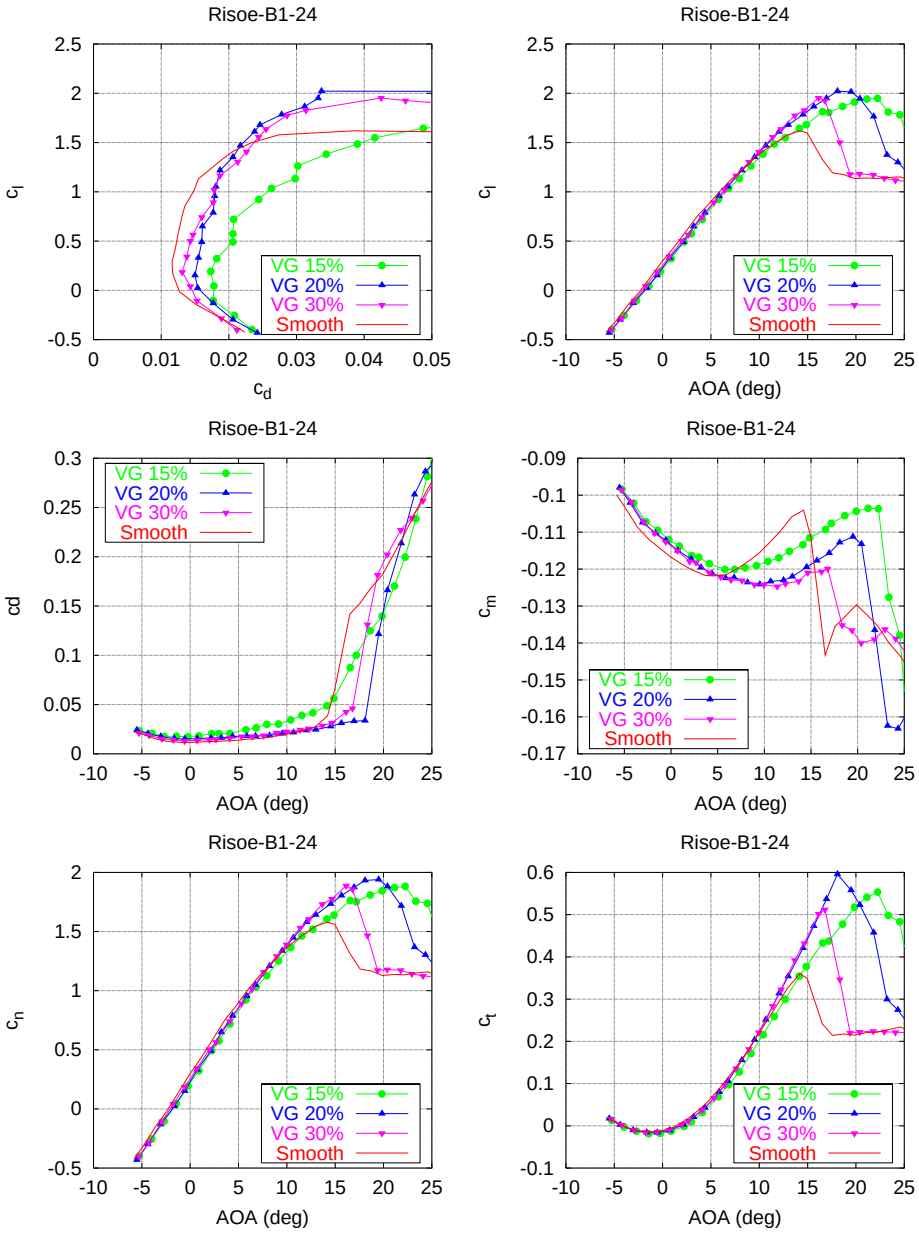

Figure 7-5 Comparison of Risø-B1-24 with vortex generators at various chord positions (run 012, 016, 017) and smooth flow (run002).

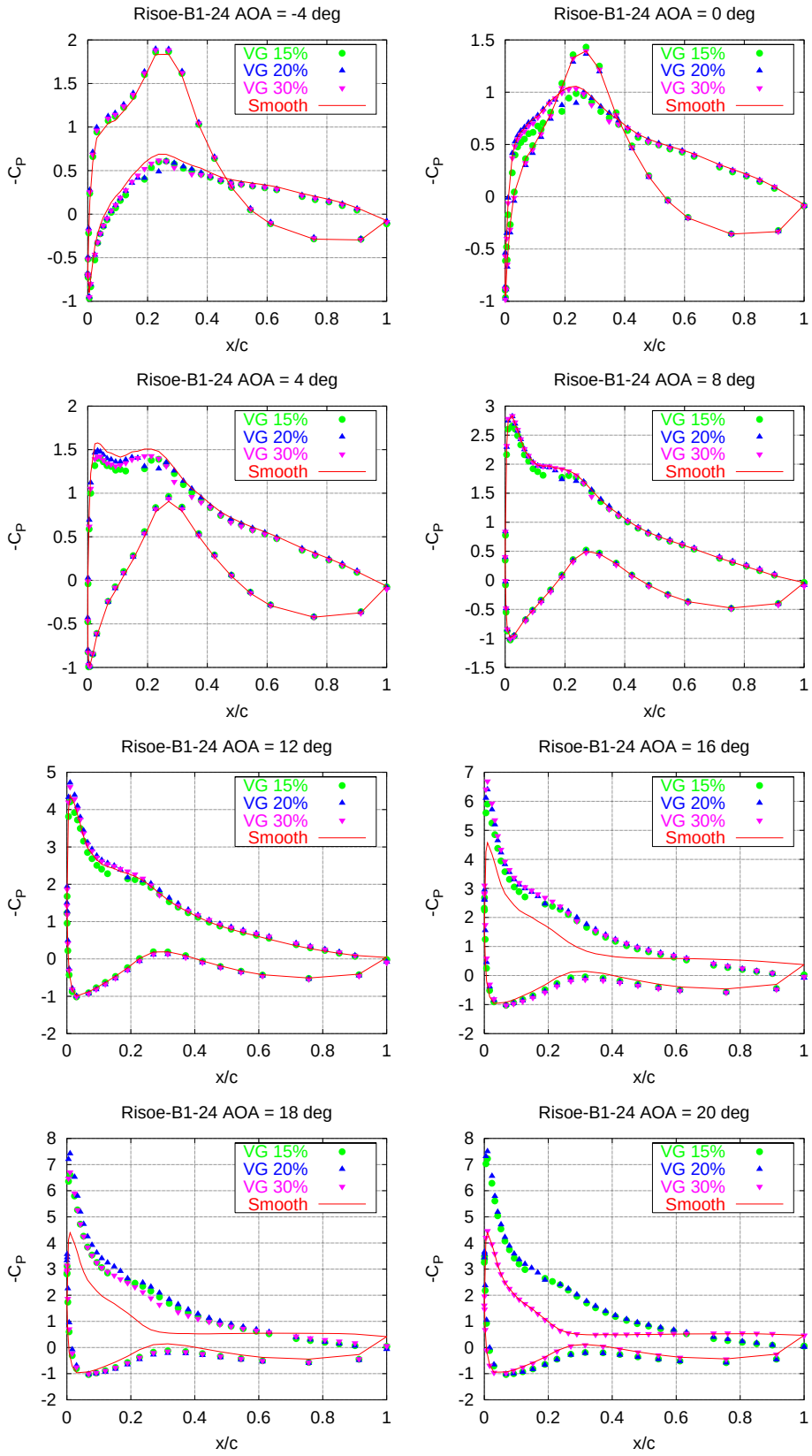

Figure 7-6 C_P at different angles of attack for Risø-B1-24 with vortex generators at various chord positions (run 012, 016, 017) and smooth flow (run002).

7.4 Risø-B1-24, vortex generators at x/c = 0.20, leading edge roughness (run 009, 012)

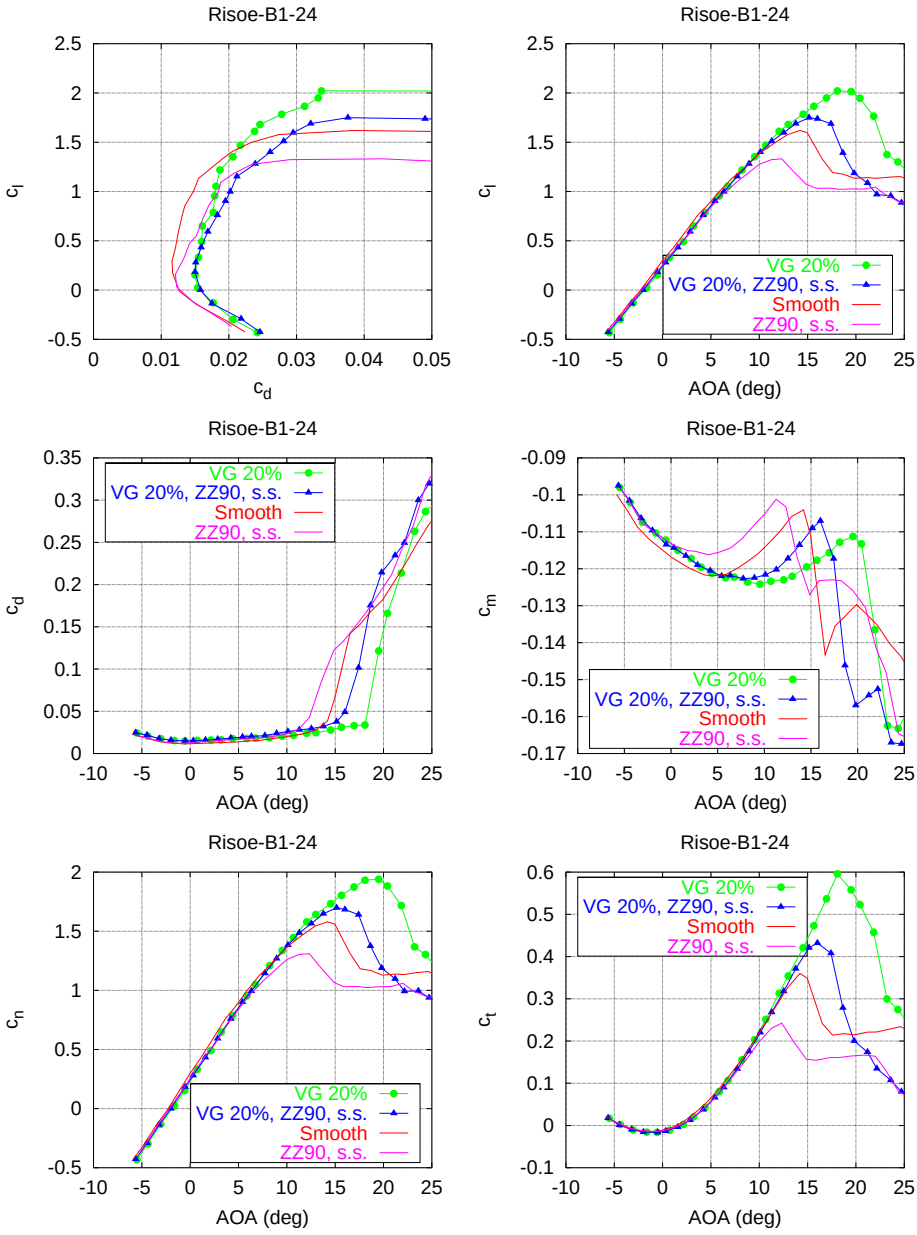

Figure 7-7 Risø-B1-24 with vortex generators at x/c = 0.20 (run 012) and leading edge roughness (run 009) compared with smooth flow (run002).

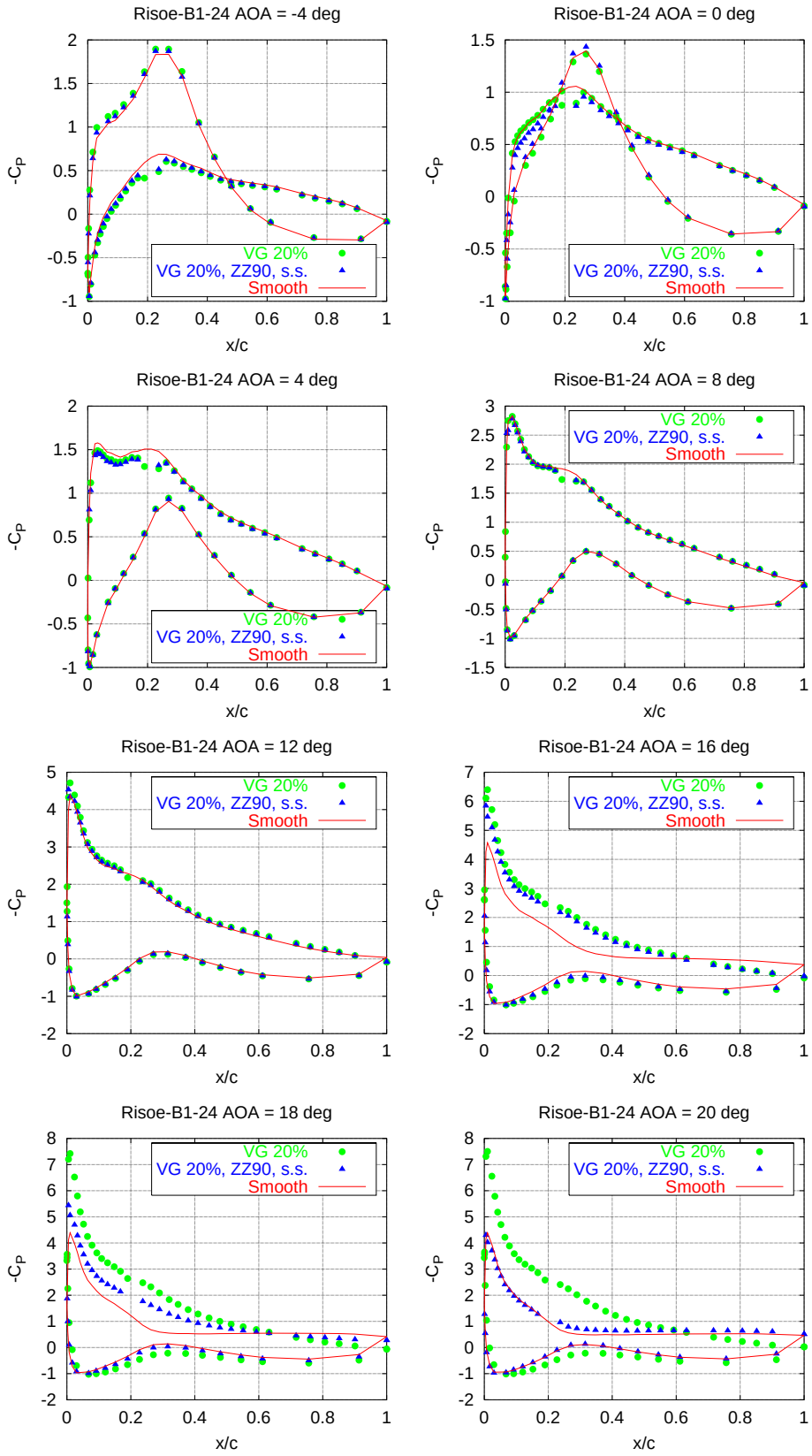

Figure 7-8 C_P at different angles of attack for Risø-B1-24 with vortex generators at x/c = 0.20 (run 012) and leading edge roughness (run 009) compared with smooth flow (run002).

7.5 Gurney flaps (run 013, 018, 019, 020, 021)

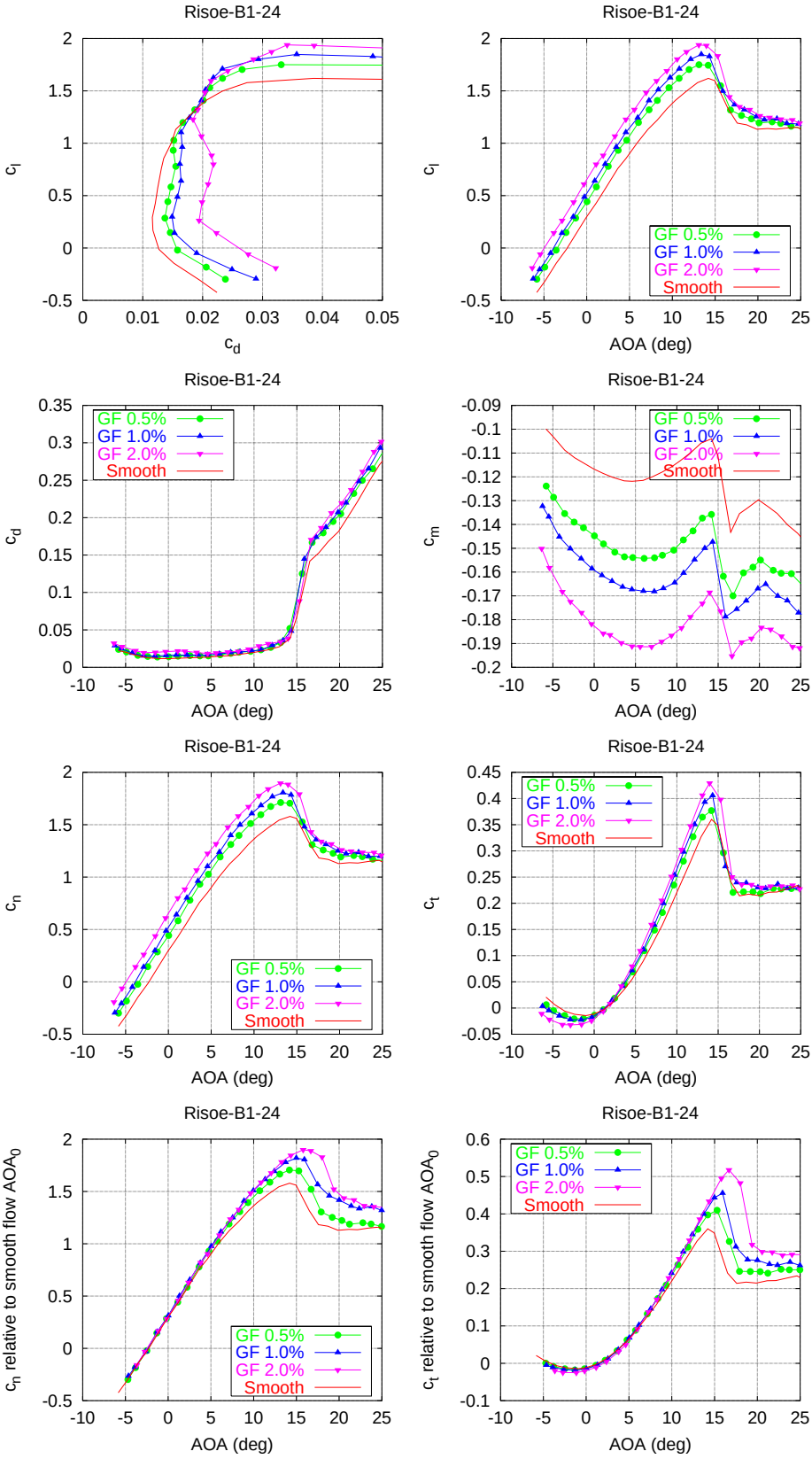

Figure 7-9 Risø-B1-24 with Gurney flaps of different height (run 013, 018, 019) compared with smooth flow (run002).

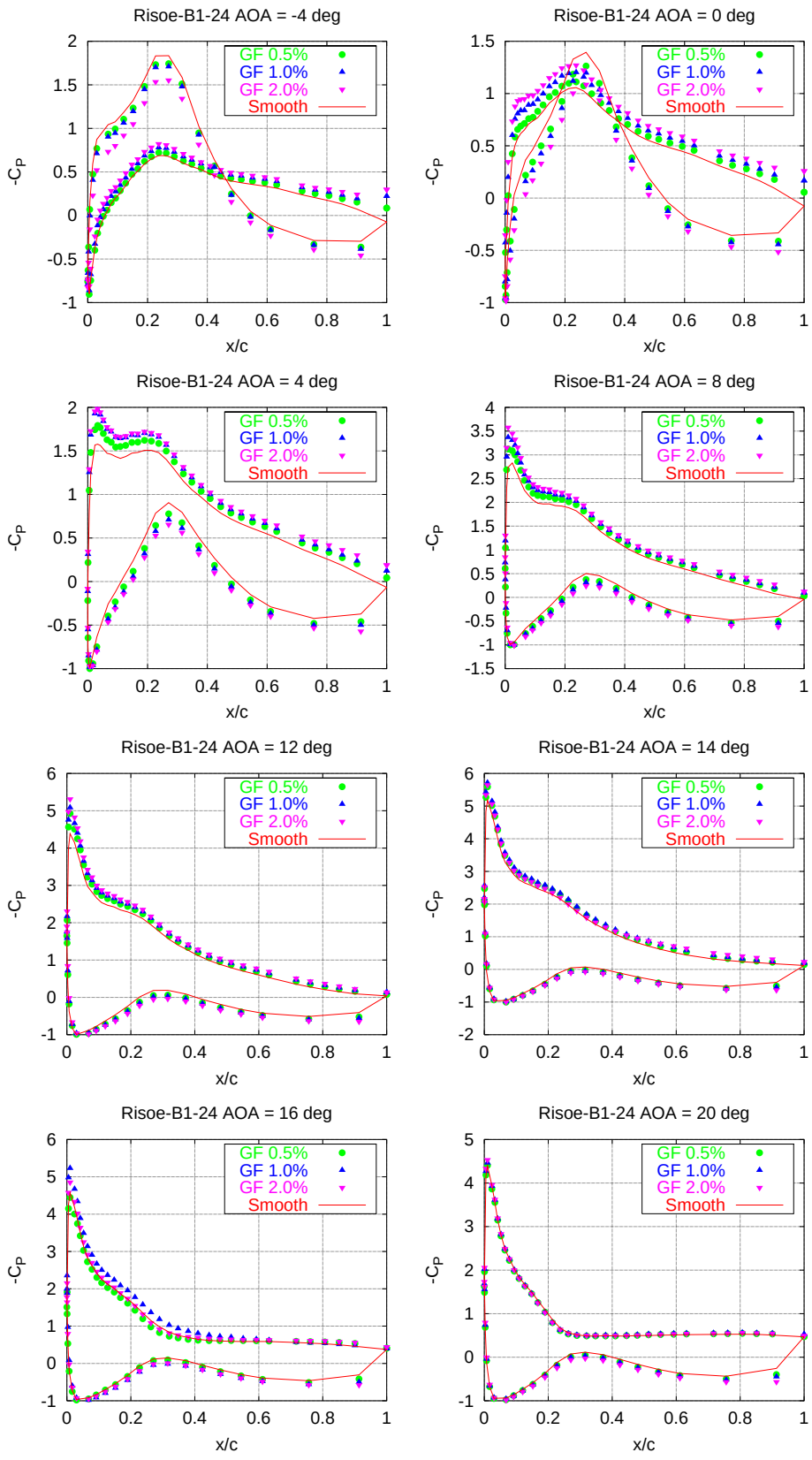

Figure 7-10 C_P at different angles of attack for Risø-B1-24 with Gurney flaps of different height (run 013, 018, 019) compared with smooth flow (run002).

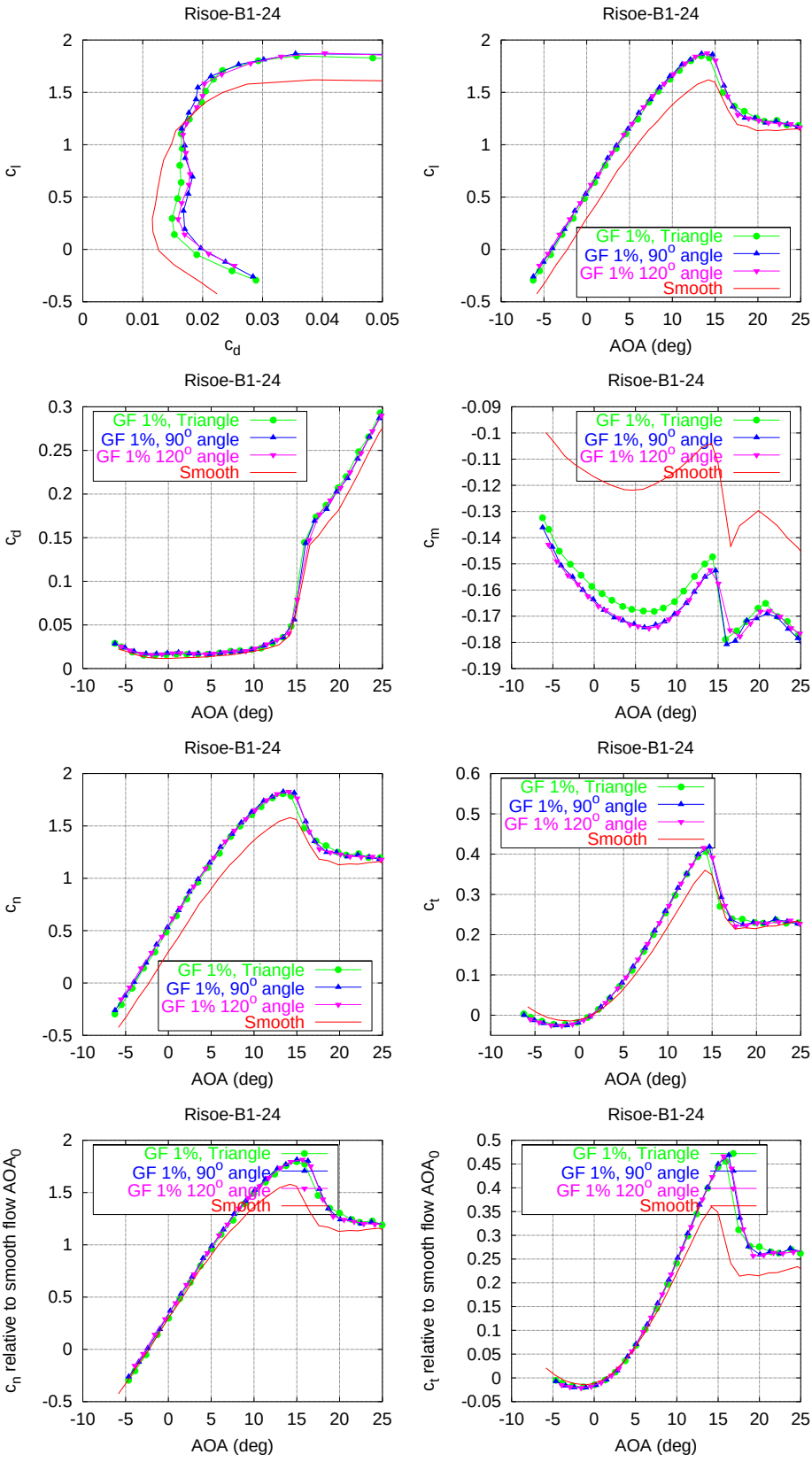

Figure 7-11 Risø-B1-24 with Gurney flaps of h/c = 0.01 with different shapes (run 013, 020, 021) compared with smooth flow (run002).

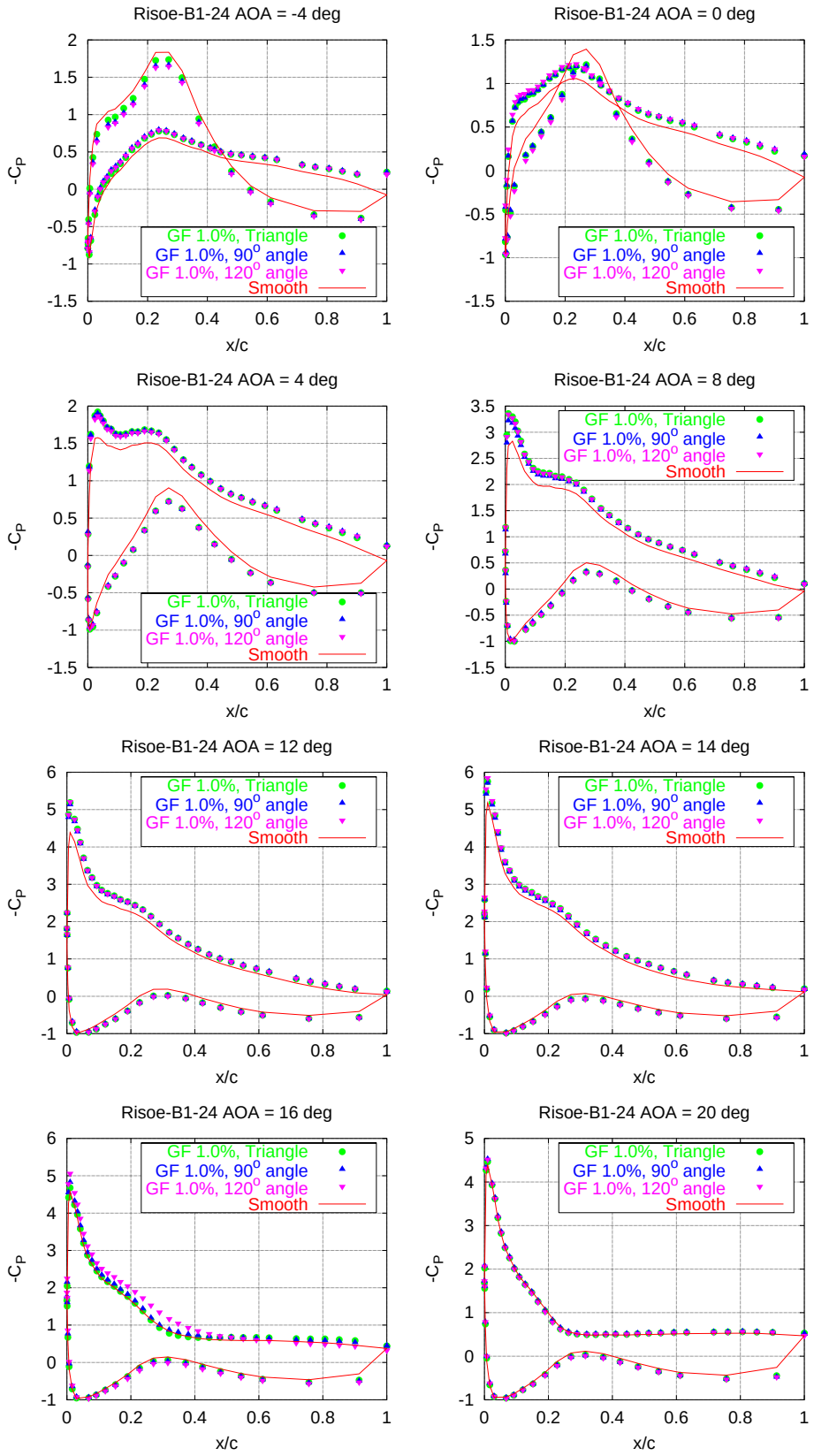

Figure 7-12 C_P at different angles of attack for Risø-B1-24 with Gurney flaps of h/c = 0.01 with different shapes (run 013, 020, 021) compared with smooth flow (run002).

7.6 Vortex generators, Gurney flaps (run 011, 014, 015)

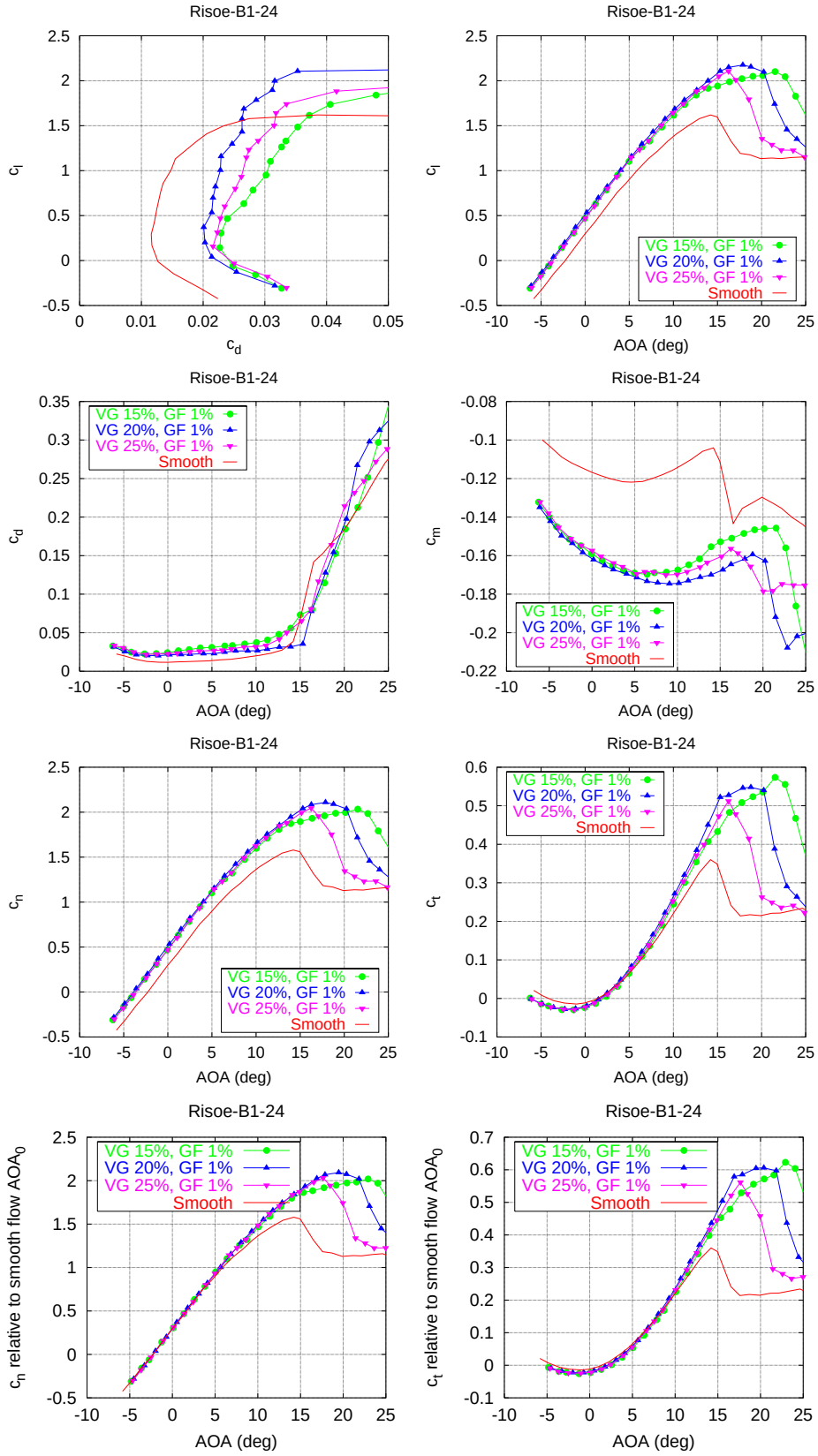

Figure 7-13 Risø-B1-24 with Gurney flaps, h/c = 0.01, vortex generators at different chord positions (run 011, 014, 015) compared with smooth flow (run002).

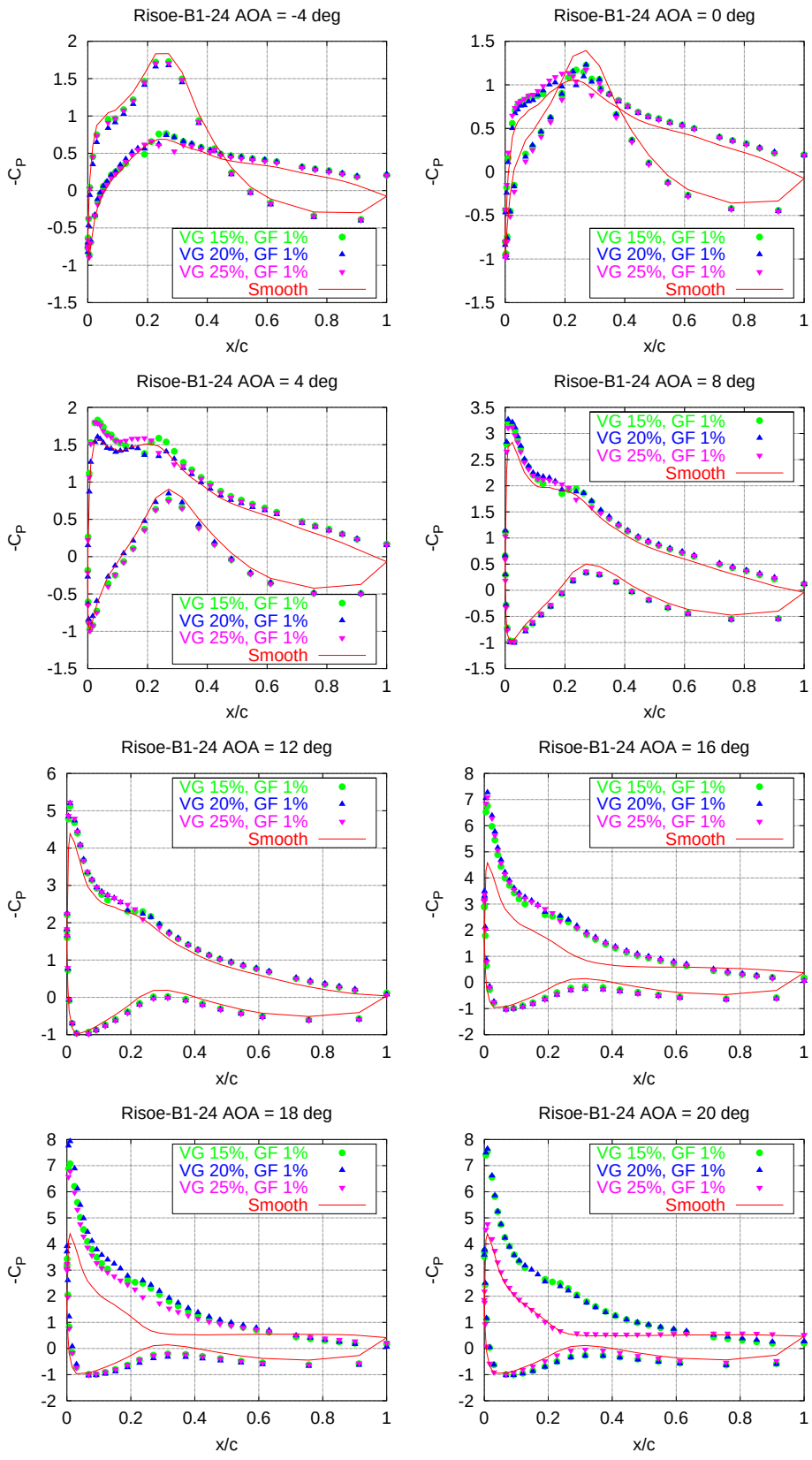

Figure 7-14 C_P at different angles of attack for Risø-B1-24 with Gurney flaps, h/c = 0.01, vortex generators at different chord positions (run 011, 014, 015) compared with smooth flow (run002).

7.7 Risø-B1-24, vortex generators, Gurney flaps, leading edge roughness (run 010, 011)

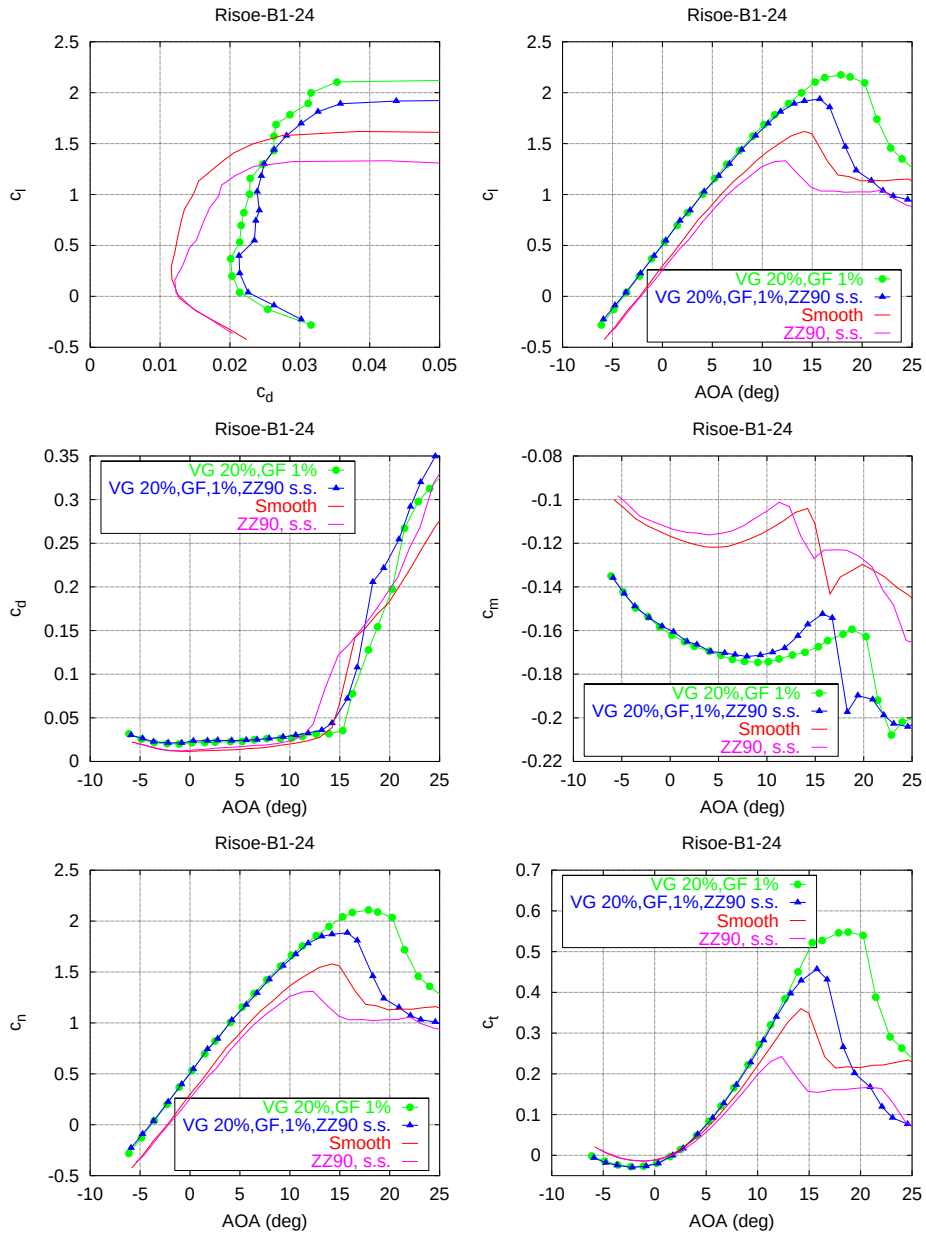

Figure 7-15 Risø-B1-24 with vortex generators, x/c = 0.20, Gurney flaps, h/c = 0.01 triangle, leading edge roughness ZZ90 s.s. (run 010, 011) compared with smooth flow (run002).

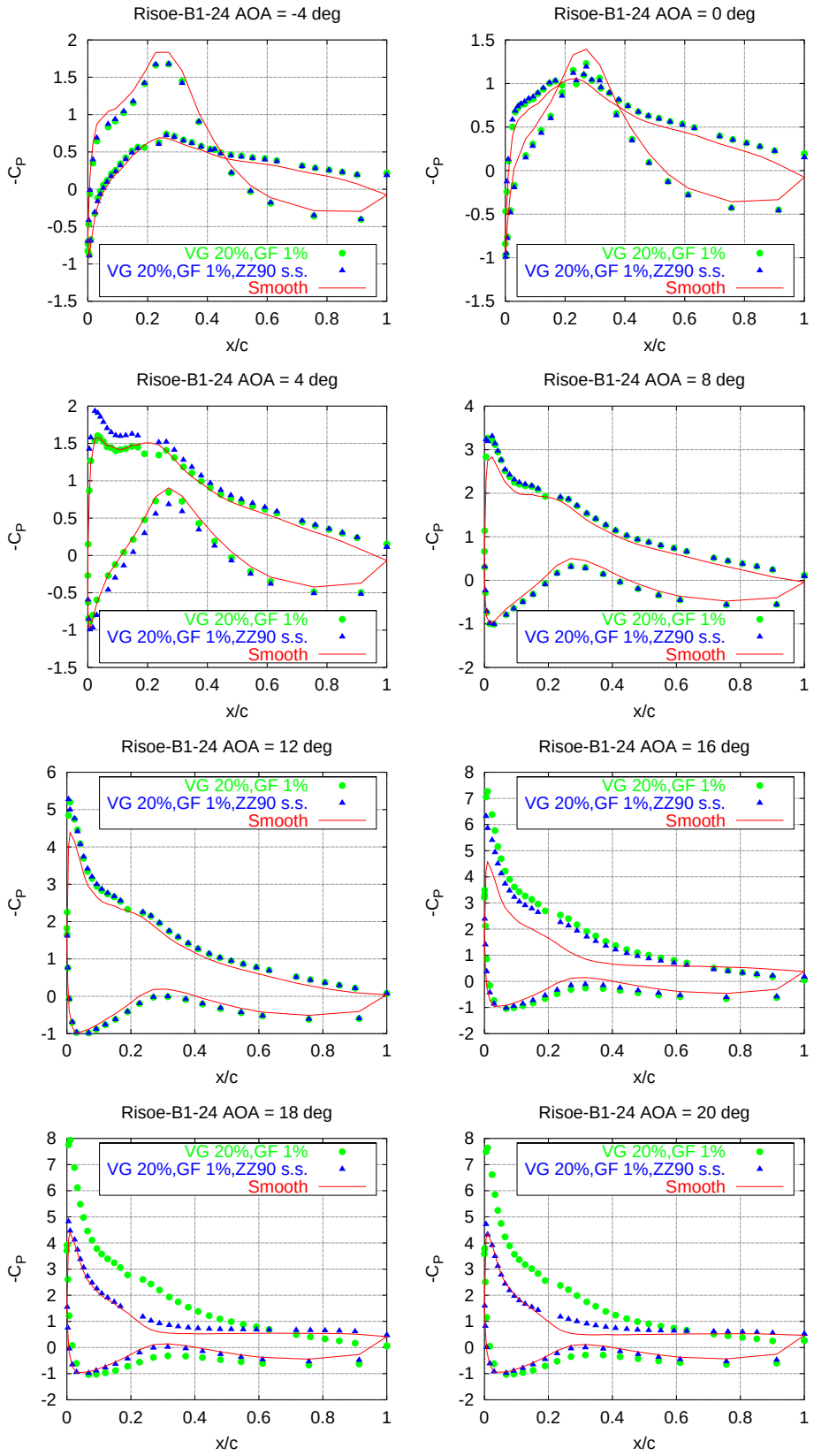

Figure 7-16 C_P at different angles of attack for Risø-B1-24 with vortex generators, x/c = 0.20, Gurney flaps, h/c = 0.01 triangle, leading edge roughness ZZ90 s.s. (run 010, 011) compared with smooth flow (run002).

7.8 Risø-B1-24, dynamic stall (run 005)

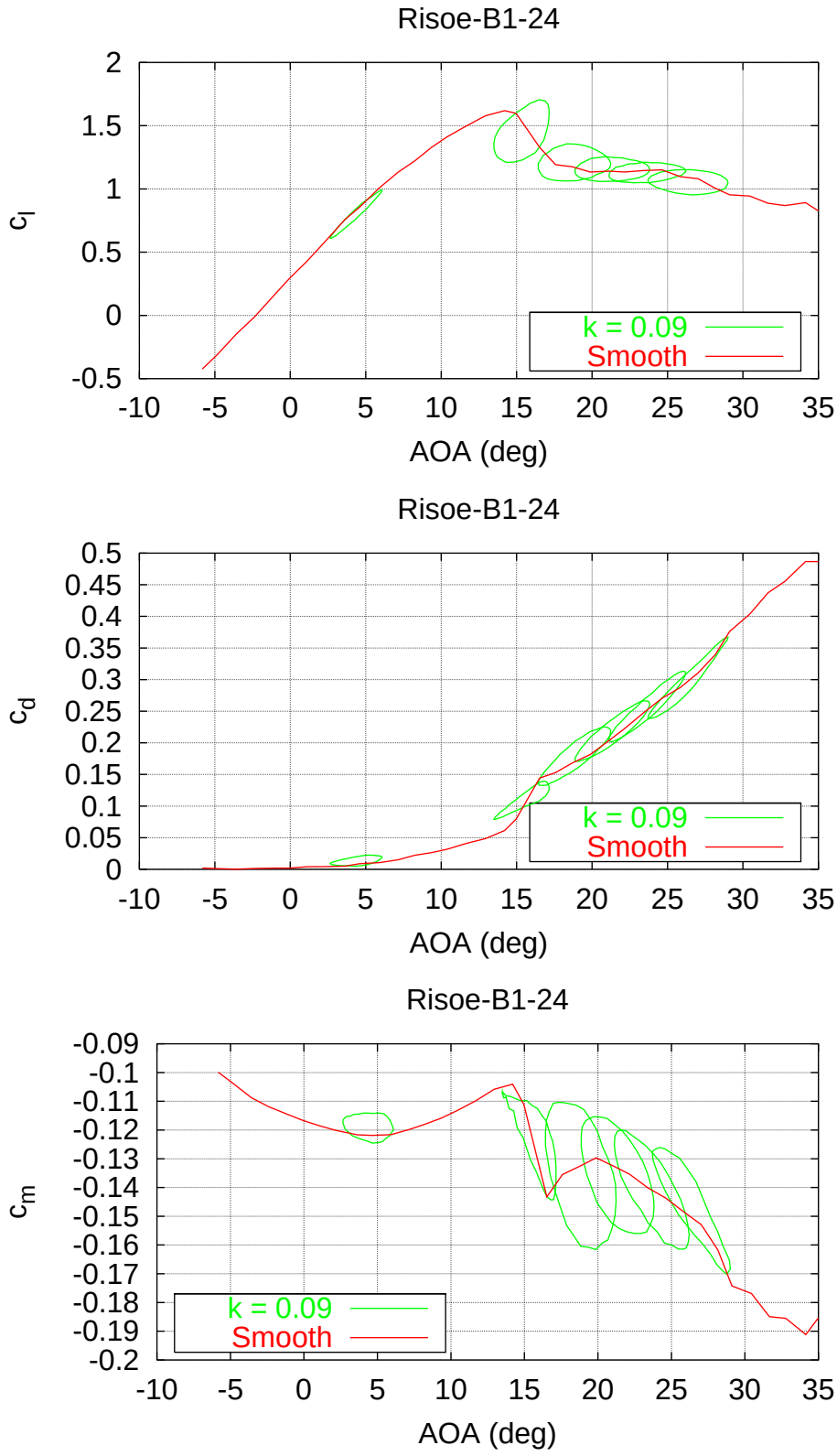

Figure 7-17 Risø-B1-24 c_l, c_d and c_m hysteresis loops for smooth flow, k = 0.092, A between 1.7° and 2.7° (run 005).

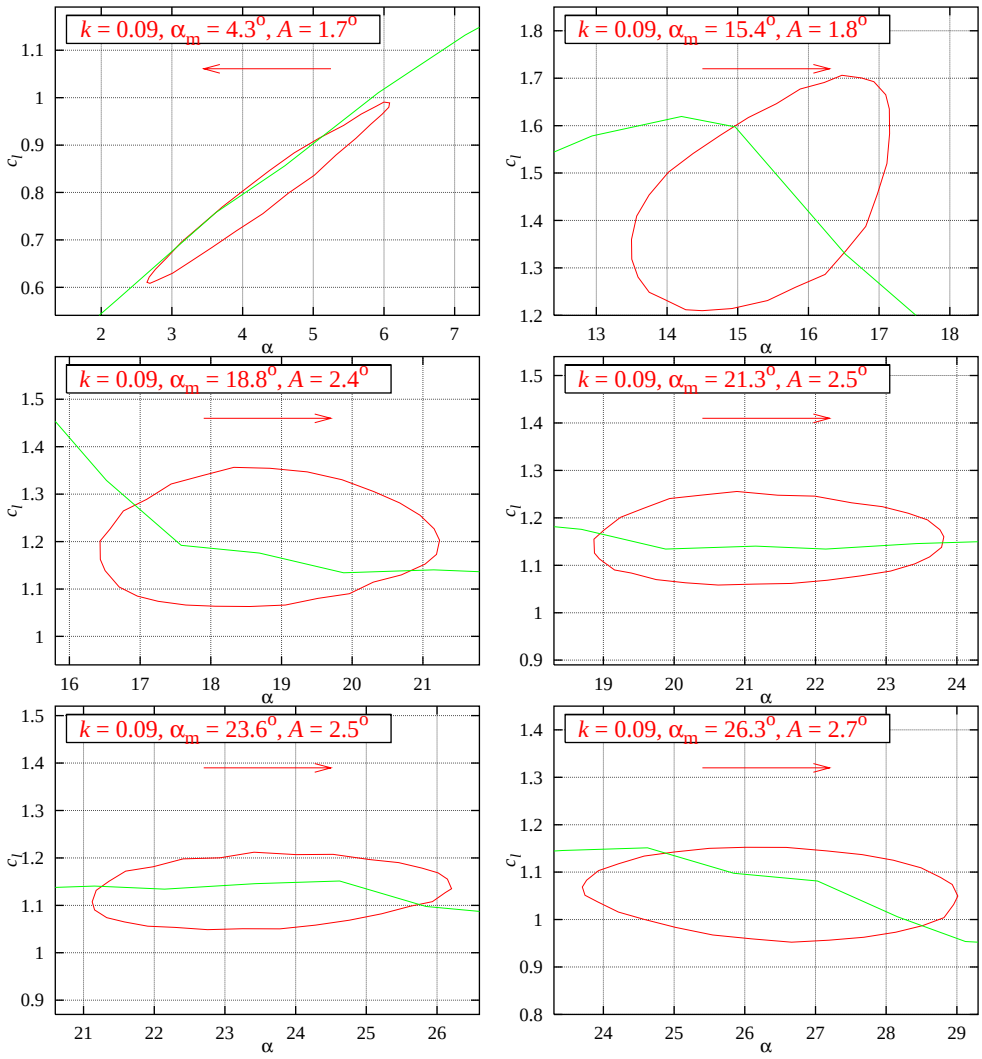

Figure 7-18 Risø-B1-24 c_l hysteresis loops for smooth flow at k = 0.09, A between 1.3° and 2.1° (run 005).

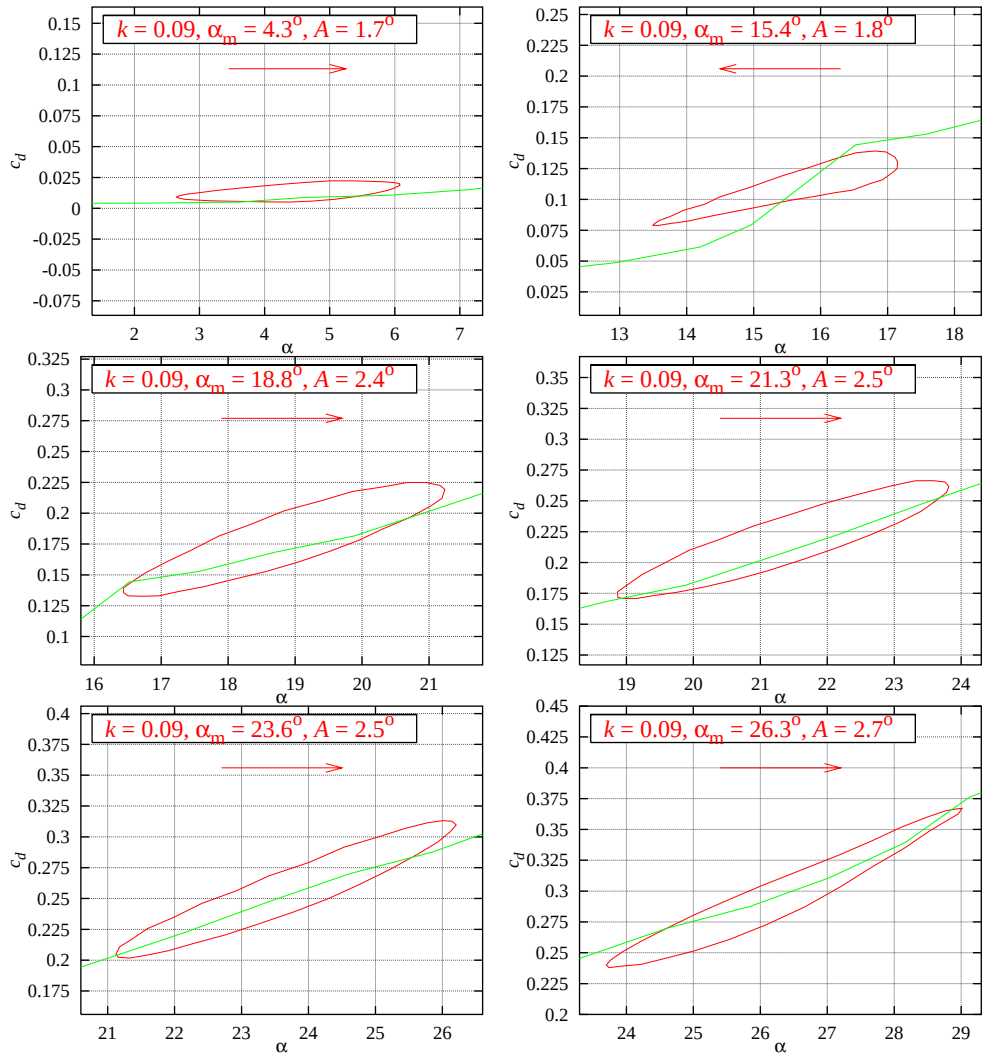

Figure 7-19 Risø-B1-24 c_d hysteresis loops for smooth flow at k = 0.09, A between 1.7° and 2.7° (run 005).

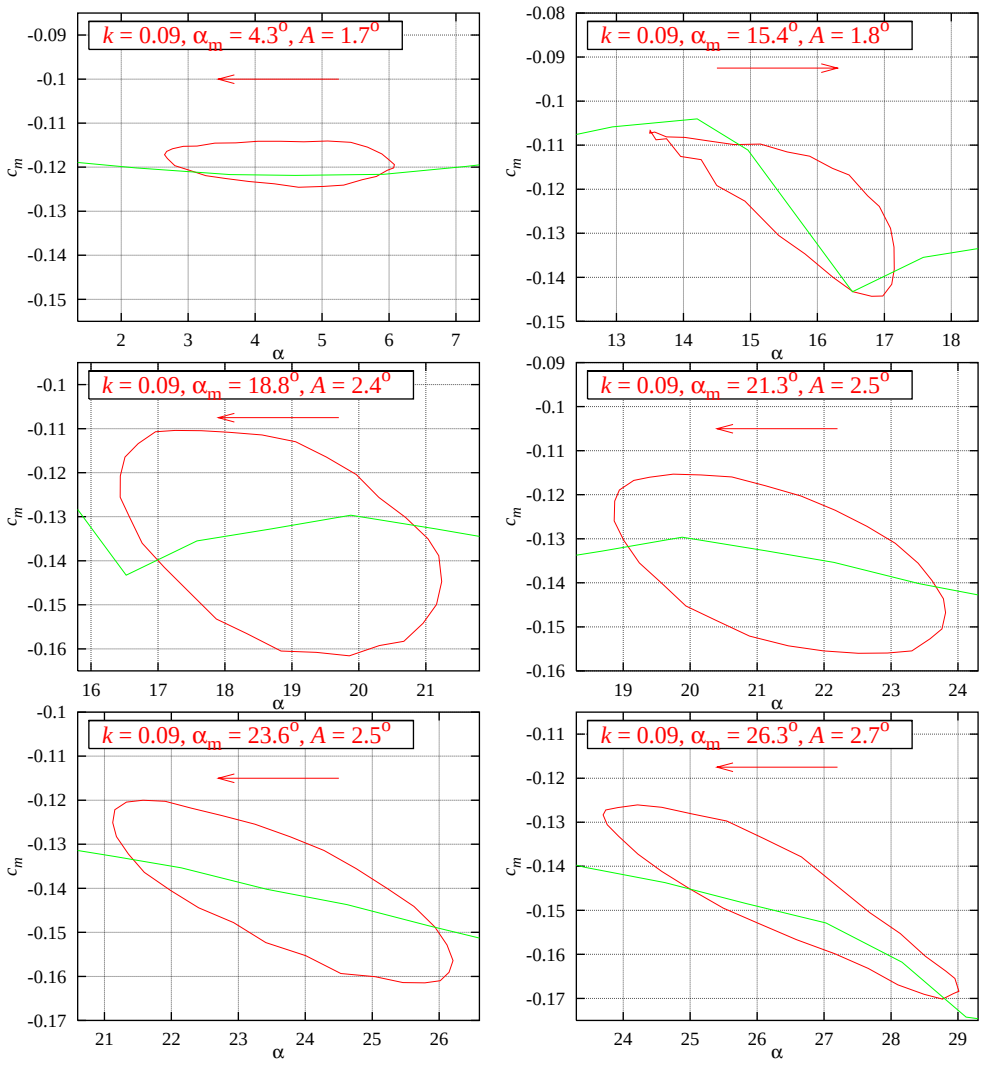

Figure 7-20 Risø-B1-24 c_m hysteresis loops for smooth flow at k = 0.09, A between 1.7° and 2.7° (run 005).

8 Sensitivity of airfoil characteristics

To determine the sensitivity of the airfoil characteristics with respect to the accuracy of the airfoil shape and the variation in Reynolds number, investigations were undertaken using EllipSys2D. The results are shown in Sections 8.1 and 8.2.

8.1 Theoretical and measured airfoil shape

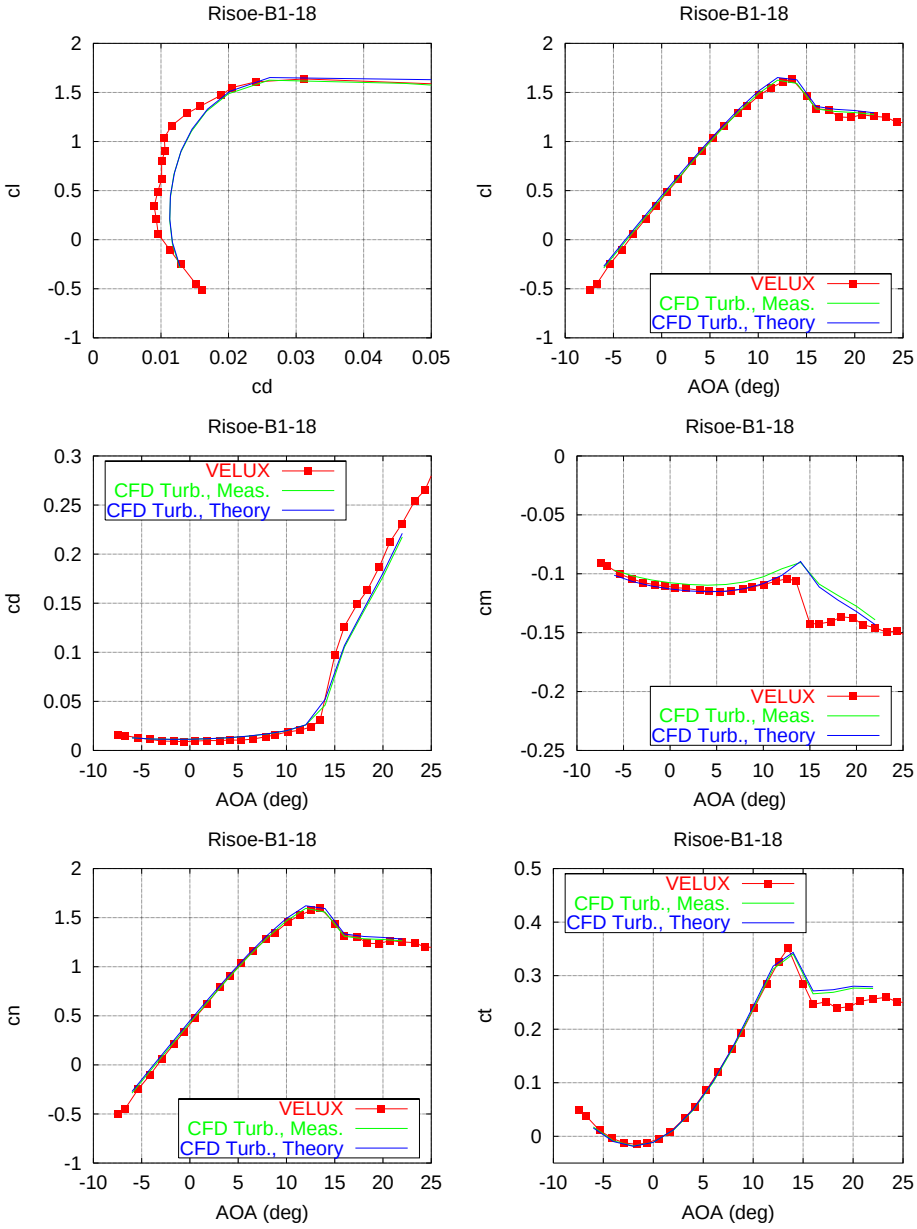

Figure 8-1 Comparison of airfoil characteristics for the measured and the theoretical Risø-B1-18 airfoil shape. The CFD computations were carried out using EllipSys2D assuming fully turbulent flow.

Figure 8-1 and Figure 8-2 show a comparison of airfoil characteristics for the actually measured and the theoretical Risø-B1-18 shape calculated with EllipSys2D with fully turbulent flow. For both airfoils it appeared that the difference in the predicted performance based on theoretical coordinates and actual measured coordinates was negligible. The only noticeable difference was a small offset of the moment coefficient curves whereas the remaining force coefficient curves were identical.

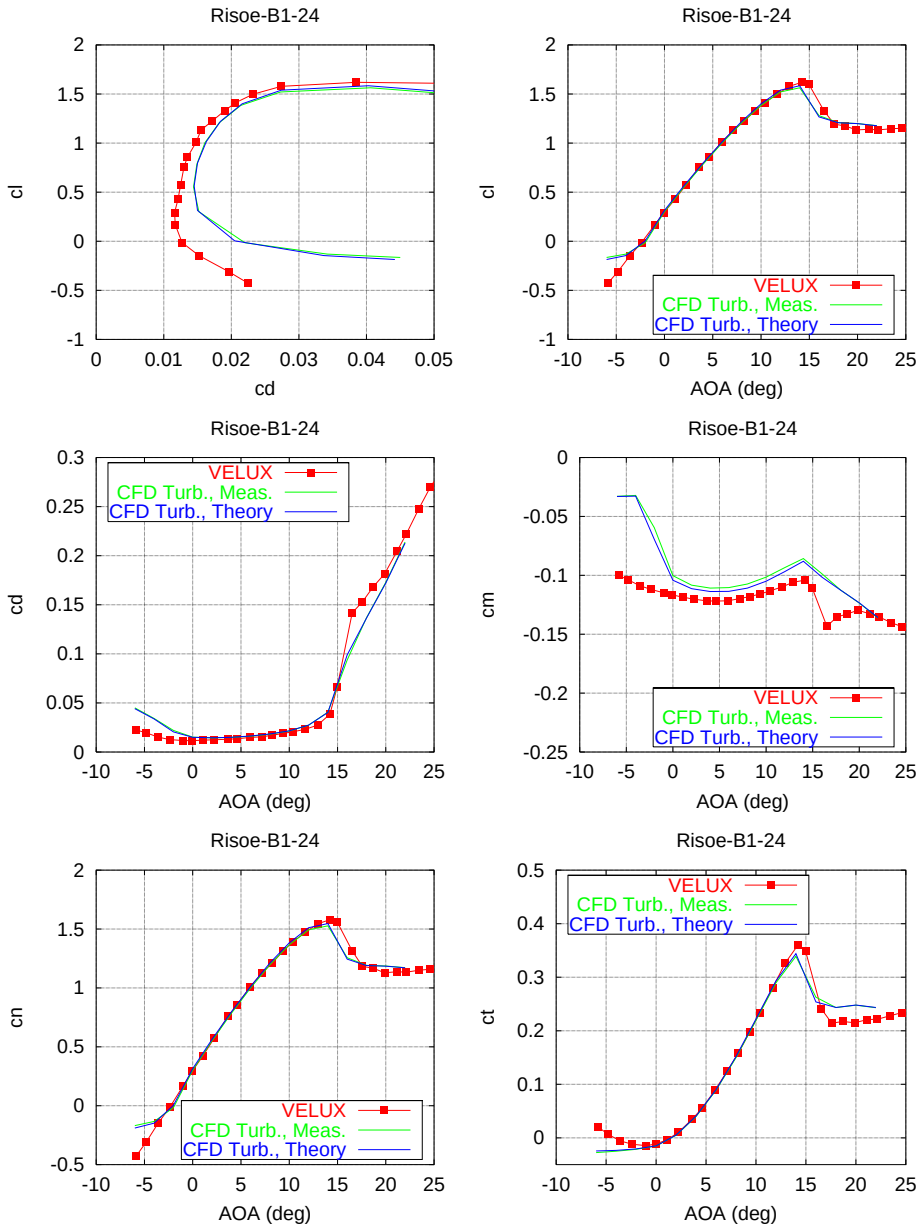

Figure 8-2 Comparison of airfoil characteristics for the measured and the theoretical Risø-B1-24 airfoil shape. The CFD computations were carried out using EllipSys2D assuming fully turbulent flow.

8.2 Variation in Reynolds number

The maximum Reynolds number for the VELUX wind tunnel is 1.6×10^6, which unfortunately is not representative for large wind turbines, which often have a Reynolds number of 6×10^6 on parts of the blades. Figure 8-3 and Figure 8-4 show a comparison of the measured airfoil characteristics with predictions at different Reynolds numbers for Risø-B1-18 and Risø-B1-24 respectively. The predictions were carried out using EllipSys2D with fully turbulent flow at Re = 1.6×10^6 and Re = 6×10^6.

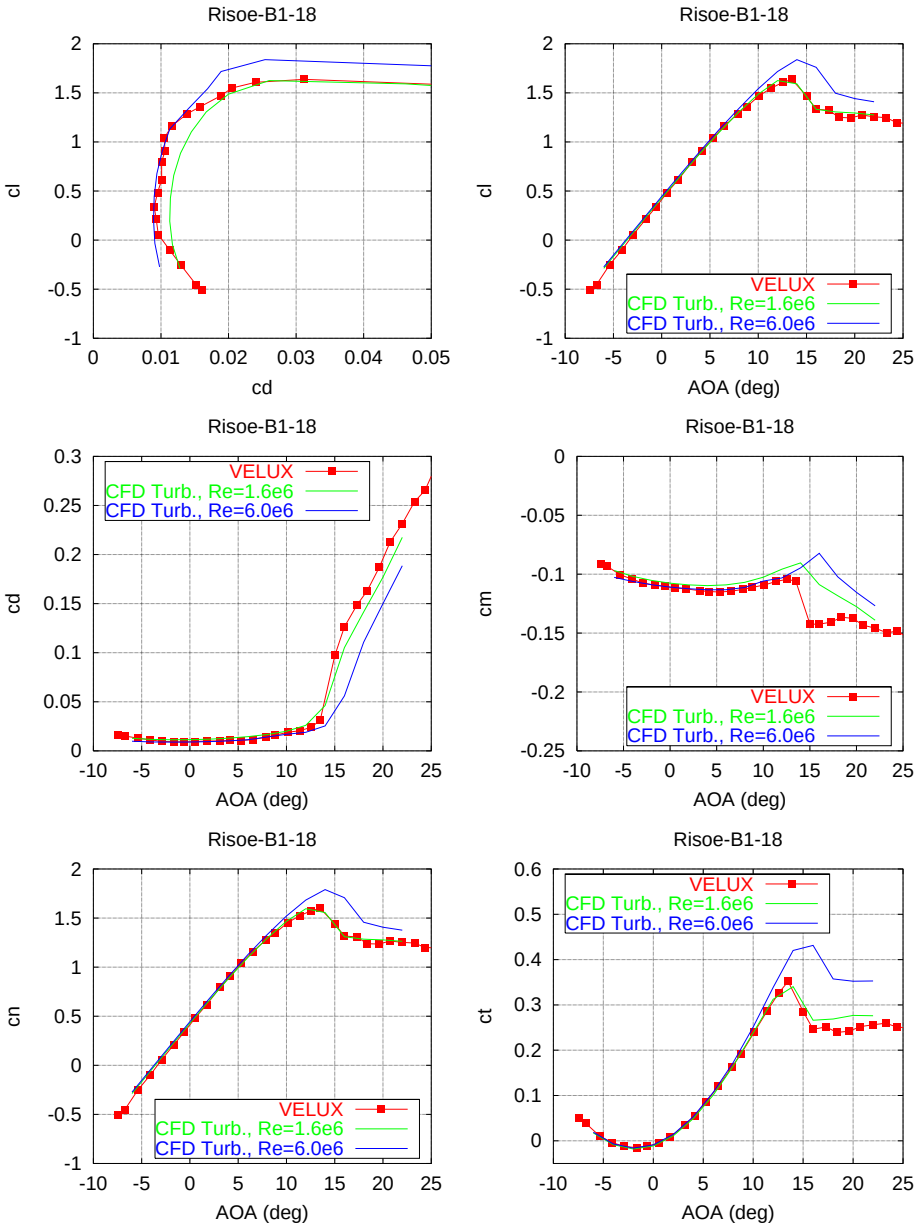

Figure 8-3 Comparison of airfoil characteristics for the measured Risø-B1-18 airfoil shape for two Reynolds numbers: Re=1.6×10^6 and 6.0x10^6. The CFD computations were carried out using EllipSys2D assuming fully turbulent flow.

For both Risø-B1-18 and Risø-B1-24 there was a clear trend in the change of both maximum lift and minimum drag with the Reynolds number. Increasing the Reynolds number to 6×10^6 from 1. 6×10^6 caused an increase in the maximum lift coefficient of 0.22 for Risø-B1-18 and 0.21 for Risø-B1-24 and a decrease in minimum drag of 0.0024 for Risø-B1-18 and 0.0033 for Risø-B1-24. When using the measurements in the input to wind turbine blade design, proper corrections have to be made on both lift and drag coefficients to ensure reliable predictions of aerodynamic performance.

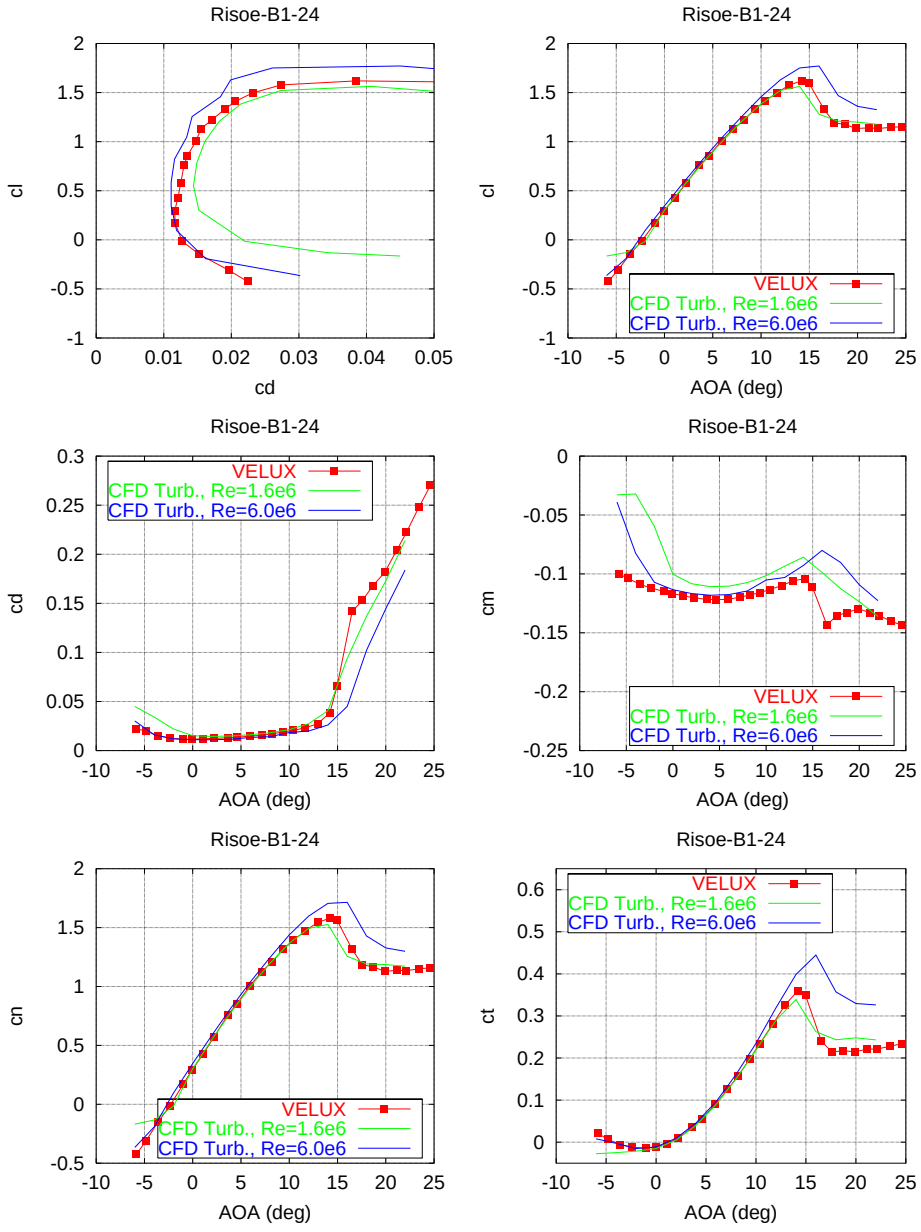

Figure 8-4 Comparison of airfoil characteristics for the measured Risø-B1-24 airfoil shape for two Reynolds numbers: Re=1.6×10^6 and 6.0x10^6. The CFD computations were carried out using EllipSys2D assuming fully turbulent flow.

9 Discussion

The quality of the measurements was in general very good. A few of the pressure transducers showed an unstable response and they had to be removed from the data analysis. A sufficient number of pressure transducers remained stable and reliable values could be obtained for the airfoil force coefficients. On the aft part of the pressure side a second order integration was used for the integration of the pressure distribution because of the coarse spacing between the remaining pressure transducers. The response of the wake rake yielding the drag coefficients at low angles of attack was in general stable

Numerical predictions were carried out for fully turbulent flow as well as for transitional flow using EllipSys2D as explained in Section 5.2. The major differences between the two different kinds of predictions were the magnitude of drag at attached flow and the magnitude of the maximum lift coefficient. As expected the predicted minimum drag coefficient for turbulent flow was significantly higher than the minimum drag for transitional flow. Also the maximum lift coefficient for transitional flow was larger than for turbulent flow.

9.1 Risø-B1-18

Measurements of Risø-B1-18 are shown in Chapter 6, and main results are shown in Table 9-1.

Table 9-1 Risø-B1-18 $c_{l,max}$, $c_{d,min}$ and c_{mo}.

Surface condition		**Run**	$c_{l,max}$	$c_{d,min}$	c_{mo}
Smooth		024	1.64	0.0090	-0.17
Leading edge roughness	ZZ90^o 5%/10%	030	1.58	0.013	-0.17
	ZZ90^o s.s.	031	1.39	0.011	-0.18
	ZZ90^o p.s.	032	1.45	0.011	-0.17
	ZZ60^o s.s.	033	1.20	0.010	-0.18
	Trip Tape 1	025	1.62	0.0092	-0.18
	Trip Tape 2	026	1.62	0.0092	-0.18
Stall strips	SS 0%	034	1.23	0.0098	-0.17
	SS 1%	035	1.26	0.0097	-0.14
	SS 2%	036	1.43	0.011	-0.16
	SS 3%	038	1.57	0.012	-0.16

The measured results with smooth flow show a maximum lift coefficient of 1.64 at an angle of attack of approximately 13^o and a minimum drag coefficient of 0.0090 at an angle of attack of approximately -1^o, Section 6.1. Drag coefficients in the angle of attack range, [0^o:5^o] were slightly irregular. The rise in drag began around an angle of attack of 5^o. However, separation from the trailing edge did not occur until angles of attack around 12^o. In the post stall area the lift coefficient was 1.25 at angles of attack around 20^o.

The measurements were in very good agreement with the numerical predictions. The turbulent predictions captured very well the shape of the lift coefficient versus angle of attack curve from low angles of attack until stall including the magnitude of the maximum lift coefficient. Also the post stall region was well captured. The measured magnitude of drag at attached flow fell between the predictions for transitional and turbulent flow. This has always been the case for measurements in the VELUX wind tunnel [3] because the transitional prediction assumes a hydraulically smooth surface and neglects background turbulence in the on-coming flow. On the other hand the turbulent prediction involves too high skin friction from the turbulent boundary layer on the entire airfoil. The comparison of predicted and measured pressure distributions showed excellent agreement for the entire angle of attack range from -4^o until 20^o. At angles of attack above 14^o the turbulent prediction matched the measurements better than the transitional prediction.

Measurements with leading edge roughness (LER) were shown in Section 6.2. The different kinds of roughness were explained in Section 4.2. Overall the different kinds of roughness were divided into severe roughness and light roughness. Severe roughness included measurements with 0.35 mm thick zigzag tape of 90^0 at the very leading edge suction side (ZZ90 s.s.) and pressure side (ZZ90 p.s.) together with zigzag tape simultaneously on the suction side at 5% chord and on the pressure side at 10% chord (zz90, 5%/10%). Furthermore measurements were carried out with 0.85 mm 60^o zigzag tape at the leading edge suction side. Light roughness included 0.12 mm trip tape at the very leading edge (TT 1) and two times 0.12 mm trip tape (TT 2).

All measurements with leading edge roughness showed that the airfoil was not very sensitive to leading edge roughness. We found an expected increase in drag at low angles of attack whereas the loss in maximum lift varied for the different kinds of roughness. Maximum lift was only marginally sensitive to light roughness and to the ZZ90, 5%/10% configuration whereas a drop in maximum lift coefficient was measured for the more severe cases with zigzag tape on the leading edge part of the suction side, ZZ60 and ZZ90. The most severe roughness, ZZ60 resulted in a drop in maximum lift coefficient of 0.44. The less severe ZZ90 case involved a drop in maximum lift of 0.25. This case is believed to be more representative than ZZ60 [12].

Section 6.3 shows measurements with stall strips on different locations of the leading edge pressure side. The stall strips were located at the very leading edge (SS 0%) and at different locations on the pressure side of the leading edge (SS 1%, 2% and 3%), section 4.3

The maximum lift was not sensitive to stall strips further downstream than 3% chord on the pressure side, but moving the stall strips towards the leading edge gradually reduced the magnitude of the maximum lift coefficient. Stall strips at the very leading edge resulted in a drop in maximum lift coefficient of 0.4. At the same time minimum drag increased when stall strips were moved towards the leading edge. Moving stall strips towards the leading edge also reduced the drag rise angle of attack because of separation on the suction side. Even though the airfoil was not intended for use with stall strips, the measurements showed that stall strips were feasible.

Dynamic stall measurements were shown in Section 6.4 with the airfoil in a harmonic pitch variation with amplitude between 1.7^o and 2.6^o around different mean angles of attack. The reduced frequency was 0.09 as explained in Section 5.1. As expected the dynamic loops were different for attached and separated flows. For attached flow, the direction of the lift coefficient loops was counter clockwise whereas the direction changed to clockwise at and beyond the maximum lift coefficient. The slope of the loops during stall was horizontal even though the slope of the mean curve was

negative. For the drag coefficient all loops were clockwise and the slope of the loops in general followed the slope of the mean curve. The opening of the drag coefficient loops was limited. For the moment coefficient, the loops were in general open and the direction of all loops was counter clockwise.

9.2 Risø-B1-24

Measurements of Risø-B1-24 are shown in Chapter 7 and the main results are shown in Table 9-2.

Table 9-2 Risø-B1-24 $c_{l,ma}$, $c_{d,min}$ and c_{mo}.

Surface condition		**Run**	$c_{l,max}$	$c_{d,min}$	c_{mo}
Smooth		002	1.62	0.012	-0.11
Leading edge roughness	ZZ90° 5%/10%	006	1.50	0.019	-0.11
	ZZ90° s.s.	008	1.33	0.012	-0.11
	ZZ60° s.s.	007	1.17	0.013	-0.11
Vortex generators	VG 15%	017	1.95	0.017	-0.11
	VG 20%	012	2.02	0.015	-0.11
	VG 30%	016	1.95	0.013	-0.11
Vortex generators Leading edge roughness	VG 20% ZZ90° s.s.	009	1.75	0.015	-0.11
Gurney flaps	Triangular height 0.5%	018	1.75	0.014	-0.14
	Triangular height 1.0%	013	1.85	0.015	-0.15
	Triangular height 2.0%	019	1.94	0.019	-0.16
	90° angle height 1.0%	020	1.87	0.016	-0.15
	120° angle height 1.0%	021	1.87	0.017	-0.15
Vortex generators Gurney flaps	VG 15% GF 1%	014	2.10	0.023	-0.15
	VG 20% GF 1%	011	2.17	0.020	-0.15
	VG 25% GF 1%	015	2.11	0.022	-0.15
Vortex generators gurney flaps Leading edge roughness	VG 20% GF 1% ZZ90° s.s.	010	1.94	0.021	-0.15

The measurements with a smooth surface in Section 7.1 showed a maximum lift coefficient of 1.62 at an angle of attack of approximately 14° and a minimum drag of 0.012 at an angle of attack of –1°. The shapes of both lift and drag curves versus angle of attack were smooth. The rise in drag began around 5° and separation from the trailing edge occurred at around 12°. The lift coefficient was around 1.1 in the post stall area.

The measurements were in excellent agreement with the numerical prediction with turbulent flow. Predictions with transitional flow were not carried out because the

modelling of transition is not trusted for airfoils with high relative thickness. The turbulent prediction captured very well the shapes of both lift and drag versus angle of attack from low angles of attack over maximum lift coefficient and into deep stall. However, the magnitude of drag at low angles of attack was slightly higher in the prediction because of the too high skin friction of the turbulent boundary layer. At very low angles of attack, the prediction showed separation on the pressure side, which lead to a significant difference in the lift coefficient compared to the linear lift curve slope of the measurement. This shows that the assumption of turbulent flow on the pressure side in the prediction was not realistic.

Section 7.2 shows measurements with leading edge roughness. The kinds of roughness, which were tested, were ZZ90 5%/10%, ZZ90 and ZZ 60 at the leading edge suction side as explained in Section 4.2. All kinds were characterised as severe. The measurements showed that the airfoil despite its high relative thickness and its high maximum lift coefficient was not very sensitive to leading edge roughness. The drop in maximum lift coefficient was 0.45 for the most severe configuration, ZZ60 and 0.29 for the less severe ZZ90 configuration whereas the drop in maximum lift was only 0.12 for the ZZ90 5%/10% configuration.

Measurements with Delta wing shaped vortex generators with a maximum height of 1% chord were shown in Section 7.3. The shapes and dimensions of the vortex generators were explained in Section 4.4. The vortex generators were located at different chord positions from 15% of the chord (VG 15%) until 30% of the chord (VG 30%).

As it could be expected, all measurements with vortex generators showed an increase in the maximum lift coefficient and at the same time an increase in the minimum drag coefficient. The angle of attack when separation occurred was increased by the presence of the vortex generators and this lead to relatively high lift to drag ratios at angles of attack in the range from 8^o until 13^o. On basis of the measurements with vortex generators at different locations it could be concluded that the optimum configuration was at 20% chord (VG 20%). Here, the maximum lift coefficient was increased by 0.40 to 2.02 compared to smooth flow. At the same time the increase in drag was limited. Moving the vortex generators forward partially destroyed the linear lift curve at angles of attack above 10^o and also increased drag significantly. On the other hand moving the vortex generators backward reduced the gain in maximum lift coefficient.

Section 7.4 shows measurements with vortex generators at 20% chord with leading edge roughness (ZZ90). The presence of leading edge roughness caused a drop in the maximum lift coefficient of 0.27. The drop in maximum lift coefficient from roughness without vortex generators was 0.29 with similar roughness. Roughness also increased drag so that the ratio of lift to drag was significantly reduced at higher angles of attack.

Measurements were carried out with different types of Gurney flaps as explained in Section 4.5. Triangular shaped Gurney flaps of different height from 0.5% of the chord (GF 0.5%) until 2% of the chord (GF 2%) were tested and Gurney flaps of height 1% with different shapes were tested.

Measurements with triangular Gurney flaps of different height showed that increasing the Gurney flap height increased the maximum lift coefficient. At the same time the angle of attack for zero lift was reduced, minimum drag was increased and the moment coefficient was reduced. It appeared from the measurements that the optimum height was 1% of the chord since this resulted in an increase in the maximum lift

coefficient of 0.23 to 1.85 whereas the ratio of lift to drag at angles of attack above 2^o was not reduced. For larger Gurney flaps the lift to drag ratio was reduced for angle of attack until 5^o.

Measurements with Gurney flaps of the same height but with different shapes showed an insignificant difference in the maximum lift coefficient and only a slight increase in drag for some of the configurations.

Section 7.6 shows measurements with a combination of vortex generators at various chord positions and triangular Gurney flaps of height 1%. The measurements show that a combination of 1% high triangular Gurney flaps and Delta wing vortex generators of height 1% chord at 20% chord position result in an increase in maximum lift coefficient of 0.55 to 2.17. At the same time the reduction in the maximum lift to drag ratio is minimum compared to the other tested configurations. It appeared from the measurements that the combination of vortex generators and Gurney flaps may provide a possible significant increase in maximum lift, which may be used to reduce the solidity and possibly increase the relative thickness of the inboard part of a wind turbine blade. The measurements of vortex generators, Gurney flaps and leading edge roughness in Section 7.7 show that leading edge roughness causes a drop in maximum lift coefficient of 0.23, which is less than the corresponding reduction value of 0.29 for the configuration without vortex generators and Gurney flaps.

Dynamic stall measurements were shown in Section 7.8 with the airfoil in a harmonic pitch variation with amplitude between 1.7^o and 2.7^o around different mean angles of attack mostly in the stalled region. The reduced frequency was 0.09 as explained in Section 5.1. For the lift coefficient, the direction of the loops was counter-clockwise for attached flow and clockwise for separated flow. The slope of the loops during stall followed the steady curve except for the loop with a mean angle of 15.4^o, where there was a positive slope of the loop compared to the negative slope of the steady curve.

For the drag coefficient the loop around 15.4^o was counter-clockwise whereas the remaining loops were clockwise. In general, the slope of the loops followed the slope of the mean curve and the opening of the loops was limited. For the moment coefficient, the loops were in general open and the direction of most loops was counter-clockwise.

9.3 Airfoil comparison

Table 9-3 shows a comparison of Risø-B1-18 and Risø-B1-24. The two airfoils were not designed to meet the same design objectives and the test matrix did only contain a limited number of identical measurements, which were smooth surface and various kinds of leading edge roughness.

The two airfoils had nearly the same value of the maximum lift coefficient with a difference of only 0.02 in favour of Risø-B1-18. However, the minimum drag coefficient was 0.003 higher for Risø-B1-24 compared with Risø-B1-18 mainly because of the higher relative thickness.

Table 9-3 Risø-B1-18 and Risø-B1-24 $c_{l,max}$ and $c_{d,min}$.

Surface condition		**Risø-B1-18**		**Risø-B1-24**	
		$c_{l,max}$	$c_{d,min}$	$c_{l,max}$	$c_{d,min}$
Smooth		1.64	0.0090	1.62	0.012
Leading edge roughness	ZZ90° 5%/10%	1.58	0.013	1.50	0.019
	ZZ90° s.s.	1.39	0.011	1.33	0.012
	ZZ60° s.s.	1.20	0.010	1.17	0.013

With leading edge roughness the drop in maximum lift coefficient was for all measurements slightly higher for Risø-B1-24 compared with Risø-B1-18, which can be explained by the higher relative thickness. However the difference between the two airfoils was only between 0.03 and 0.06 for the various measurements with the smallest difference for the most severe roughness:

- For the ZZ90 5%/10% case the drop was 0.12 for Risø-B1-24 compared with 0.06 for Risø-B1-18 which gave a difference of 0.06.
- For the ZZ90 at the leading edge suction side case the drop was 0.29 for Risø-B1-24 compared with 0.24 for Risø-B1-18, which gave a difference of 0.05.
- For the ZZ60 at the leading edge suction side case the drop was 0.45 for Risø-B1-24 compared with 0.42 for Risø-B1-18, which gave a difference of 0.03.

9.4 Sensitivity of airfoil characteristics

The actual airfoil shapes were measured and compared with the theoretical shapes to clarify possible deviations in the shapes, Section 4.1. Deviations could lead to discrepancies in the measured performance compared with the theoretical performance. Section 8.1 shows a comparison of measurements with EllipSys2D predictions on both the theoretical coordinates and the actual measured coordinates. For both airfoils it appeared that the difference in the predicted performance based on theoretical coordinates and actual measured coordinates was negligible. The only noticeable difference was a small offset of the moment coefficient curves. The remaining force coefficient curves were identical.

9.5 Variation with Reynolds number

Table 9-4 shows the variation of the airfoil main characteristics with Reynolds number. The maximum Reynolds number for the VELUX wind tunnel is 1.6×10^6, which unfortunately is not representative for large wind turbines, which often have a Reynolds number of 6×10^6 on parts of the blades. The design Reynolds number for Risø-B1-18 and Risø-B1-24 was 6×10^6.

Table 9-4 Predicted variation in Risø-B1-18 and Risø-B1-24 $c_{l,max}$ and $c_{d,min}$ with Reynolds number compared with measurement.

	Reynolds number x 10^6	**Risø-B1-18**		**Risø-B1-24**	
		$c_{l,max}$	$c_{d,min}$	$c_{l,max}$	$c_{d,min}$
Smooth measurement	1.6	1.64	0.0090	1.62	0.012
EllipSys2D prediction	1.6	1.62	0.0113	1.56	0.0144
EllipSys2D prediction	6.0	1.84	0.0089	1.77	0.0111

For both Risø-B1-18 and Risø-B1-24 there was a clear trend in the change of both maximum lift and minimum drag with the Reynolds number. Increasing the Reynolds number to 6×10^6 from 1. 6×10^6 caused an increase in the maximum lift coefficient of 0.22 for Risø-B1-18 and 0.21 for Risø-B1-24 and a decrease in minimum drag of 0.0024 for Risø-B1-18 and 0.0033 for Risø-B1-24. When using the measurements in the input to wind turbine blade design, proper corrections have to be made on both lift and drag coefficients to ensure reliable predictions of aerodynamic performance.

10 Conclusions

This report describes 2D measurements on the Risø-B1-18 and Risø-B1-24 airfoils carried out in the *VELUX* wind tunnel at a Reynolds number of 1.6×10^6. The aerodynamic properties were derived from pressure measurements on the airfoil surface and in the wake. The measurements comprised both static and dynamic inflow and the test matrix involved smooth surface, various configurations of leading edge roughness, stall strips, vortex generators and Gurney flaps.

The airfoils were specifically developed for megawatt sized wind turbine rotors with pitch regulation and variable speed (PRVS) with a high maximum lift coefficient to allow for higher energy capture and at the same time low solidity. The design Reynolds number was $6.0\text{x}10^6$.

The quality of the measurements was very good and the agreement between the measurements and numerical CFD predictions with EllipSys2D was good. For both airfoils predictions with turbulent flow captured very well the shapes of lift and drag curves as well as the magnitude of maximum lift.

The following conclusions could be drawn for the Risø-B1-18 airfoil:

- The maximum lift coefficient was 1.64 at an angle of attack of approximately 13^o.
- Measurements with leading edge roughness showed that the airfoil was not very sensitive to leading edge roughness despite its high maximum lift.
- Standard zigzag tape of 90^o at 5% chord on the suction side and 10% chord on the pressure side reduced the maximum lift coefficient by 0.06.
- Zigzag tape of 90^o at the very leading edge of the suction side caused a drop in maximum lift coefficient of 0.25.
- Measurements with stall strips showed that stall strips could control the level of maximum lift.
- Stall strips at the very leading edge of the pressure side reduced the maximum lift coefficient by 0.4
- Dynamic inflow measurements from pitch motion showed expected results for hysteresis curves of lift, drag and moment coefficients. The slopes of the loops in general followed the slopes of the mean curves.

The following conclusions could be drawn for the Risø-B1-24 airfoil:

- The maximum lift coefficient was 1.62 at an angle of attack of approximately 14^o.
- Measurements with leading edge roughness showed that the airfoil was only little sensitive to leading edge roughness despite its high relative thickness and high maximum lift.
- Standard zigzag tape of 90^o at 5% chord on the suction side and 10% chord on the pressure side reduced the maximum lift coefficient by 0.12 to 1.50.
- Zigzag tape of 90^o at the very leading edge of the suction side caused a drop in maximum lift coefficient of 0.29.
- Measurements with Delta wing shaped vortex generators of height 1% chord located at 20% chord increased the maximum lift coefficient by 0.40 to 2.02.
- Measurements with triangular shaped Gurney flaps of height 1% increased the maximum lift coefficient by 0.23 to 1.85.

- Measurements with Gurney flaps of the same height with different shapes showed insignificant differences in maximum lift and minimum drag.
- Measurements with a combination of vortex generators and Gurney flaps showed a maximum increase in the maximum lift coefficient of 0.55 to 2.17.
- Dynamic inflow measurements from pitch motion showed expected results for hysteresis curves of lift, drag and moment coefficients. The slopes of the loops in general followed the slopes of the mean curves.

The two airfoils were not designed to meet the same design objectives and the test matrix did only contain a limited number of identical measurements, which were smooth surface flow and various kinds of leading edge roughness. The two airfoils had nearly the same value of the maximum lift coefficient with a difference of only 0.02 in favour of Risø-B1-18. The minimum drag coefficient was 0.003 higher for Risø-B1-24 compared with Risø-B1-18 mainly because of the higher relative thickness. With leading edge roughness the drop in maximum lift coefficient was for all measurements slightly higher for Risø-B1-24 compared with Risø-B1-18.

The maximum Reynolds number for the VELUX wind tunnel is 1.6×10^6, which unfortunately is somewhat lower than the design Reynolds number of 6×10^6. For both Risø-B1-18 and Risø-B1-24 numerical predictions showed that there was a clear increase in the maximum lift coefficient of 0.22 for Risø-B1-18 and 0.21 for Risø-B1-24 when the Reynolds number was increased from 1.6×10^6 to 6×10^6. At the same time there was a decrease in minimum drag of 0.0024 for Risø-B1-18 and 0.0033 for Risø-B1-24. This shows that when using the measurements in the input to wind turbine blade design, proper corrections have to be done on both lift and drag to ensure reliable predictions of the aerodynamic characteristics of a wind turbine rotor with Risø-B1 airfoils.

References

[1] Abbott, I.H, and Doenhoff, E.v., 'Theory of Wing Sections', Dover Publications, Inc., New York (1959)

[2] Fuglsang, P., Bak, C., ' Modification of the NACA 63-415 leading edge to avoid double stall', Proc. of the 13th IEA Symposium on the Aerodynamics of Wind Turbines, Stockholm, Sweden (1999).

[3] Fuglsang, P., Antoniou, I., Sørensen, N.N., Madsen, H. Aa., 'Validation of a Wind Tunnel Testing Facility for Blade Surface Pressure Measurements.' Risø-R-981(EN), Risø National Laboratory, Denmark (1998)

[4] Rae Jr., W.H., Pope, A., 'Low-Speed Wind Tunnel Testing', SE, John Wiley & Sons, ISBN 0-471-87402-7. (1984).

[5] Brooks, T.F. and Marcolini, M.A., 'Airfoil Trailing Edge Flow Measurements and Comparison with Theory Incorporating Open Wind Tunnel Corrections', AIAA-84-2266, AIAA/NASA 9th Aeroacoustic Conference (1984).

[6] Hoerner, S.F. and Borst, H.V., 'Fluid-Dynamic Lift', Hoerner Fluid Dynamics, P.O. Box 342, Brick Town, N.J. 08723, USA (1975).

[7] Timmer, W.A., 'The design and testing of airfoil DU 91-W2-250', Proc. IEA Joint Action. Aerodynamics of Wind Turbines. 6th Symposium (1992).

[8] Sørensen, N.N., 'General Purpose Flow Solver Applied to Flow over Hills', Risø-R-827(EN), Risø National Laboratory, Denmark (1995).

[9] Menter, F.R., 'Zonal Two Equation k-ω Turbulence Models for Aerodynamic Flows', AIAA Paper 93-2906 (1993).

[10] Michel, R., 'Etude de la transition sur les profiles d'aile', ONERA Report 1/1578-A. See White F.M., Viscous fluid flow, p. 442 (1952).

[11] Bak, C., Madsen, H.A., Fuglsang, P., Rasmussen, F., 'Observations and Hypothesis of Double Stall', Wind Energy, **2**, 195-210 (1999).

[12] Bak, C., Fuglsang, P., Johansen, J., Antoniou, I, 2000, 'Wind Tunnel Tests of the NACA 63-415 and a Modified NACA 63-415 Airfoil.' Risø-R-1193(EN), Risø National Laboratory, December 2000, pp 107.

A Measurement overview

This appendix describes the performed measurements in detail to make the measurements stored on CD available for subsequent exploitation. The different measurement types are described and the naming convention for the data files is explained. The format of the data files is given and each performed measurement is listed and described.

A.1 List of symbols

h	[cm]	Wake rake vertical position, positive toward floor, origin at wake rake top
k		Reduced frequency
p	[Pa]	Static pressure
p_o	[Pa]	Total pressure head
p_{atm}	[Pa]	Atmospheric pressure
q	[Pa]	Dynamic pressure
x		Airfoil chord co-ordinate relative to chord, positive toward trailing edge, origin at leading edge
y		Airfoil vertical co-ordinate relative to chord, positive toward ceiling, origin at leading edge
A	[°]	Pitch motion amplitude
c_d		Drag coefficient
c_l		Lift coefficient
c_m		Moment coefficient
c_n		Normal force coefficient
c_t		Tangential force coefficient
C_p		Airfoil pressure coefficient
Re		Reynolds number
T	[°C]	Air temperature
α	[°]	Angle of attack
ρ	[kg/m^3]	Air density
Subscripts		
C		Corrected value
P		Pressure measurement (opposite to wake rake measurement)
W		Wake rake measurement
∞		Reference for normalisation of airfoil forces

A.2 Measurement types

There are four different basic types of measurements of the airfoil flow as shown in Table A-1:

Table A-1 Overview of the different types of measurements that have been performed.

CONT
Lift, drag and moment polar versus angle of attack.
• Continuous measurements at different angles of attack. • Angle of attack range: -6° to 35°. • Rate of change of angle of attack: 0.1°/s to 0.5°/s (manually changed). • Time series length app: 250 s. • Sampling frequency: 50 Hz.
STEP
The lift, drag and moment polar versus angle of attack.
• Discrete measurements at different angles of attack. • Angle of attack range: -6° to 35°. • Interval between different angles: 1° to 4°. • Time series length: 20 s. • Sampling frequency: 5 Hz.
STAT
Time series of airfoil flow at different angles of attack.
• Stationary measurements at different angles of attack. • Time series length: 60 s and 180 s. • Sampling frequency: 100 Hz.
PITCH
Time series of unsteady airfoil flow from pitching motion.
• Dynamic measurements at different mean angles of attack with the airfoil in pitching motion. • Pitching amplitude: 2° • Reduced frequency: 0.09 • Time series length: 30s. • Sampling frequency: 100 Hz.

The following table contains a list of all the data files that are available for each type of measurement. A detailed description of the data files is given in Section A.4.

Table A-2 Overview of the available data files for each measurement type.

CONT	
pol.bin	Raw data are sorted in bins of the angle of attack, Table A-5, to obtain airfoil forces versus angle of attack.
pol-1hz.nnn	Raw data as rows in general data file reduced to frames of 1 Hz, Table A-4.
pol-10hz.nnn	Raw data as rows in general data file reduced to frames of 10 Hz, Table A-4.
pol-50hz.nnn	Raw data as rows in general data file with frames of 50 Hz as the first 17 columns in Table A-4.
cp-1hz.nnn	C_P distribution in columns reduced to frames of 1 Hz.
V_w-1hz.nnn	Wake velocity distribution in columns reduced to frames of 1 Hz.
STEP	
pol.dat	Average general results where the average of each sub measurement is written in rows, Table A-4, to obtain airfoil forces versus angle of attack.
cp.dat	Average C_P distributions where the average of each sub measurement is written in columns corresponding to the rows in Pol.dat.
v_w.dat	Average wake rake velocity distributions where the average of each sub measurement is written in columns corresponding to rows in Pol.dat.
pol-5hz.nnn	Raw data as rows in general data file with frames of 5 Hz, Table A-4.
cp-5hz.nnn	C_P distribution in columns with frames of 5 Hz.
V_w-5hz.nnn	Wake velocity distribution in columns with frames of 5 Hz.
STAT	
pol.dat	Average general results where the average of each sub measurement is written in rows, Table A-4.
cp.dat	Average C_P distributions where the average of each sub measurement is written in columns corresponding to the rows in Pol.dat.
v_w.dat	Average wake rake velocity distributions where the average of each sub measurement is written in columns corresponding to rows in Pol.dat.
pol-100hz.nnn	Raw data as rows in general data file with frames of 100 Hz, Table A-4.
PITCH	
loop.nnn	Average results where raw data are sorted in bins of the phase angle of the hysteresis loop, Table A-7 Well suited to obtain hysteresis loops of c_l and c_d and c_m versus α.
pol.dat	Average general results where the average of each sub measurement is written in rows, Table A-4.
cp.dat	Average C_P distributions where the average of each sub measurement is written in columns corresponding to the rows in Pol.dat.
pol-100hz.nnn	Raw data as rows in general data file with frames of 100 Hz, Table A-4.

Where

- nnn is the sub measurement number

A.3 Data file naming convention

The different data files are stored in the following directory structure:

- The name of the airfoil.
- The measurement run name.

The naming and the format of the data files is explained in Table A-3.

A.4 Data file formats

The different data files are shown in Table A-3.

Table A-3 Available data files.

pol-yyhz.nnn	
yy	Frame average frequency: 100, 50, 10, 5 or 1
nnn	measurement sub number
General data file with each measurement frame/average formatted in rows. The first two rows contain the column number and the sensor name. The format of the data files is described in Table A-4	
STEP	Measurements are given with 5 Hz frame resolution
CONT	Measurements are given with 50 Hz, 10 Hz and 1 Hz frame resolutions respectively
STAT	Measurements are given with 100 Hz resolution
PITCH	Measurements are given with 100 Hz resolution

pol.dat	
General data file with overall average values of each sub measurement formatted in rows, as above. All sub measurements for a given measurement run are assembled into one single file. The format of the data files is described in Table A-4.	
STEP	Measurements are given with a 20 s average value for each sub measurement
PITCH	Measurements are given with a 30 s average value for each sub measurement
STAT	Measurements are given with a 60 s or 180 s average value for each sub measurement

pol.bin	
Post processed data file where the frames from all sub measurements are sorted in bins of the angle of attack to obtain the airfoil polar. The format of the data files is described in Table A-5.	
CONT	Measurements where the 50 Hz frames from all sub measurements are sorted in bins of α_c. The angle of attack range is divided into 30 bins.

loop.nnn	
nnn	Measurement sub number
Post processed data file where the frames from all sub measurements are sorted in bins of the phase of the hysteresis loop. The format of the data files is described in Table A-6.	
PITCH	Measurements where the 100 Hz frames from all sub measurements are sorted in bins of the phase of the hysteresis loop. The phase range is divided into 30 bins.

cp-yyhz.nnn	
yy	Frame average frequency: 5 or 1
nnn	measurement sub number
Data file with each frame/average formatted in columns. The first column contains the x-coordinates of the pressure tabs. The subsequent columns contain the C_P distributions for the different frames. The angle of attack for the frames can be found in the corresponding, pol-yyhz.nnn file.	
CONT	Measurements are given with 1 Hz frame resolution
STEP	Measurements are given with 5 Hz frame resolution

cp.dat	
Data file with each average formatted in columns. The first column contains the x-coordinates of the pressure tabs. The subsequent columns contain the average C_P distributions for each sub measurement. The angle of attack for the frames can be found in the corresponding, pol.dat file.	
STEP	Measurements are given as 20 s average values
STAT	Measurements are given as 60 s or 180 s average values
PITCH	Measurements are given as 30 s average values

v_w-yyhz.nnn	
yy	Frame average frequency: 5 or 1
nnn	measurement sub number
Data file with each frame/average formatted in columns. The first column contains the coordinates of the wake rake total pressure tabs. The subsequent columns contain the wake rake velocity for the different frames. The angle of attack for the frames can be found in the corresponding, pol-yyhz.nnn file.	
CONT	Measurements are given with 1 Hz frame resolution
STEP	Measurements are given with 5 Hz frame resolution

v_w.dat	
Data file with each average formatted in columns. The first column contains the coordinates of the wake rake total pressure tabs. The subsequent columns contain the average wake rake velocity distributions for each sub measurement. The angle of attack for the frames can be found in the corresponding, pol.dat file.	
STEP	Measurements are given as 20 s average values
STAT	Measurements are given as 60 s or 180 s average values

Table A-4 The content of the columns in the general data file.

Col.	Symbol	Sensor	Unit	Description
1	α_c	αc	°	Corrected angle of attack
2	c_l	cl	-	Lift coefficient (pressure)
3	c_{dc}	cd_c	-	Corrected drag coefficient (wake rake + pressure)
4	c_{mc}	cm_c	-	Corrected moment coefficient (pressure)
5	c_{nc}	cn_c	-	Corrected normal force coefficient
6	c_{tc}	ct_c	-	corrected tangential force coefficient
7	c_{dpc}	cdpc	-	Corrected drag coefficient (pressure)
8*	c_{dw}	cdw		Drag coefficient (wake rake)
9	α	α	°	Raw angle of attack
10	c_d	cd	-	Raw drag coefficient (wake rake + pressure)
11	c_{dp}	cdp		Raw drag coefficient (pressure)
12	c_m	cm	-	Raw moment coefficient (pressure)
13	c_n	cn	-	Normal force coefficient
14	c_t	ct	-	Tangential force coefficient
15	Re	re		Free stream Reynolds Number
16	q_∞	qref	Pa	Free stream dynamic pressure
17	p_∞	ps,ref	Pa	Free stream static pressure
18	T	t	°	Tunnel temperature
19	p_{atm}	patm	mBar	Atmospheric pressure
20-75**	C_P	cp(x)		Pressure coefficients corresponding to the coordinates in top row
76-78	$p_{1\text{-}3}$	ps,Pitot()	Pa	Pitot tube static pressures
79-81	$p_{o1\text{-}3}$	pt,Pitot()	Pa	Pitot tube total pressures
82-86*	p_w	ps,wake	Pa	Wake rake static pressures corresponding to the coordinates in top row
87-140*	p_{ow}	pt,wake	Pa	Wake rake total pressures corresponding to the coordinates in top row

*) At the 'PITCH' type measurements, the wake rake was not used. c_{dw} was set to c_{dP} and p_w and p_{ow} were not written in the data files.

**) In some measurements one or more of the airfoil pressure sensors were excluded because of unstable calibration or because the pressure hole was blocked by vortex generators or roughness elements. The corresponding column in the file was then removed and the number of subsequent sensors changed.

Table A-5 The content of the columns in the post processed data files sorted in bins of the angle of attack.

Col.	Symbol	Sensor	Unit	Description
1	α_c	aoa_c	°	Corrected angle of attack
2	c_l	cl	-	Lift coefficient (pressure)
3	c_{dc}	cd_c	-	Corrected drag coefficient (wake rake + pressure)
4	c_{mc}	cm_c	-	Corrected moment coefficient (pressure)
5	c_{nc}	cn_c	-	Corrected normal force coefficient
6	c_{tc}	ct_c	-	Corrected tangential force coefficient
7	c_{dpc}	cdpc	-	Corrected drag coefficient (pressure)

Table A-6 The content of the columns in the post processed data files sorted in bins of the phase angle of the hysteresis loop.

Col.	Symbol	Sensor	Unit	Description
1	α_c	αc	°	Corrected angle of attack
2	c_l	cl	-	Lift coefficient (pressure)
3	c_{dpc}	cdpc	-	Corrected drag coefficient (pressure)
4	c_{mc}	cmc	-	Corrected moment coefficient (pressure)

A.5 Performed measurements

Table A-7 and Table A-8 contain a list of the performed measurements for the different airfoil sections.

Table A-7 Risø-B1-18 performed measurements.

Run	Type	Surface conditions
024	CONT	Smooth
025	CONT	Leading edge roughness, Trip Tape 1
026	CONT	Leading edge roughness, Trip Tape 2
027	STEP	Smooth
028	STAT	Smooth
029	PITCH	Smooth, $k = 0.09$, $1.7° < A < 2.6°$
030	CONT	Leading edge roughness, 90° zigzag, 5% suction side / 10% pressure side
031	CONT	Leading edge roughness, 90° zigzag, leading edge, suction side
032	CONT	Leading edge roughness, 90° zigzag, leading edge, pressure side
033	CONT	Leading edge roughness, 60° zigzag, leading edge, suction side
034	CONT	Stall strip, 0% pressure side
035	CONT	Stall strip, 1% pressure side
036	CONT	Stall strip, 2% pressure side
037	CONT	Smooth
038	CONT	Stall strip, 3% pressure side

Table A-9 Risø-B1-24 performed measurements.

Run	Type	Surface conditions
002	CONT	Smooth
003	STEP	Smooth
004	STAT	Smooth
005	PITCH	Smooth, $k = 0.09$, $1.7° < A < 2.7°$
006	CONT	Leading edge roughness, 90° zigzag, 5% suction side / 10% pressure side
007	CONT	Leading edge roughness 60° zigzag, leading edge, suction side
008	CONT	Leading edge roughness 90° zigzag, leading edge, suction side
009	CONT	Leading edge roughness 90° zigzag, leading edge, suction side Vortex Generators, 20% suction side
010	CONT	Leading edge roughness 90° zigzag, leading edge, suction side Vortex Generators, 20% suction side Gurney flap, Triangular, 1% height
011	CONT	Vortex Generators, 20% suction side Gurney flap, Triangular, 1% height
012	CONT	Vortex Generators, 20% suction side
013	CONT	Gurney flap, Triangular, 1% height
014	CONT	Vortex Generators, 15% suction side Gurney flap, Triangular, 1% height
015	CONT	Vortex Generators, 25% suction side Gurney flap, Triangular, 1% height
016	CONT	Vortex Generators, 30% suction side
017	CONT	Vortex Generators, 15% suction side
018	CONT	Gurney flap, Triangular, 0.5% height
019	CONT	Gurney flap, Triangular, 2% height
020	CONT	Gurney flap, 90° angle, 1% height
021	CONT	Gurney flap, 120° angle, 1% height
022	CONT	Smooth

Bibliographic Data Sheet **Risø-R-1375(EN)**

Title and authors

Wind Tunnel Tests of Risø-B1-18 and Risø-B1-24

Peter Fuglsang, Christian Bak, Mac Gaunaa, Ioannis Antoniou

ISBN			ISSN
87-550-3139-0 87-550-3140-4 (internet)			0106-2840
Department or group			Date
Wind Energy Department	January 2003		
Groups own reg. number(s)			Project/contract No(s)
1110401-00			
Pages	Tables	Illustrations	References
82	9	58	12

Abstract (max. 2000 characters)

This report contains 2D measurements of the Risø-B1-18 and Risø-B1-24 airfoils. The aerodynamic properties were derived from pressure measurements on the airfoil surface and in the wake. The measurements were conducted in the *VELUX* open jet wind tunnel, which has a background turbulence intensity of 1%, and an inlet flow velocity of 42 m/s. The airfoil sections had a chord of 0.600 m giving a Reynolds number of 1.6×10^6. The span was 1.9 m and end plates were used to minimize 3D flow effects. The measurements comprised both static and dynamic inflow. Static inflow covered angles of attack from -5^o to 30^o. Dynamic inflow was obtained by pitching the airfoil in a harmonic motion around various mean angles of attack. The test matrix involved smooth flow, various kinds of leading edge roughness, stall strips, vortex generators and Gurney flaps in different combinations.

The quality of the measurements was good and the agreement between measurements and numerical CFD predictions with EllipSys2D was good. For both airfoils predictions with turbulent flow captured very well the shapes of lift and drag curves as well as the magnitude of maximum lift. Measurements of Risø-B1-18 showed that the maximum lift coefficient was 1.64 at an angle of attack of approximately 13^o. The airfoil was not very sensitive to leading edge roughness despite its high maximum lift. Measurements with stall strips showed that stall strips could control the level of maximum lift. The Risø-B1-24 measurements showed that the maximum lift coefficient was 1.62 at an angle of attack of approximately 14^o. The airfoil was only little sensitive to leading edge roughness despite its high relative thickness and high maximum lift. Measurements with delta wing shaped vortex generators increased the maximum lift coefficient to 2.02 and measurements with Gurney flaps increased the maximum lift coefficient to 1.85. Measurements with combination of vortex generators and Gurney flaps showed a maximum increase in the maximum lift coefficient to 2.17.

At the design Reynolds number of 6×10^6 numerical predictions showed that there was a clear increase in the maximum lift coefficient of 0.22 for Risø-B1-18 and 0.21 for Risø-B1-24.

Descriptors INIS/EDB

AERODYNAMICS; AIRFOILS; DRAG; STALL; TEST FACILITIES;
TESTING; TURBINE BLADES; TURBULENT FLOW;
TWO-DIMENSIONAL CALCULATIONS; WIND TUNNELS;
WIND TURBINES